AN ASSESSMENT OF THE HIGH-RESOLUTION RAPID REFRESH MODEL'S ABILITY TO RESOLVE THE GREAT LAKES MARINE ATMOSPHERIC BOUNDARY LAYER AND LAKE-BREEZE FRONT

by

Collin DeYoung

A Thesis Submitted in

Partial Fulfillment of the

Requirements for the Degree of

Master of Science

in Atmospheric Science

at

The University of Wisconsin-Milwaukee

May 2024

ABSTRACT

AN ASSESSMENT OF THE HIGH-RESOLUTION RAPID REFRESH MODEL'S ABILITY TO RESOLVE THE GREAT LAKES MARINE ATMOSPHERIC BOUNDARY LAYER AND LAKE-BREEZE FRONT

by

Collin DeYoung

The University of Wisconsin-Milwaukee, 2024
Under the Supervision of Professor Clark Evans

We determined the ability of the High-Resolution Rapid Refresh (HRRR) mesoscale model to predict the lake-breeze front's structure and faithfully represent the marine atmospheric boundary layer (MABL) behind it. First, two field missions were completed during the 2023 warm season over Lake Michigan to characterize the spatiotemporal evolution of the MABL and validate HRRR forecasts. We found the Lake Michigan MABL was characterized by minimal thermodynamic and kinematic variability on diurnal time scales, regardless of the stability or flow regime. Additionally, the HRRR was able to resolve MABL thermodynamic structures effectively but underestimated the vertical temperature distribution, leading to a persistent cold bias at all vertical levels over Lake Michigan. Second, a model-based lake-breeze detection algorithm was developed and tested on multiple 2023 warm season lake-breeze cases. The algorithm skillfully predicted the evolution of the lake-breeze front for offshore flow regimes across the warm season but struggled to consistently identify the front under onshore flow regimes. These results advance our understanding of the warm-season MABL structure over the Great Lakes, its influence on lake-breeze front propagation, and how faithfully the HRRR represents these features.

TABLE OF CONTENTS

LIST OF FIGURES

LIST OF TABLES

LIST OF ABBREVIATIONS

BKE	Block-based Komura Equivalence
CCL	Connected Components Labeling
CDT	Central Daylight Time
CONUS	Continental United States
FVCOM	Finite Volume Community Ocean Model
GFS	Global Forecast System
GPS	Global Positioning System
GSI	Gridpoint Statistical Interpolation
HRRR	High Resolution Rapid Refresh
HRRRDAS	HRRR Data Assimilation System
MABL	Marine Atmospheric Boundary Layer
MRMS	Multi-Radar Multi Sensor
MYNN-EDMF	Mellor-Yamada-Nakanishi-Niino eddy-diffusivity/mass-flux
NAM	North American Mesoscale
NOAA	National Oceanic and Atmospheric Administration
NWP	Numerical Weather Prediction
RMSE	Root-Mean Square Error

RRTMG	Rapid Radiative Transfer Model for Global Climate Models
RUC LSM	Rapid Update Cycle Land Surface Model
SGS	Subgrid-scale Modeling
SST	Sea-Surface Temperature
TKE	Turbulent Kinetic Energy
WRF	Weather Research & Forecasting

ACKNOWLEDGEMENTS

I want to express my gratitude and thanks to my advisor Dr. Clark Evans for his continued support throughout this project that made this possible. His guidance over the past two years helped me learn more than I could have asked for and demonstrated to me what it means to be a scientist in our field.

An additional thanks to Dr. Sergey Kravtsov and Dr. Jon Kahl for serving on my committee alongside Dr. Evans.

Lastly, a great thanks to my family and friends who supported me throughout this journey.

1. Introduction

a. The Great Lakes Lake-Breeze Front

The weather and climate in the upper-midwestern United States are significantly influenced by the Laurentian Great Lakes (hereafter simply Great Lakes) through the heat exchange between the lakes and the air above. Water has a higher specific heat capacity than air, meaning it takes more energy to warm water than air by the same amount. As a result, the surface water temperatures, or SSTs, of the Great Lakes lag seasonal variations in lower-atmosphere air temperatures (e.g., Fig. 1). This temperature difference between the water and air results in significant heat exchange between the two through sensible and latent heat fluxes within the atmospheric

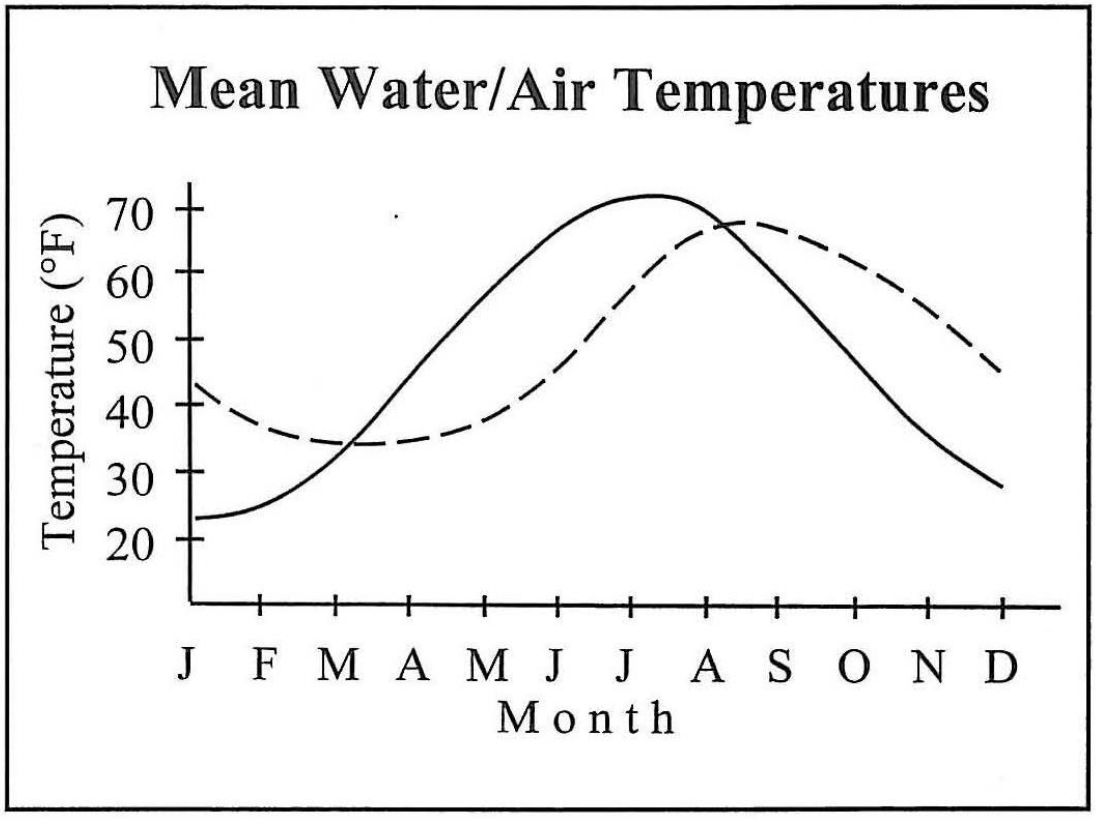

FIG 1. Mean water temperature (dashed) over Central Lake Michigan and mean air temperature (solid) for Muskegon, Michigan (Smith 2001).

boundary layer – representing the layer of the atmosphere that is directly influenced by heat, moisture, and frictional exchanges with the Earth's surface (Stull 1988). The magnitudes and signs of these fluxes are dependent on the temperature and moisture differential between the air and water with a large difference inducing larger fluxes. During the warm season, the synoptic-scale flow often advects warmer air from the land over the cooler water throughout the boundary layer (Lyons 1972), resulting in a negative sensible heat flux. The air closest to the water surface experiences rapid remodification to match the lake's SST values with a lesser impact on boundary layer temperatures further aloft (Lyons 1970; Bellaire 1965). As a result, the marine atmospheric boundary layer (MABL) across the Great Lakes is prone to very strong inversions where the temperature increases significantly with height, particularly during the late spring/early summer.

The depth of the Great Lakes' warm-season temperature inversion layer is typically no greater than a few hundred meters. The larger the difference between the air and the SSTs, the larger the vertical temperature gradient, particularly towards the water surface. For example, observations have demonstrated that the strongest temperature gradient within the inversion occurs in the lowest 20 to 30 m of the MABL, especially towards the center of Lake Michigan where SST values are the lowest (Bellaire 1965). Much of this is owed to the residence time of the airmass that is advected over the water – more time spent over the cool SSTs towards the center of the lake allows for greater modification of air temperatures within the MABL. By the time the marine-modified airmass reaches the downwind shoreline, the near-surface air temperatures are nearly identical to the SST values.

The airmasses that interact with the Great Lakes MABL originate from the planetary boundary layer (PBL) over land and are heavily influenced by diurnal heating due to land's low specific heat capacity. During the daytime, the land surface heats up more efficiently from solar insolation, leading to significant vertical heat transfer throughout the PBL. Consequently, the PBL experiences large positive sensible heat fluxes and turbulent vertical mixing per the diurnal cycle. Driven by this difference in specific heat between the land and water surface, the result is a differential in the heating of two distinct airmasses along the Great Lakes coastlines. The atmosphere responds with localized circulations along the lakeshore that attempt to resolve this heating imbalance (Miller et al. 2003). In the Great Lakes, this differential heating in the warm season manifests as a lake-breeze – a thermally direct solenoidal circulation that separates the PBL from the MABL.

The lake breeze's development is driven by mesoscale horizontal pressure and density gradients induced by differential diurnal heating between the land and lake (Miller et al. 2003; Simpson 1994). As the air over land warms in tandem with the diurnal cycle, it expands and becomes less dense, promoting the buoyantly driven ascent of initially surface-based parcels. Conversely, the air's density and pressure over the cooler water remain approximately constant due to the minimal diurnal response of the water temperature to daytime insolation. If the resulting horizontal pressure gradient is sufficiently large, the air within the MABL is directed towards the shore, whereupon it encounters the PBL. The intersection of these two air masses defines the lake-breeze front (e.g., Fig. 2). The less-dense, less-unstable airmass ahead of the lake-breeze front is forced to rise, whereas the air in the MABL behind the lake-breeze front is more

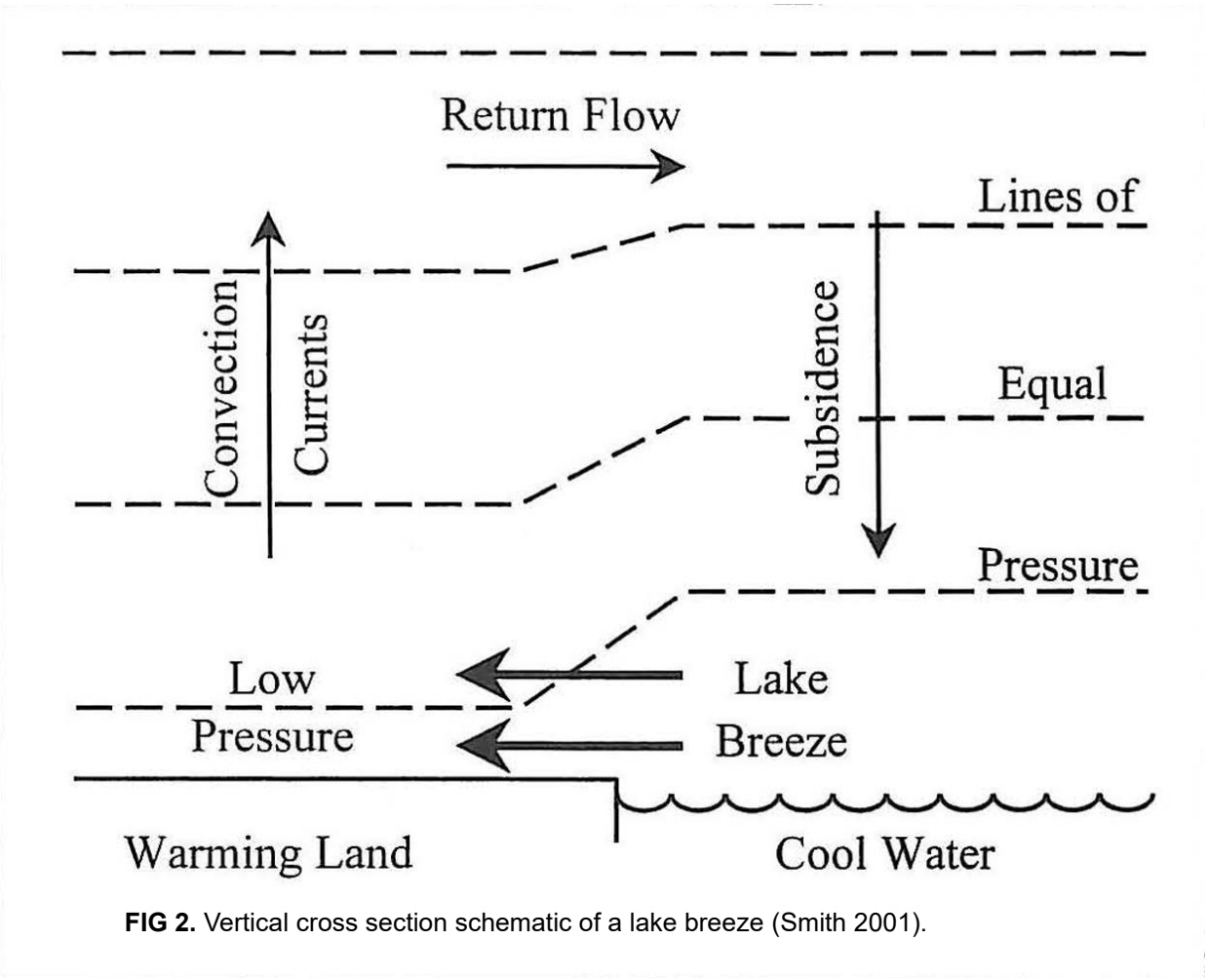

FIG 2. Vertical cross section schematic of a lake breeze (Smith 2001).

stable and descends to the surface. The circulation is completed by return flow from the land to the lake atop the MABL through the advection of MABL-influenced air over land. Upon the arrival of the lake-breeze front, surface temperatures rapidly drop as the warm air of the PBL is replaced with cooler, more humid, and more stable MABL air. This transition is the most significant at the early stages of the lake-breeze circulation's life cycle and diminishes as the lake-breeze front progresses further inland. With time, the marine airmass behind the front is warmed by upward sensible heat fluxes from the underlying warm land surface, resulting in a more subtle temperature gradient along the lake-breeze boundary (Lyons 1972).

The lake-breeze front's initiation is largely dependent on the near-surface wind speed and the horizontal temperature gradient's magnitude. If the offshore component of the background synoptic flow is too strong, particularly greater than 5 m s^{-1} (e.g., Segal et al. 1997; Crossman and Horel 2010), the lake-breeze circulation is not sustainable and will be washed out by the synoptic-scale wind. Thermodynamically, a lake-breeze front can develop if the surface water temperature is at least 1 °C colder than the land (Watts 1955). Furthermore, modeling studies have shown that the effect of the water surface temperature is not important for lake-breeze development, so long as the land warms up enough to allow for stable stratification of the MABL (Segal and Pielke 1985; Arritt 1987). Thus, the heating over land determines the temperature gradient between the land and water and is the driving factor for lake-breeze development (Segal and Pielke 1985). This is contingent on the strength of the synoptic flow – weaker temperature gradients require weaker synoptic flow for lake-breeze circulations to develop (Biggs and Graves 1962; Lyons 1972; Segal et al. 1997; Crossman and Horel 2010). Lake breezes can still develop with a weaker temperature gradient or stronger background flow, but the circulations are generally confined to the coastline.

Research into the Great Lakes lake-breeze front has been motivated by its influence on nearshore weather conditions (e.g. Scott and Huff 1996) and its ability to initiate convection along the frontal convergence zone (Kingsmill 1995). Along with the temperature decrease post lake-breeze passage, the stable airmass behind the front inhibits convective cumulus cloud growth, whereas enhanced convergence along the front forces surface-based parcels to rise and promotes convective cloud growth

(Kingsmill 1995; Segal et al. 1997). Consequently, the presence of shore-parallel bands of cumulus clouds are often indicative of the lake-breeze front's position through remotely sensed radar and satellite data. Along with the modifications to nearshore weather conditions, lake-breeze research is heavily motivated by the circulation's propensity to transport and trap pollutants near the surface (Lyons and Cole 1976; Dye et al. 1995; Lennartson and Schwartz 2002; Wagner et al. 2021). The lake-breeze front significantly impacts the air quality of large metropolitan areas along the Great Lakes' coastlines with increased concentrations of ground-level ozone being the primary concern. Emissions of nitric oxide [NO] and nitrogen dioxide [NO_2] from combustion engines react with oxygen in the atmosphere and create ozone which is damaging to vulnerable populations (USDA 2020). Normally, these pollutants are transported offshore by the near-surface wind and remain over water with minimal impact on people. However, the lake-breeze circulation mixes these pollutants down towards the surface in its descending branch, and the circulation's onshore flow transports the pollution inland (Lyons and Cole 1973). Furthermore, ground-level ozone production is enhanced by strong solar insolation and weak surface winds, both of which are characteristic of the post-lake-breeze frontal airmass (Lyons and Cole 1976). Finally, convergence along the lake-breeze front also increases ozone concentrations as the front progresses inland (Lennartson and Schwartz 2002).

b. Model Verification and Prediction of the Lake-Breeze Front

The climatic and anthropogenic impacts of the lake-breeze front have encouraged research towards identification and prediction of the lake-breeze circulation throughout the Great Lakes region. Lake-breeze cases were first identified using a lake-

breeze index based on a critical ratio of the wind speed and the horizontal temperature gradient; a ratio of inertial and buoyant forces (Biggs and Graves 1962). This index was utilized in Lyons (1972) but included additional parameters such as expected cloud cover and wind direction to improve lake-breeze hindcasts. Both methods yielded high skill for identifying the occurrence of the lake-breeze front, but struggled to classify non-lake-breeze events, overpredicted lake-breeze occurrence, and had to be adjusted for different coastal environments (Biggs and Graves 1962: Lyons 1972). Different critical values were necessary due to variations in lake orientation, depth, and coastal geography for the respective studies. More recent approaches have utilized observational datasets to identify lake-breeze events by including criterion such as surface wind speed/direction, temperature, dewpoint, cloud cover, and precipitation (Laird et al. 2001; Sikora et al. 2010; Stauffer et al. 2015; Stauffer and Thompson 2015), examples of which are shown in Table 1.

Table 1. List of multiple detection algorithms, the regions where they were tested, and the parameters used to identify the presence of the lake-breeze, denoted by a checkmark.

Detection Algorithm	Region	Temperature Drop	Wind Shift	Dewpoint Rise	Dry-Bulb Drop	Wind Gust
Biggs and Graves (1962)	Lake Erie	✓	✓			
Lyons (1972)	Chicago, IL	✓	✓			
Sikora et al. (2010)	Chesapeake Bay		✓		✓	✓
Stauffer and Thompson (2015)	Chesapeake Bay		✓			
Stauffer et al. (2015)	Edgewood, MD		✓	✓		

Such detection algorithms have been crucial in developing climatological datasets of lake-breezes in the Great Lakes region, giving insight into the spatiotemporal variability and impacts of the lake-breeze front.

While observational methods have been the traditional way to identify the lake-breeze front, numerical weather prediction model analysis and forecasts can also be used to identify and predict the lake breeze. One of the first approaches utilized a high-resolution mesoscale model that could resolve lake breezes along Lake Michigan's shoreline. The model's output was able to identify the lake-breeze front up to 48 hours in advance and outperformed simple lake-breeze indices. However, the main limiting factor was a dependence upon an accurate representation of the synoptic near-surface flow and Lake Michigan SSTs (Roebber and Gehring 2000). Model-based approaches were expanded upon by Hawbecker and Knievel (2022a) by using the observational detection algorithms of Sikora et al. (2010), Stauffer et al. (2015) and Stauffer and Thompson (2015) to detect coastal circulations within the Weather Research and Forecasting (WRF) and High-Resolution Rapid Refresh (HRRR) model domains. Applied to the Chesapeake Bay sea-breeze, skills for the observational detection algorithms were generally poor because their detection parameters did not translate well to the grid-cell averaged and smooth gradients of the WRF and HRRR model fields. Thus, Hawbecker and Knievel (2022a) created a model-based detection algorithm that took advantage of the model's continuity, utilizing parameters such as vertical wind shear and lapse-rate inferred stability to identify the lake-breeze front. This algorithm performed better with significantly fewer misses and higher precision, especially for the HRRR analyses and forecasts. The fine tuning of the algorithm's parameters to the

three-dimensional model space improved predictability compared to observational methods and demonstrated the ability of a high-resolution model to discriminate between lake-breeze days.

c. Motivation

The present research seeks to expand on the current literature regarding high-resolution model-based verification, detection, and prediction of the Great Lakes MABL structure and its associated lake-breeze circulation with a focus on the western coast of Lake Michigan. Accurately detecting and predicting the lake-breeze front using a model relies on a faithful representation of the lake-breeze circulation within the model domain. Previous studies have shown the main deficiencies of model-based detection algorithms are rooted in the representation of SSTs and flow patterns within the land-based and marine boundary layer (Roebber and Gehring 2000; Hawbecker and Knievel 2022b). Models that inaccurately predict SST values and MABL thermodynamic structures can lead to unrealistic sensible heat fluxes that depict the wrong temperature profiles or stability regimes over water (Segal and Pielke 1985; Arritt 1987). In-situ observations are one-way SSTs and near-surface temperatures are determined across the Great Lakes. However, these are sparse with a low density of buoy sites located primarily along coastlines, minimal observations from instrumentation on ships, and sporadic radiosonde launches. Measurements from airliners are used to determine boundary layer and upper-air atmospheric variability over land, but do not descend low enough to capture shallow MABL structures over water.

Lake temperatures and near-surface variables are also assimilated into operational weather models via satellite data. However, these have low horizontal and

vertical spatial resolutions and struggle to capture the temporal characteristics of lake-temperatures, leading to biases in the resolved SSTs for large bodies of water (Schluessel et al. 1990; Donlon et al. 2002; Benjamin et al. 2022; Iversen et al. 2023). Model biases in lake SST values have been demonstrated to translate to the MABL across the Great Lakes during the warm season (Wang et al. 2022), leading to unrealistic lake-breeze development, or lack thereof, due to unrealistic air temperatures and flow regimes (Reobber and Gehring 2000; Zhang et al. 2019; Hawbecker and Knievel 2022b). With the most recent version of the HRRR discussed in Section 2a, lake-temperatures are specified more accurately due to loose coupling of NOAA's Finite Volume Community Ocean Model (FVCOM) model (Chen et al. 2006) with the HRRR to provide better initial conditions for lake temperatures, improving forecasts along lake coastlines (Dowel et al. 2022). Thus, the high resolution of the HRRR combined with its lake-model coupling provides a unique avenue towards assessing a model's ability to resolve the MABL structure.

To assess the ability of the HRRR model to faithfully represent the structure and evolution of the MABL and its associated lake-breeze circulation along Lake Michigan's western shoreline, observations of the MABL environment over water were collected for two days during the 2023 warm season. Utilizing UWM's *Neeskay* research vessel, thirty radiosondes in total have been launched to analyze the 3-dimensional spatial and temporal resolution of the MABL environment. With this observational dataset, the spatiotemporal evolution of the MABL is better documented in a region where vertical profiles of its structure are nearly nonexistent. Furthermore, the dataset provides two case studies on lake-breeze front evolution from the perspective of the marine side of

the boundary in a research field where land-based observations dominate. Comparison of these observations to the HRRR domain also serves as validation of the model output to identify any biases or inconsistencies with the observed MABL structure. In tandem with model-based verification, a lake-breeze detection algorithm has been developed to identify the lake breeze in HRRR model output. The detection algorithm seeks to objectively identify the spatial extent of the lake-breeze front across all grid cells of Lake Michigan's coastline by isolating the thermodynamic and kinematic discrepancies associated with the lake-breeze front. With this algorithm, the ability of the HRRR to resolve and predict the evolution of the lake-breeze front is assessed.

d. Thesis Organization

The next section of this paper describes the background of the HRRR model (section 2a), the instrumentation used to measure the evolution of the MABL structure over Lake Michigan (section 2b), the details of the two field campaigns (section 2c), and the formulation of the lake-breeze detection algorithm (2d). The subsequent results are split into sections 3 and 4. Section 3 analyzes the spatiotemporal characteristics of the MABL for the June 1st, 2023 field mission (3a) and validates the HRRR model against the observational dataset (3b). Sections 3c and 3d follow the same organization, but for the September 14th, 2023 field mission. Section 4 assesses the performance of the lake-breeze algorithm for HRRR analyses (4a) and its dependence upon the flow regime (4b) and stability regime (4c). The figures that visualize the observational dataset and lake-breeze algorithm are listed in appendices A and B, respectively. Lastly, the results from the observations and lake-breeze algorithm are synthesized in section 5.

2. Methodology

a. HRRR Model

All model-based verification was conducted for the National Oceanic and Atmospheric Administration's (NOAA) HRRR model, an operational convective-allowing model across the Continental United States (CONUS) with a 15-minute temporal cycle (Benjamin et al. 2016; Dowell et al. 2022; James et al. 2022). Data was readily available every hour with a minimum forecast duration of 18 h along with an extended 48 h forecast on a 6 h cycle beginning at 0000 UTC each day. The HRRRv4 version of the HRRR model, operational since January 2020, was used for the analysis performed in this research with a focus on forecasts between 0 and 12 h. It is necessary to note the 2020 upgrade to the HRRR model inadvertently set the terrain height of the Great Lakes to zero and was resolved in July 2022 (Tallapragada, 2022). Thus, all analysis of HRRR model output for the Great Lakes was done for the 2023 warm season. Data was downloaded from the Amazon Web Server Open Data Registry which provides an archive of HRRR data back to 2014 that includes all initialization, forecast, and coordinate systems of the HRRR.

The HRRR utilizes the HRRR Data Assimilation System (HRRRDAS) system to assimilate the most recent conventional observations including aircraft, rawinsonde, Global Positioning System (GPS) precipitable water, surface, buoy/ship, profiler, and satellite wind observations every hour (Dowell et al. 2022) in conjunction with 3-dimensional radar reflectivity observations from NOAA's Multi-Radar Multi Sensor (MRMS) project every 15 minutes over the 1-hour cycle (Zhang et al. 2016; Smith et al. 2016). Lateral boundary conditions are provided by the RAP model. Initial conditions are

created by passing the observations through the HRRRDAS, a 36-ensemble member model, of which the ensemble mean provides the first guess to the HRRR and the member 1-hr forecasts provides the background error covariances for the Gridpoint Statistical Interpolation (GSI) hybrid data assimilation (Dowell et al. 2022).

Assimilated observations are interpolated onto a 3 km grid with 51 terrain-following vertical levels extending between the surface and 15 hPa. The HRRR utilizes a hybrid sigma-terrain following vertical coordinate system with model levels closely following the terrain near the surface and gradually transitioning to primarily isobaric surfaces in the mid-to-upper troposphere (Klemp 2011). At the surface, the model uses the most recent version of the Rapid Update Cycle land surface model (RUC LSM) scheme with nine soil levels contrasted to the six soil levels prior, allowing for an accurate depiction of the near-surface temperature diurnal cycle (Smirnova et al. 2016). To resolve subgrid-scale processes within the boundary layer, the HRRR uses the Mellor-Yamada-Nakanishi-Niino eddy-diffusivity/mass-flux (MYNN-EDMF) planetary boundary and surface layer scheme (Dowell et al. 2022), a scheme whose functionality is relevant to the formation of the model-based detection algorithm and will be discussed in more detail in section 2d. Shortwave and longwave radiation are parameterized using the Rapid Radiative Transfer Model for Global Climate Models (RRTMG) scheme (Iacono et al. 2008) modified with Subgrid-scale (SGS) cloud properties from the MYNN-EDMF scheme, reducing bias errors in surface temperatures for HRRRv4 prior to previous iterations (Dowell et al. 2022). Lastly, the Thompson bulk scheme (Thompson et al. 2004, 2008) is used to parameterize cloud microphysics.

b. Instrumentation

The Windsond S1H3 system from Sparv Embedded of Sweden were used to collect vertical profiles of the Lake Michigan MABL. The Windsond system has been used primarily for lower-tropospheric observations (Markowski et al. 2018; Bessardon et al. 2019; White et al. 2020; Diedrichsen et al. 2023) due to its portable size and smaller balloon size requiring as little as 1/20th the helium of other radiosonde systems, such as Vaisala radiosondes (Sparv Embedded 2019). This makes Windsonds a cost-effective option without a sacrifice in measurement quality. Bessardon et al. (2019) directly compared the more commonly used Vaisala RS41 radiosonde system to Windsonds and found strong correlations between the temperature, humidity, and pressure profiles of the two systems. The primary drawback of the Windsond system was its slower response time causing temporary biases and wind errors near the surface. Later work by Diedrichsen et al. (2023) also demonstrated the thermal profiles from the Windsond system were nearly identical to the Vaisala RS41 radiosonde profiles in the lowest 3 km of the atmosphere with biases less than 0.5 °C. Noticeable wind direction differences were observed within 250 m of the surface, primarily due to excess swinging of the Windsonds upon launch due to their smaller size. Direct comparisons of the low-cost Windsond system to the more expensive Vaisala system has demonstrated that the former is reliable for thermodynamic observations of the boundary layer. However, it is important to keep in mind the Windsond's kinematic biases observed near the surface.

The S1H3 version is a lightweight radiosonde which measures real-time temperature, pressure, wind, and humidity profiles. Temperature was measured using a band-gap thermometer, pressure was measured with a barometric pressure sensor,

wind speed and direction was calculated using GPS position, and humidity was measured using a capacitive hygrometer. Furthermore, each Windsond was equipped with a 76 mAh rechargeable lithium-ion battery (BL75), weighing 1.9 g, to power the sensors. Sensor specifications, such as operating range and accuracy, are shown in Table 2 (Sparv Embedded 2019).

Table 2. Sensor specifications of the Windsond system. The units for each column correspond to the units listed in the rightmost column.

Variable	Data Range	Resolution	Accuracy	Response Time	Units
Temperature	-40 to + 80	0.01	± 0.2	6 s	Celsius
Pressure	300 to 1100	0.02	± 1.0		hPa
Wind Speed	0 to 150	0.1	± 5%		$m\ s^{-1}$
Wind Direction	0 to 360	0.1	Variable		Degrees
Humidity	0 to 100	0.05	± 1.8	6 s	%

Prior to launch, each Windsond was tethered to a 9 g latex weather balloon filled with helium with a targeted circumference of 120 cm, corresponding to about 30 liters of helium per balloon. At this balloon size, the Windsonds rise at an average speed of 2 m s^{-1} for the duration of their ascent. Once the Windsonds were launched, they recorded the time, altitude above mean sea level, ascent speed, and latitude and longitude at each observed level. Raw measurements of temperature, wind, and pressure were sent in a data packet every third second at a sampling frequency of 1 Hz. Any missing data sent between packets was interpolated by the software based on existing measurements (Sparv Embedded 2019). All the aforementioned parameters were written to a SHARPpy (Blumberg et al. 2017) text file format that interpolated the data to a constant above-ground-level vertical coordinate, with data every 20 m. Temperature

and relative humidity measurements were corrected based on incoming solar radiation intensity to reduce warm biases caused by solar heating of the Windsond (Sparv Embedded 2018).

c. 2023 Warm Season Field Missions

Two field missions were completed in 2023 with fifteen Windsond profiles collected for each mission. Using UWM's *Neeskay* research vessel, vertical profiles of the MABL were captured over western-central Lake Michigan off the port of Milwaukee. Before each mission, transects of the research vessel were defined to assess MABL variability in accordance with the remotely sensed spatial variability of Lake Michigan's SSTs. Furthermore, the frequency of the Windsond launches were predetermined at the desired spatial and temporal variability along the *Neeskay* transect. The following sections describe in detail the transect paths, frequency of the Windsond launches, and overall synoptic environment for these missions.

I. June 1st, 2023

For the June 1st mission, the team on the *Neeskay* vessel departed from the Port of Milwaukee around 0800 CDT and concluded the mission around 1600 CDT. At the surface over land, the environment was characterized by light east-southeast flow and sunny skies in the morning hours, followed by convective initiation inland along a lake-breeze front shortly after 1300 CDT. Behind the lake-breeze front and over Lake Michigan, the skies were clear as well. While temperatures reached as high as 32 °C inland, temperatures along Lake Michigan's western coastline remained around 24 °C due to the cold water temperatures and present lake-breeze circulation. The

consistently cool temperatures along the lakeshore and subsequent convective initiation inland along the lake-breeze front were plotted in Figs. 3 and 4, respectively.

Windsonds were launched off the *Neeskay* along a linear east-to-west 20 nautical mile-long transect with five launch locations (Fig. 5) The first Windsond launch, sonde 1, was performed 1 n. mi. east of Milwaukee's shoreline followed by four more launch sites to the east. Each of the Windsond launch sites were approximately 5 n. mi. apart from each other. Once the *Neeskay* arrived at the eastmost launch site 21 n. mi. away from the shoreline, the *Neeskay* ventured back west along the same path, launching the remaining Windsonds at the previous launch sites. For each site, the vessel stopped momentarily to prepare the Windsonds for launch. Once the Windsonds were successfully launched and were transmitting data, the *Neeskay* continued to the next launch site. Most of the launch sites only had one Windsond launch, especially for the first half of the transect. At the following sites, three Windsonds were launched in total during the second half of the transect; the eastmost site (sondes 5 through 7), the centermost site (sondes 9 through 11), and the westmost site (sondes 13 through 15). At the singular launch sites, the Windsonds were launched 30 to 40 minutes apart from each other. At the stationary sites, the sondes were launched approximately 20 minutes apart from each other. The exact launch times for each Windsond are listed in Table 3.

June 1st, 2023 – Surface Analysis Charts

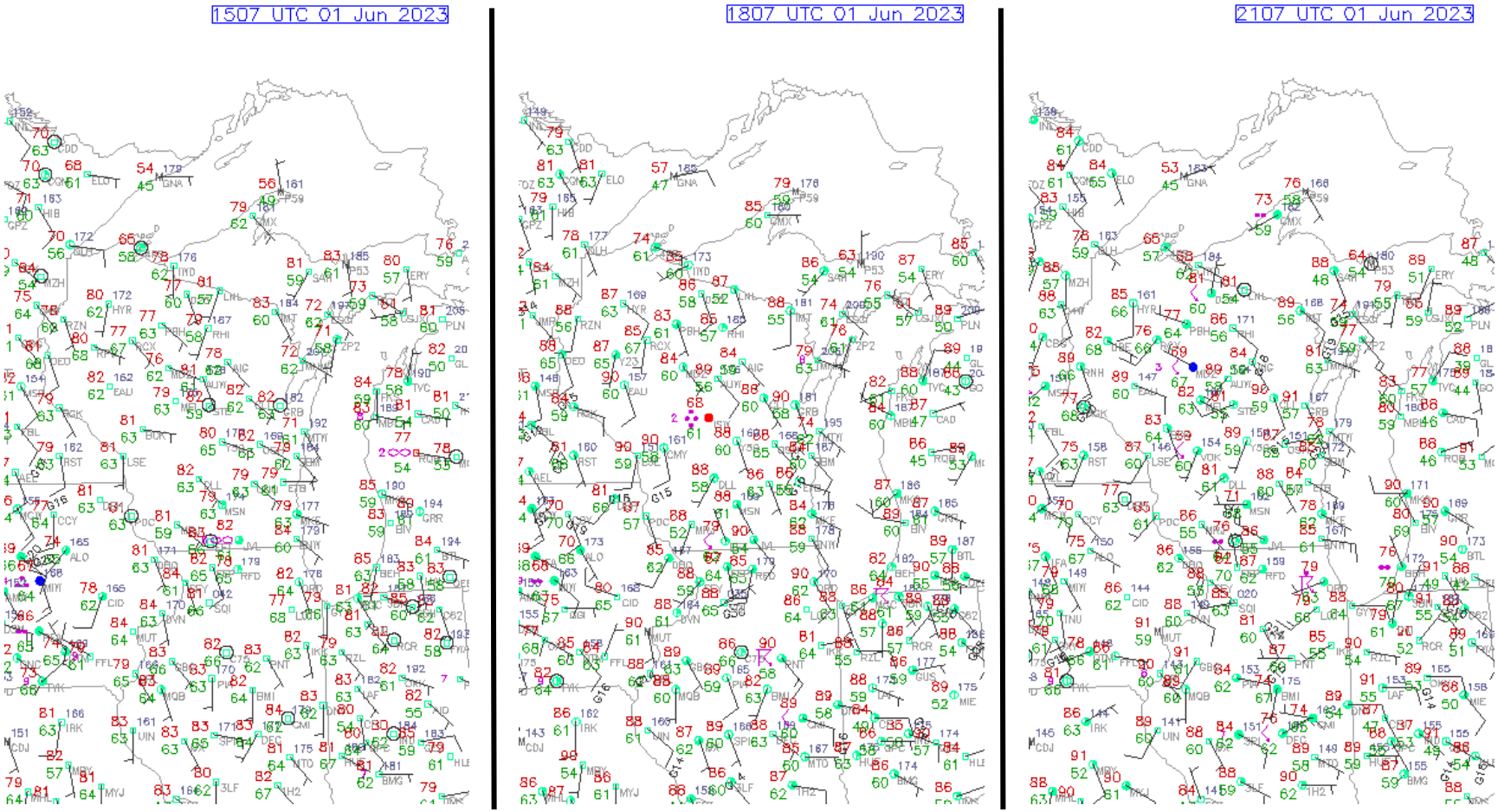

FIG 3. Surface analyses of temperature, dewpoint, and wind direction/speed represented as station plots for June 1st, 2023, valid around 1000 CDT (left), 1300 CDT (center), and 1600 CDT (right). Images were retrieved from the NCAR Image Archive (Ahijevych 2023)

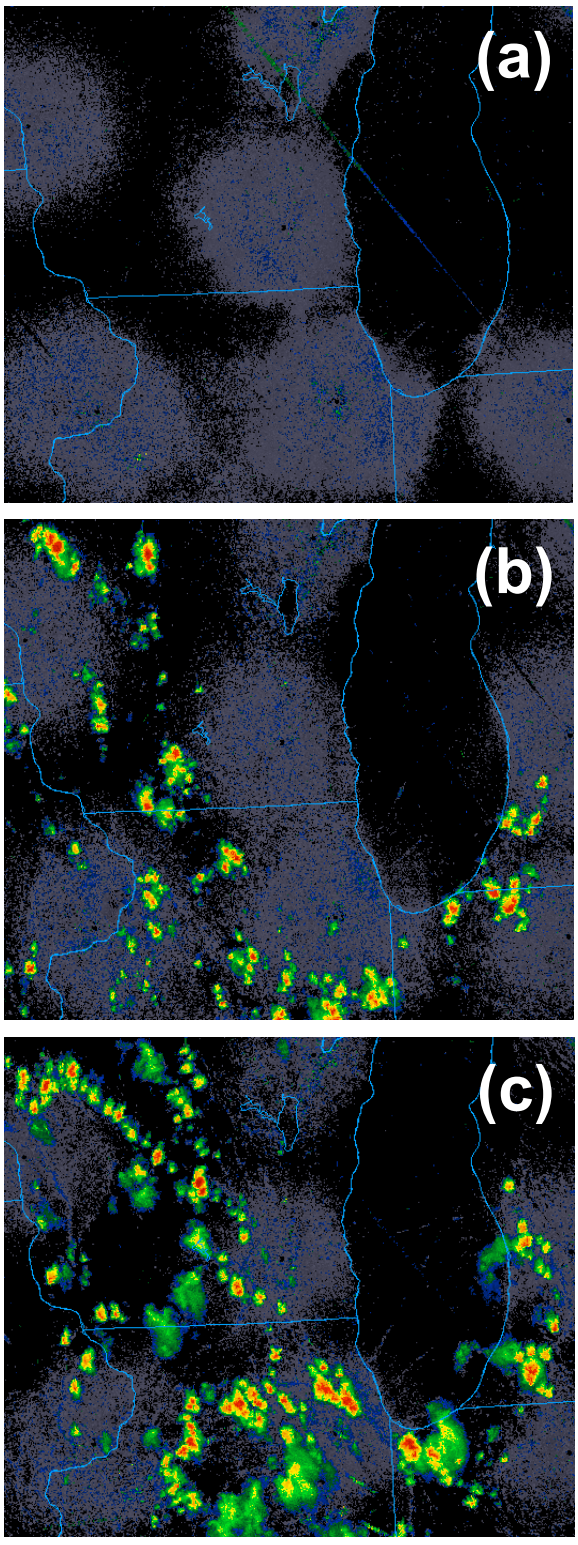

FIG 4. Plot of radar composite maps derived from WSR-88D radars across the United States. Maps are valid around 1000 CDT (a), 1300 CDT (b) and 1600 CDT (c) for June 1st, 2023. Images were retrieved from the NCAR Image Archive (Ahijevych, 2023)

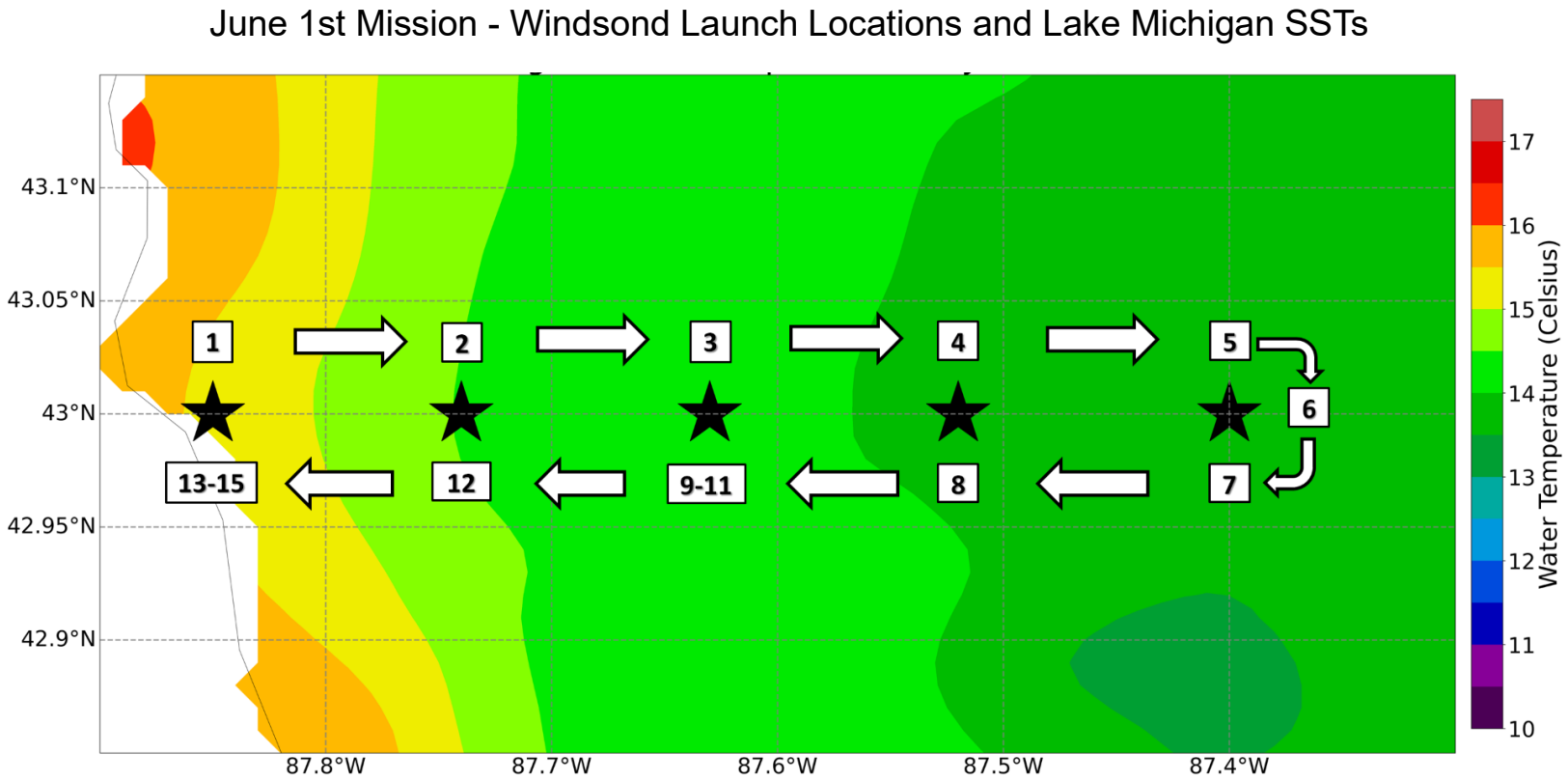

FIG 5. Plot of the GHRSST's Level 4 sea surface temperature (SST) Analysis for western Lake Michigan (color contours), valid at 0900 UTC on June 1st, 2023, along with the excursion track of the *Neeskay* research vessel. Windsond launch locations are denoted by a black star. The numbers in white boxes next to the black stars denote the Windsond launch number at that site. The arrows denote the path of the *Neeskay*, showcasing a linear east-west path.

Table 3. List of the Windsond launch times for the June 1st, 2023, mission. The launch times, converted to UTC, are listed in parentheses next to the CDT launch time.

Sonde Number	Time in CDT (UTC)	Sonde Number	Time in CDT (UTC)
1	0825 (1325)	8	1232 (1732)
2	0904 (1404)	9	1311 (1811)
3	0947 (1447)	10	1332 (1832)
4	1028 (1528)	11	1356 (1856)
5	1107 (1607)	12	1430 (1930)
6	1136 (1636)	13	1507 (2007)
7	1156 (1656)	14	1529 (2029)
		15	1552 (2052)

II. September 14, 2023

Given the September 14th mission occurred much later in the season, SST values over western Lake Michigan were between 20 and 21 °C (see Fig. 6). Land-surface temperatures were similar to Lake Michigan SST's during the morning and early afternoon hours with temperatures around 18 °C in the morning and 22 °C in the afternoon. Southerly flow and cloudless skies were present for the entire day over land due to a high-pressure system positioned to the east of Lake Michigan. The variation of these surface conditions over land were plotted in Fig. 7. Evidence of a developing lake-breeze circulation was seen as early as 1000 CDT (1500 UTC) with onshore flow along the coastline along the Illinois/Wisconsin border. By 1300 CDT (1800 UTC), more sites along Lake Michigan's western coastline had easterly flow and slightly cooler 2 m temperatures compared to inland stations. By the late afternoon, almost every station along the western coast had an easterly flow component, in direct contrast to the southerly winds further inland. It was at this point where the lake-breeze circulation was evident through surface observations and with the Windsond data.

The September 14th mission began around 0900 CDT and concluded around 1800 CDT with a total of fifteen Windsond launches. Beginning approximately 3 n. mi. east of the Port of Milwaukee, the *Neeskay* followed a clockwise rectangular transect (Fig. 6). The north-south portions of the transect were approximately 11 n. mi. long, whereas the east-west portions of the transect were approximately 10 n. mi. long. There were 8 unique launch sites in total which were approximately 5 n. mi. apart from each other. Along both north-south transects of the mission, comprising six of the eight launch sites, two Windsonds were launched each per site. The only locations that had one

Windsond launch were the centermost sites along the east-west portions of the transect and the last Windsond at the last launch site. Just like the June 1st mission, the *Neeskay* was stationary for each Windsond launch and departed to the next site once all the necessary Windsonds were launched. The Windsonds were launched roughly 20 minutes apart from each other at the sites where two sondes were launched. The travel time between each site was approximately 25 to 30 minutes. The exact times of each launch are listed in Table 4.

Table 4. List of the Windsond launch times for the September 14th, 2023, mission. The launch times, converted to UTC, are listed in parentheses next to the CDT launch time.

Sonde Number	Time in CDT (UTC)	Sonde Number	Time in CDT (UTC)
1	0910 (1410)	8	1319 (1819)
2	0929 (1429)	9	1342 (1842)
3	1017 (1517)	10	1434 (1934)
4	1042 (1542)	11	1502 (2002)
5	1136 (1636)	12	1546 (2046)
6	1159 (1659)	13	1614 (2114)
7	1237 (1737)	14	1657 (2157)
		15	1739 (2239)

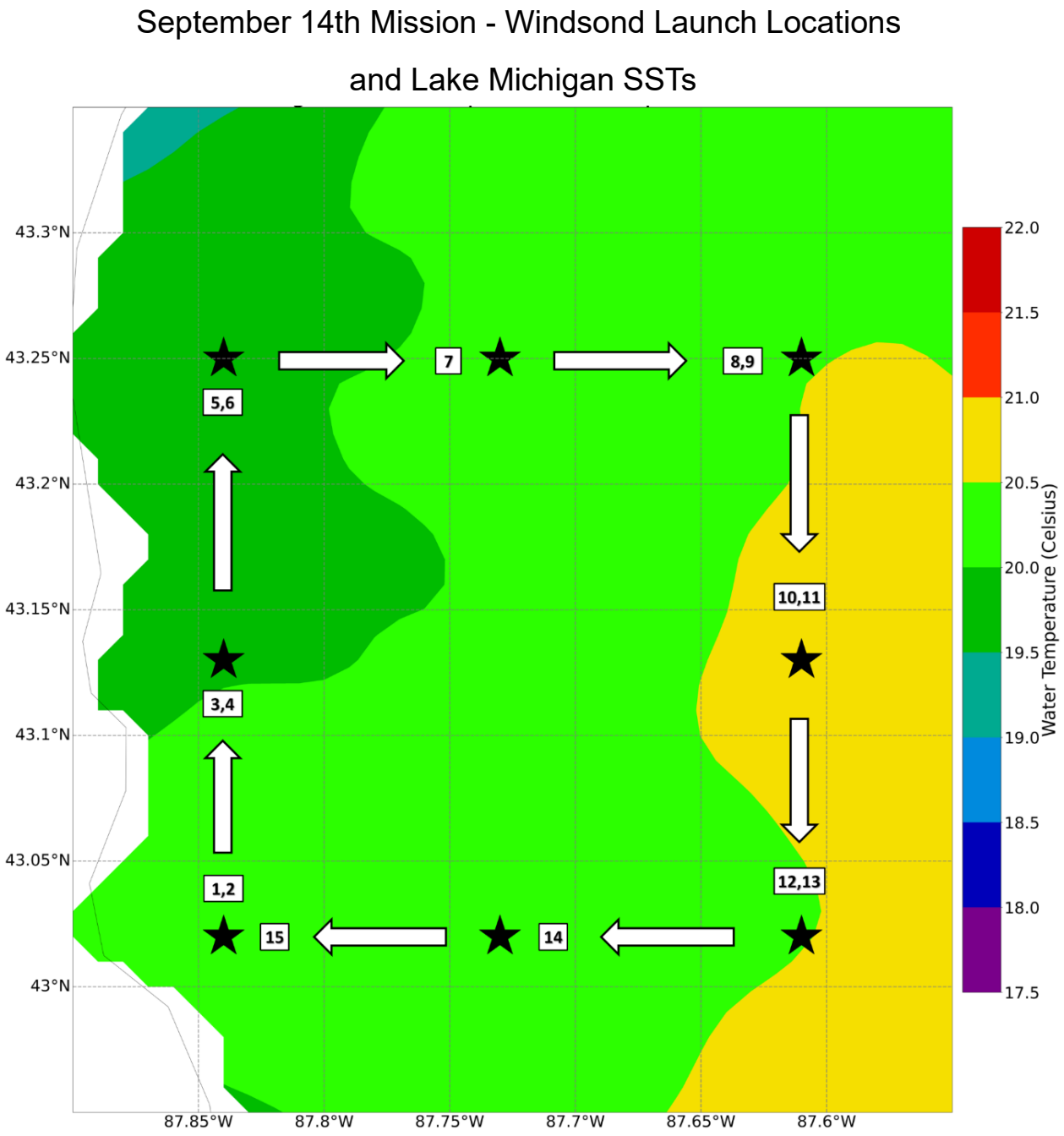

FIG 6. Plot of the GHRSST's Level 4 sea surface temperature (SST) Analysis for western Lake Michigan (color contours), valid at 2300 UTC on September 14th, 2023, along with the excursion track of the *Neeskay* research vessel. Windsond launch locations are denoted by a black star. The numbers in white boxes next to the black stars denote the Windsond launch number at that site. The arrows denote the path of the *Neeskay*, showcasing an east-west clockwise path.

September 14th, 2023 – Surface Analysis Charts

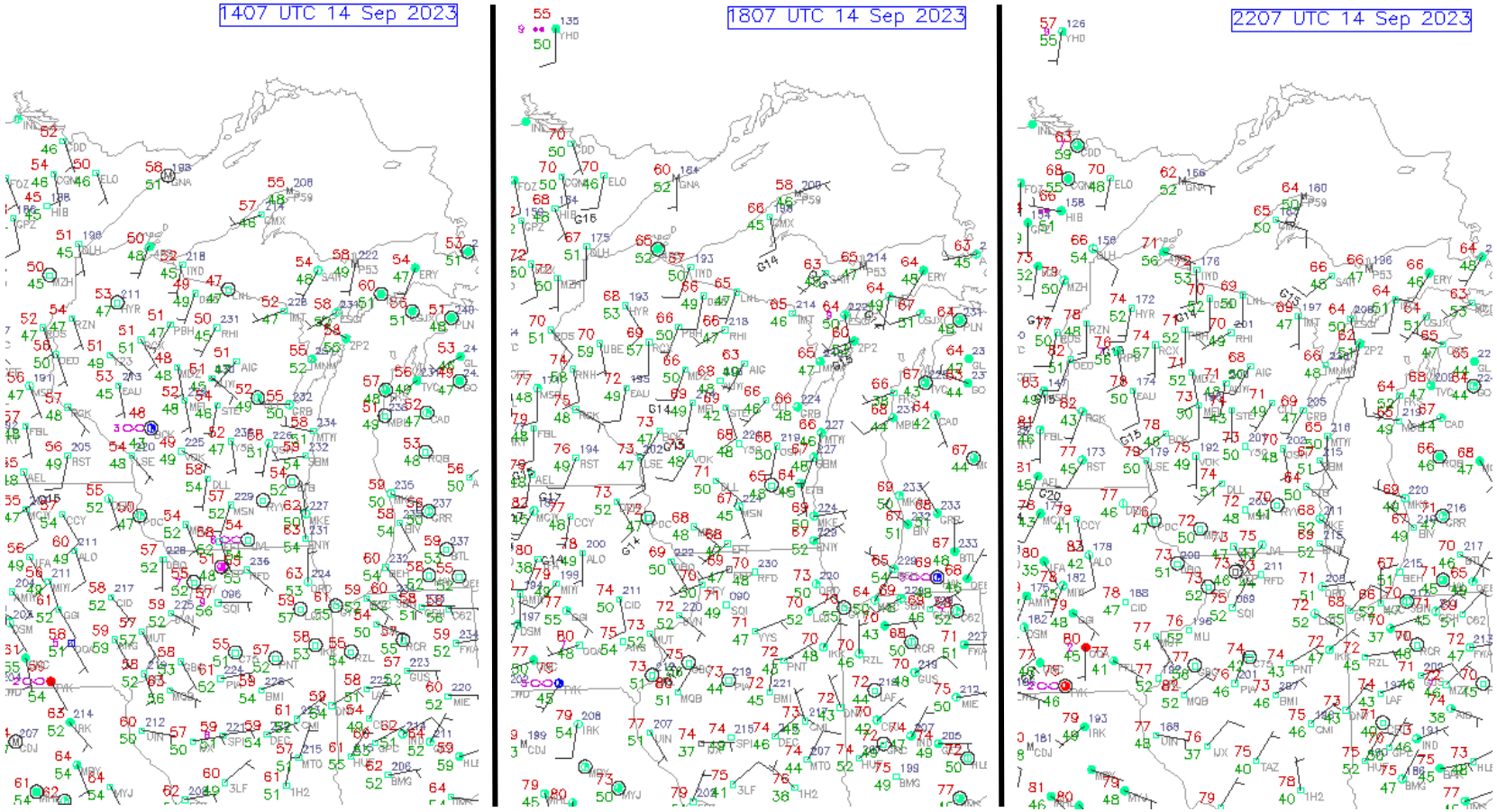

FIG 7. Surface analyses of temperature, dewpoint, and wind direction/speed represented as station plots for September 14th, 2023, valid around 0900 CDT (left), 1300 CDT (center), and 1700 CDT (right). Images were retrieved from the NCAR Image Archive (Ahijevych 2023)

III. Model Verification of the Observed MABL Structure

The data from both *Neeskay* missions will be analyzed in more detail in Section 3. In addition to discussing the variability of the MABL environment over Lake Michigan, the observations will be used to verify HRRR model forecasts. To accurately compare the Windsonds to HRRR output, the Windsond launch times were matched to the closest HRRR analyses or forecast time of which all future times will be denoted in UTC. Additionally, a given Windsond's latitude and longitude coordinates were matched to the nearest grid cell in the HRRR. To compare the 20 m resolution data of the Windsonds to the HRRR vertical profiles, the native hybrid-sigma coordinates of the HRRR were linearly interpolated to a 20 m resolution. It is relevant to note that geometric height coordinates in meters were not innate to the HRRR's vertical dimension. To compensate for this, geopotential height coordinates along the hybrid-sigma levels were used as a substitute for geometric height given the minimal discrepancies between the two in the lower troposphere.

The selection of height coordinates for bias assessment was due to some observed variations in pressure towards the surface. When the Windsonds determine the height and pressure above ground level, the first value measured when the sonde is turned on sets the AGL pressure and height as a reference for the AGL coordinates (Sparv Embedded 2018). Thus, if the Windsond had a high or low bias in the first measured pressure, that pressure bias persists for the remaining observations. Despite a relative stagnation of the surface pressure synoptically for both cases, a few Windsonds had surface pressures vary a few hectopascals between sites. Thus, when comparing the vertical profiles between Windsonds, some begin at different pressure

levels than others along a pressure coordinate system, like on a skew-T. This generally was not too big of an issue for the September case whose MABL environment was near homogeneous vertically but had larger implications for the June 1st mission as will be discussed in section 3.

d. Description of the Lake-Breeze Detection Algorithm

The essence of the lake-breeze detection algorithm is isolating the lake-breeze front by locating the grid cells where the front was being depicted in the HRRR domain. To identify the lake-breeze front, the HRRR's domain was scanned to identify where atmospheric parameters were changing in accordance with a lake-breeze front passage. To locate where a transition in an atmospheric field was occurring across model grid cells, the algorithm computed the spatial gradient of specified flagging parameters, and identified where this gradient was maximized. Ideally, these gradient maxima should coincide with the lake-breeze front's position, contingent on the fact that the selected parameters were relevant to lake-breeze front passage.

The following two parameters used to identify the lake-breeze front at a given grid cell were, 1) the model-derived planetary boundary layer height, and 2) the u and v components of the wind. Using the wind speed as an identifying criterion for the lake-breeze front is intuitive given the opposition of the lake-breeze front's progression to the large-scale flow and the localized acceleration of flow that occurs behind the boundary. Furthermore, the wind speed (Biggs and Graves 1962; Lyons 1972) and wind direction (Laird et al. 2001; Sikora et al. 2010; Stauffer et al. 2015; Stauffer and Thompson 2015) have been used in past research to identify the lake-breeze front. The boundary layer criterion was chosen because the lake-breeze front often separates the distinctly

different PBL and MABL airmasses. The former has a deep boundary layer due to sensible heating and turbulent mixing, whereas the latter has a shallow boundary layer due to the high stability and downward momentum fluxes. Therefore, a significant discrepancy in the boundary layer height should occur across the lake-breeze front.

In the model space, the HRRR outputs the PBL height parameter hourly based on the MYNN-EDMF boundary layer parameterization. This scheme employs a hybrid definition of the boundary layer height that utilizes a potential temperature definition for convective boundary layers and a turbulent kinetic energy (TKE) definition for stable boundary layers. This approach has been shown to be more accurate across these stability regimes than using one approach alone (Lemone et al. 2013; Lemone et al. 2014). The former height is determined by identifying the minimum virtual liquid/ice potential temperature (θ_{vli_min}) in the lowest 200 m. Where the potential temperature equals θ_{vli_min} plus 0.75 K over land or 1.25 K over water, is the convective boundary layer's height (Nielsen-Gammon et al. 2008; Olson et al. 2019). The latter height is computed where the TKE at the surface decreases below a threshold value equal to 5% of TKE at the surface. Once the boundary layer height is computed for both approaches, the potential temperature definition is used when the convective boundary layer height exceeds 200 m, and the stable boundary layer height definition is used when the convective boundary layer height is less than 200 m (Olson et al. 2019).

To determine where these parameters experienced the largest differentials associated with a lake-breeze front, the first-order gradient magnitude of both parameters were computed across a subset of the HRRR domain centered around Lake

Michigan. The gradient computations applied to each grid cell are shown in Equations 1 and 2

$$(1) \quad \nabla|BLH| = \sqrt{\left(\frac{dBLH}{dx}\right)^2 + \left(\frac{dBLH}{dy}\right)^2}$$

$$(2) \quad \nabla|\vec{\boldsymbol{V}}| = \sqrt{\left(\frac{du}{dx}\right)^2 + \left(\frac{dv}{dy}\right)^2}$$

where *BLH* corresponds to the boundary layer height and $\boldsymbol{V}$ corresponds to the total wind, and *u* (*v*) corresponds to the east-west (north-south) components of the wind. The output of these gradients without any filtering were prone to noisy output due to unrelated lake-breeze phenomena. To reduce this noise, minimum threshold values were set for the boundary layer and wind gradients based on an analysis of lake-breeze cases during the 2023 warm season. With respective thresholds of 20 and 0.2 for the boundary layer and wind gradients, grid cells where these thresholds were met were identified. If a threshold was met for a parameter, a binary flag of 1 was set for that grid cell, or 0 if the threshold was not met. Lastly, the flags were summed up for each grid cell where a sum of 2 meant both parameters flagged. Locations across the domain where the total flags equaled 2 corresponded to the position of the lake-breeze front. All grid cells where the flag was less than 2 were treated as noise and were not plotted. A visualization of this output is shown in Fig. 8. The result of this process is an isolation of the lake-breeze front where kinematic and thermodynamic differentials coincide while filtering out insignificant gradients.

To further isolate the lake-breeze front and remove residual noisy gradients that result from precipitation, localized convective updrafts, or synoptic-scale features, the

algorithm utilizes image processing algorithms from the OpenCV python library developed by Bradski and Kaehler (2008). A Block-based Komura Equivalence (BKE) connected components labeling (CCL) algorithm (Allegretti et al. 2019) implemented by OpenCV was applied to identify continuous features associated with the lake-breeze front. A CCL algorithm scans an image's pixels and identifies 'blobs' of pixels in a binary image using a nearest neighbor algorithm that connects pixels with the same binary output. Applied to the lake-breeze algorithm, the CCL isolates the shore-parallel continuous flags associated with the maximized boundary layer and kinematic gradients. The image processing is applied as follows:

1. Load the raw image of the lake-breeze algorithm's output (e.g. Fig. 8).
2. Convert the raw image into a grayscale image and apply a gaussian blur to the grayscale image.
3. Apply a threshold to the grayscale image that converts it into a binary image.
4. Compute the CCL analysis.
5. Set a minimum and maximum area threshold for the identified connected components.
6. Plot the areas that meet the threshold and repeat for all identified components.

Once the following steps were complete, the 'blob' that corresponds to the lake-breeze was plotted for the HRRR domain. This image serves as the final output of the lake-breeze algorithm and is plotted in Fig. 9 for the example shown in the previous figure. Components detected by the algorithm that did not correspond to the lake-breeze were not shown in the final lake-breeze algorithm output. This version of the algorithm will be used to assess the position and spatial extent of the lake-breeze front in section 4.

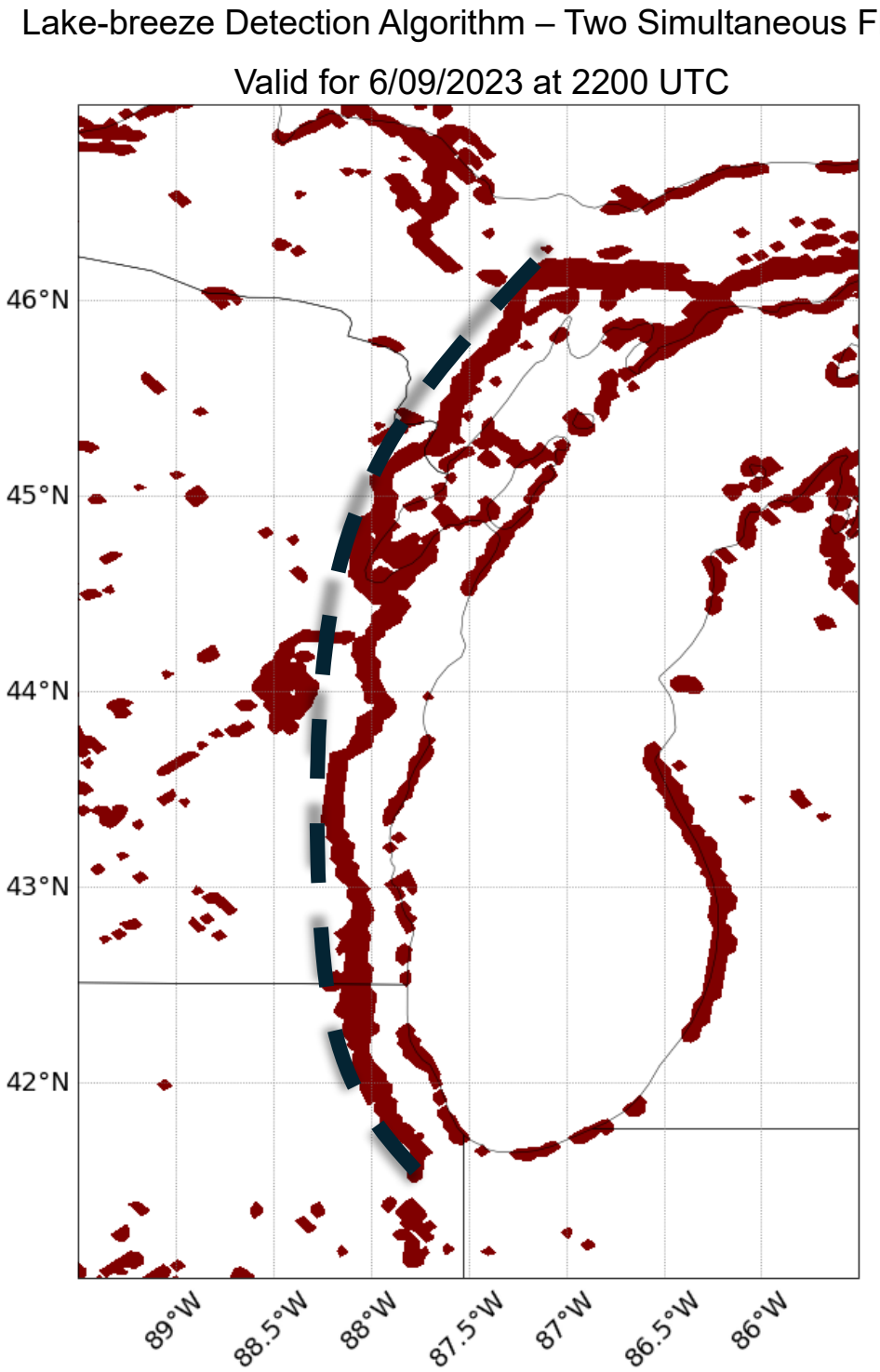

FIG 8. Plot of the lake-breeze algorithm utilizing the binary flags of the boundary layer height and wind gradient magnitudes. Flag values less than 2 were contoured to be the same color as the background (white). Areas in red denote where the total number of flags equals 2. The dashed black line corresponds to the identified lake-breeze front. The model output is valid for June 9th, 2023, at 2200 UTC.

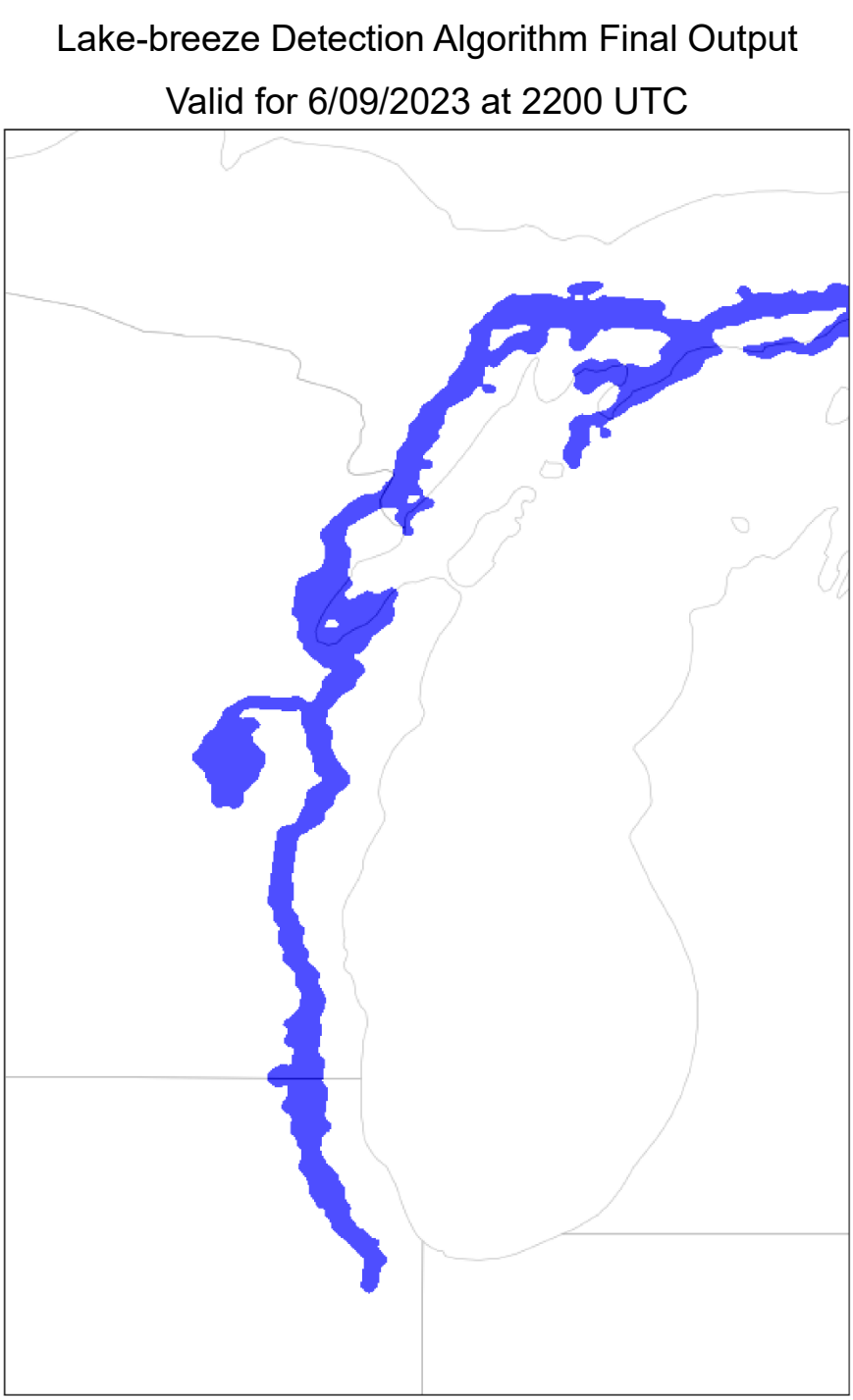

FIG 9. Plot of the lake-breeze algorithm post-image processing using the CCL algorithm. The area shaded in blue denotes the position of the lake-breeze front given the area thresholds are met by the algorithm. The model output is valid for June 9th, 2023, at 2200 UTC.

3. Evaluation of the 2023 Warm Season MABL

a) June 1st, 2023 – Characteristics of the MABL

The skew-T profiles captured on June 1st were used to determine the spatial and temporal variability in the structure of the MABL. The advection of the significantly warmer PBL airmass over the cool lake resulted in a highly stable MABL environment over Lake Michigan for the entire excursion. This was immediately evident during the morning along the first half of the transect (e.g., Fig. 11) with an incredibly strong inversion present in a shallow layer no deeper than 950 hPa, denoting the top of the MABL. The temperature increased by approximately 8 °C from the surface to the MABL top for the first seven Windsonds launched with little variability in the inversion depth or magnitude. The persistent temperature discrepancies seen between the Windsonds launched at the eastmost site (e.g., Fig. 11c) were exaggerated along the pressure coordinate system due to the surface-pressure biases discussed in section 2c. In conjunction with the minimal variability in the heat distribution throughout the MABL, the structure of the dewpoint profiles were consistent as well. A gradual moistening of the MABL column did occur between Windsonds 1 and 3, but the dewpoint lapse rates, and vertical distribution of moisture were unchanged along the first half of the transect. Windsond 4 was deemed to have an erroneous humidity measurement due to its abnormally low surface dewpoint and persistent dry bias that was inconsistent with the other Windsonds. Kinematically, the winds within and above the MABL were predominately out of the southeast around 5 kts with a gradual shift towards southerly flow with each Windsond launch. Variations in the wind speed or direction were

negligible between the Windsonds, demonstrating the stagnation of the flow regime over Lake Michigan.

Along the second half of the transect (e.g., Fig. 12), a slight increase in the inversion magnitude was present for Windsond 8 and persisted as the *Neeskay* continued west towards the shoreline. The increase in the vertical temperature gradient was a consequence of diurnal heating of the PBL airmass that was being advected over the water surface. Despite this, surface temperatures remained around 18 °C, which was the same as the first half of the transect, and the depth of the inversion remained around 950 hPa. The dewpoint profiles were nearly identical for the Windsonds along the second half of the transect, maintaining a gradual decrease in moisture with height within and above the MABL. A notable decrease in moisture was present above 800 hPa for Windsonds 13 through 15 (e.g., Fig. 12c), but this was well outside the confines of the MABL. Lastly, winds near the surface were predominately out of the east at 5 kts for Windsonds 9 through 12 with a decrease in wind speed towards the shoreline for the last launch site (Fig 12c). Further aloft, the winds continued to veer to the south with insignificant changes to the wind speed. The persistence of the easterly flow near the surface in direct contrast to flow above the MABL was indicative of an ongoing lake-breeze circulation. Additionally, onshore observations captured inland progression of the lake-breeze front around 1800 UTC around the same time Windsond 9 measured the onshore surface flow over Lake Michigan.

To better assess the spatiotemporal variations of the temperature and dewpoint, the observed profiles were compared along the height-based coordinates of the Windsond system. With this perspective, the small-scale variations that did occur were

more apparent and easier to quantify. Along the first half of the transect (e.g., Fig. 13), the main discrepancy was a colder and weaker inversion for Windsond 1 compared to the latter six Windsonds launched. With time, a gradual warming of the MABL column occurred due to diurnal heating during the morning hours. However, this warming was marginal, and the depth of the inversion remained consistent at ~ 200 m for the first seven Windsonds. This warming did extend above the MABL but was even less significant than what was observed below the top of the inversion. For the dewpoint profiles, the spatiotemporal evolution seen with the skew-T analysis was replicated here – dewpoints in the MABL increased with each Windsond launch, apart from Windsond 4. Windsond 4 did have a lower surface temperature, comparable to Windsond 1, which was likely why the dewpoint profile for the two Windsonds were nearly similar. Despite this outlier, a general increase in moisture content was observed. Across the first half of the transect, there were marginal increases in moisture and temperature throughout the MABL, but with no significant chance to the MABL structure as seen in Fig. 14.

For the second half of the transect, spatiotemporal variations of the MABL primarily occurred with the temperature profiles – the dewpoint profiles were nearly identical. The increase in the inversion magnitude identified in the skew-T analysis post Windsond 8 was apparent as seen in Fig. 15, given the increase in the vertical temperature gradient throughout the MABL. The timing of this MABL warming around 1800 UTC (Windsond 9) matched well with the development of the lake-breeze circulation. It can be hypothesized that warming of the MABL was induced by the enhanced subsidence over water from the lake-breeze circulation, forcing adiabatic warming of descending parcels that warmed the column. However, without more

observations, this could not be confirmed and could be coincidental with the diurnal warming in the afternoon. For Windsonds 13 through 15 1 n. mi. away from the shoreline, a uniquely shallow unstable layer extended from 20 m to 80 m for all three Windsonds. The origin of this layer was likely a result of turbulent mixing due to the abrupt change in surface roughness close to the shoreline. The forced deceleration of the wind from the east eroded the inversion near the surface, creating a shallow, well mixed MABL. The result was a significantly colder MABL environment from 20 m to 400 m for Windsonds 13 – 15 compared to the Windsonds launched to the east. Furthermore, the presence of this layer displaced the inversion vertically to ~ 100 m, weaking the vertical temperature gradient without a substantial modification to the MABL depth seen in Fig. 16.

b. Model Verification of the June 1st MABL Structure

To first characterize the HRRR's depiction of the MABL through its initialized 0 h analyses, skew-T profile comparisons were first analyzed in Figs. 17 and 18. Windsond 1 was an anomaly amongst the fourteen other Windsonds launched for this mission, given that it underestimated the magnitude of the inversion and overforecasted the dewpoint over Lake Michigan. For the remaining Windsonds launched after 1300 UTC presented in Figs. 17 and 18, the HRRR was able to replicate the inversion magnitude decently well, capturing the sharp change in temperature with height over a shallow layer. Furthermore, the HRRR faithfully resolved the depth of the MABL at a height of 950 hPa and replicated the steeper lapse rates seen above the MABL. However, the analyses significantly underestimated the temperatures nearest to the surface as high as 5 °C for Windsond 10, for example. The consequence of this was a persistent cold

bias from the HRRR that permeated the entire temperature profile for every Windsond launched on June 1st, including Windsond 1. The magnitude of the cold bias near the top of the MABL and well above averaged around 2 °C, regardless of time or location. Despite the large bias in temperature, the dewpoint errors were nowhere near as egregious with many of the HRRR dewpoint profiles matching well with the observations. Occasionally the HRRR analyses would depict unrealistic dry or moist layers at specific levels, particularly in the MABL, but these biases were not consistent between HRRR analyses. Additionally, the kinematic fields were represented well by the HRRR analyses that captured the weak southeasterly flow through the shallow MABL for the whole excursion.

The root mean square error (RMSE) and bias were calculated between all fifteen Windsonds and the HRRR profiles to assess the average error for the HRRR 0 h analyses, plotted in Fig. 19. With these profiles, the biases present from the HRRR were evident, especially in the MABL where temperature changed so rapidly with height. As seen with the skew-Ts, an average error of 2 °C occurred for the entire vertical profile based on the RMSE calculations. Additionally, the magnitude of the dewpoint RMSE was similar to that of the temperature, albeit a larger surface dewpoint error around 3 °C. From the bias profile, the 20 m temperature was consistently underrepresented by the HRRR analyses with a bias of -1.5 °C. Furthermore, there was a near-zero bias a few levels up due to the sheer magnitude of the inversion; small differences in the analysis inversion could shift the bias from positive to negative between levels in the MABL. The dewpoint bias curve demonstrated the HRRR's overestimation of the near-surface dewpoint in the MABL and underestimation above the MABL on average. Given

the large spread of the 25th and 75th percentiles however, there was some uncertainty as to the magnitude and sign of the bias at every level. The same cannot be said for the temperature – the tight spread of the percentiles were predominately negative, especially above the MABL height around 200 m.

To see if the patterns observed for the HRRR analyses persisted for the short-range forecasts, the RMSE and bias were computed for the HRRR's 3, 6, 9, and 12 h forecasts, plotted in Figs. 20 and 21. Overall, the errors and biases structures exhibited for the 0 h analyses translated to the HRRR forecasts, regardless of the forecast duration. Temperature RMSE values within and above the MABL continued to average around 2 °C, meaning the biases discussed prior were not unique to the analysis data. From the temperature bias profile, the forecasts trended more towards a cooler MABL on average than the HRRR 0 h analyses did, particularly for the 3 and 6 hr forecasts. However, there was still a decent bit of spread between individual HRRR forecasts given how sharp and shallow the MABL's inversion was. And just like the HRRR 0 h analyses, all the forecasts converged on an average cold bias above the MABL at roughly the same magnitude of -1.5 °C with low spread given the tight range of the temperature percentiles. Like the temperature bias, the vertical distribution of the dewpoint errors were relatively unchanged between the analyses and forecast data, except for a larger dewpoint bias above the MABL for the longer-range 6 through 12 h forecasts. The dewpoint RMSE visualizes this well with higher RMSE values around 3 °C above 500 m for these forecasts. The forecasts trended towards a drier atmosphere above the boundary layer as well with average bias values around -2 °C above 500 m for all forecasts, contrasted to the near-zero average bias for the 0 h analyses.

Additionally, the dewpoint upper percentile bound was predominately negative above the MABL, meaning most of the HRRR forecasts underforecasted the vertical distribution of moisture.

c. September 14th, 2023 – Characteristics of the MABL

The time of this mission so late in the warm season led to Lake Michigan SST values that were slightly colder than the surface temperatures across Wisconsin, leading to a well-mixed, neutrally stable MABL environment over Lake Michigan. This was evident with the first Windsond launched during the excursion around 1400 UTC, plotted in Fig. 22. Temperature lapse rates were slightly lower than the adiabatic lapse rate of 9.8 °C km^{-1} from the surface to 850 hPa which denoted the top of the MABL. Along the first half of the transect, the western and northern legs, temperature variability between the Windsonds were negligible with most of the profiles overlapping each other. Any shifts in the temperature profile were unique to the skew-T diagram due to surface pressure biases discussed prior. The lack of variability seen in the temperature profiles also occurred for the dewpoint profiles, apart from Windsonds 1 through 3. A notable dry layer throughout the MABL was present for these Windsonds that was eventually washed out by the time of Windsond 5's launch due to the turbulent mixing of the MABL, homogenizing the moisture distribution. Once this mixing was established, the vertical distribution of moisture remained mostly constant for the rest of the day. Additionally, a significant decrease in moisture was present above 850 hPa for all Windsonds where the boundary layer top was decoupled from the free atmosphere. Kinematically, the winds were weak and predominately out of the east during the morning hours for Windsonds 1 through 5 within the MABL with slightly stronger

northwesterlies aloft. By the time of Windsond 6's launch (e.g., Fig. 22b), the winds were consistently out of the east near the surface in direct contrast to westerly flow in the upper-layers of the MABL, marking the beginning of the lake-breeze circulation.

Along the second half of the transect (e.g., Fig. 23), the lake-breeze circulation persisted with easterly flow in the lower half of the MABL around 5 kts in conjunction with westerly flow towards the upper-layers of the MABL. The consistent westerlies between 900 and 850 hPa in direct contrast to the northerly flow aloft and easterly flow below for Windsonds 13 through 15 (e.g., Fig. 23b) were characteristic of an ongoing lake-breeze circulation. As a result, warmer PBL air was advected along the return flow of the circulation into the upper layers of the MABL, creating a shallow inversion layer between 900 and 850 hPa during the late afternoon. Additionally, sharp decreases in the dewpoint were observed in this layer due to the offshore advection of drier PBL air. Despite this warming effect in the upper half of the MABL, temperature and dewpoint structures surrounding this layer experienced no variability. The depth of the MABL remained around 850 hPa, and the temperature and dewpoint lapse rates remained consistent with the first half of the transect. The only notable difference was a moistening of the entire MABL column after Windsond 8's launch around 1800 UTC, shifting the dewpoint profile to the right. Overall, the structures seen at the start of this mission persisted for the remainder of the day, just like the June 1st mission, despite the vastly different stability regime present here.

Assessment of the MABL's spatiotemporal evolution was performed using the height-based coordinates, plotted in Figs. 24 and 25. Similar to the June 1st mission, marginal warming of the MABL occurred with time between the start and end of the

mission. However, the magnitude of this warming was significantly less than what was observed during the early warm season. Along the first half of the transect, the temperature profiles were nearly identical in terms of their lapse rates, MABL depth around 1500 m, and temperature magnitude at each height level. The same was true for the dewpoint profiles except for the vertical turbulent mixing of moisture between Windsonds 3 and 5 leading to a more consistent distribution of moisture. Post Windsond 5, the dewpoint profiles had the same vertical structure for the remainder of the mission.

The stagnation of the MABL environment along the second half of the transect was even more apparent along the height coordinates as seen in Fig. 25. Especially in the lower half of the MABL below 500 m, the temperature profiles were identical for all Windsonds with marginal warming further aloft for Windsonds 8 through 12 (e.g., Fig. 25a). The previously identified moistening of the MABL was visible along the height coordinates for the latter half of the Windsonds, but without any modifications to the dewpoint lapse rates. To put the lack of variability across this mission into perspective, a comparison of the MABL profile at the first, middle, and last launch sites were plotted in Fig. 26. Over the 8 h excursion, temperature throughout the MABL only warmed by approximately 1 °C near the surface and 2 °C in the MABL's upper layer. Lastly, despite the well-mixed nature of the MABL environment, the depth of the boundary layer remained constant, evidenced by the consistent height of the isothermal layer and large dewpoint decrease around 1300 m.

d. Model Verification of the September 14th MABL Structure

Skew-T profile comparisons of the HRRR 0 h analyses and the Windsonds were plotted in Figs. 27, 28, and 29. Generally, the HRRR's depiction of the temperature

profile matched well with the observations, effectively capturing the neutral stability and depth of the MABL around 850 hPa, for all the Windsonds. Almost immediately however, the HRRR had a cold bias compared to the Windsonds during the morning and early afternoon hours. This bias extended from the surface to the top of the MABL, and into the free atmosphere for Windsonds 1 through 13. The presence of this cold bias was very similar to the bias observed with the June 1st case. At a magnitude of roughly 2 °C for Windsonds 1 through 9, the cold bias decreased later in the afternoon with the HRRR more closely matching the observed temperature profiles. By the time of Windsonds 14 and 15 (e.g., Fig. 29), the temperature profiles were nearly identical at all pressure levels.

The HRRR derived dewpoint profiles were slightly more variable than the temperature profiles when compared against Windsond observations. For Windsond 1, the HRRR struggled to capture the dry layer throughout the MABL, leading to a large moist bias throughout the boundary layer. Once this dry layer was washed out, the HRRR analyses then underrepresented the vertical distribution of moisture with a persistent dry bias for the remainder of the mission. One exception was the analysis profiles of Windsonds 9 and 11 with the model's dewpoint profiles being a bit more representative of the observed moisture content. The last parameter of interest was the HRRR analyses' representation of the wind profiles throughout the MABL. Overall, the HRRR was effective at resolving the wind speeds and directions near the surface and aloft at all timesteps. One minor discrepancy was an underestimation of the wind speed during the morning hours for Windsonds 1 through 9 (e.g., Figs. 27 and 28). While the winds were too weak to be visualized as barbs, analysis of the wind components

confirmed the HRRR accurately represented the wind direction for these sondes. Additionally, the lake-breeze depth and timing were modeled effectively in the 0 h analyses. As discussed before, the lake-breeze circulation was well established by Windsond 5 (1700 UTC) of which the HRRR's u component of the wind was negative from the surface up to 900 hPa. Later in the afternoon, the wind HRRR and Windsond wind profiles were nearly identical around 2000 UTC up to the last observation around 2300 UTC, resolving both the onshore flow in the MABL and the offshore flow atop the circulation.

The average errors and biases with height were determined for the September 14th mission by computing the vertical RMSE and bias profiles for the temperature and dewpoint. For the 0 h analyses (e.g., Fig. 30), the average temperature RMSE values were around 2 °C immediately near the surface along with a negative temperature bias at the same magnitude. Despite the cold bias near the surface, temperature errors for the rest of the MABL were lesser, up to 1500 m, at approximately 1 °C. Furthermore, the tight spread in the temperature bias percentiles demonstrated the HRRR's cold biases were persistent for much of the mission. While the temperature errors and biases were evenly distributed vertically, the dewpoint biases were dramatically more variable, especially at the top of the MABL. The HRRR 0 h analyses had a slight moist bias on average near the surface that quickly translated to a dry bias further aloft, yet not all the HRRR analyses had this dry bias considering the 75th percentile in the lower half of the MABL was positive. Additionally, the magnitude of the biases was variable between HRRR analyses given the wide range of the shaded percentile regions shown in Fig. 30. Above the top of the MABL at 1500 m, the dewpoint biases and errors were highly

variable due to the sharp decrease in dewpoint exhibited at top of the boundary layer seen prior from the skew-T analysis. The HRRR was unable to resolve the drop in the dewpoint because the model does not have enough vertical levels at that height to faithfully represent the feature. Thus, the dewpoint RMSE and bias values were significantly large in this layer, shifting from positive to negative as the dramatic dewpoint lapse rates were not captured by the model.

Computations of the RMSE and bias for the HRRR forecasts yielded similar RMSE and bias structures as the 0 h analyses. Between the forecasts plotted in Figs. 31 and 32, the average temperature biases were predominately negative at all height levels at a similar magnitude seen in the 0 h analyses. The average temperature biases were around -2 °C near the surface and -1 °C aloft for all forecasts. Additionally, the range of the temperature biases' 25th and 75th percentiles progressively increased with longer forecast durations at all levels but remained predominately negative. This was not too surprising considering longer-range forecasts have higher uncertainty due to errors in initial conditions. However, what was surprising was the decrease in HRRR moisture uncertainty for the longer-range forecasts. Seen in Figs. 31 and 32, the range of the dewpoint percentiles were the lowest for the 9 and 12 h forecasts, despite no notable change in the dewpoint bias profiles compared to the prior forecasts and 0 h analyses. The dewpoint biases were predominately negative at the surface and positive further aloft at roughly similar magnitudes in the MABL for all forecasts. Lastly, the large variability in the dewpoint bias above the MABL recurred for the forecasts which was to be expected considering these errors were due to low vertical resolution of the model. Thus, it would seem that the HRRR analyses and short-range forecasts were resolving

unrealistic moisture profiles with high variability, whereas the longer-range forecasts converged on spatiotemporally consistent, yet biased structures.

4. Evaluation and Prediction of the Lake Michigan Lake-Breeze Front

2023 was abnormally warm, allowing for lake-breeze development from early April up to the end of October. Between these months, lake-breezes occurred on approximately 37 % of days along Lake Michigan's western shoreline based on manual assessments of flow patterns and radar-data output. A total of 80 lake-breeze cases were documented under varying stability and flow regimes which the lake-breeze algorithm was tested on all these cases to determine the ability of the algorithm to identify and predict the lake-breeze front. From this analysis, a few key relationships were identified, and a few select cases were used to visualize these relationships across the 2023 warm season.

a. HRRR Analyses vs. Forecasts

One pattern that emerged was a poor representation of the lake-breeze front when using the HRRR 0 h analyses as input for the algorithm, particularly for edge-cases where the thermodynamic and kinematic discrepancies along the boundary were minimal. As will be demonstrated, the HRRR initialization fields often underestimated the magnitude of the lake-breeze front, depicting a weaker transition between the PBL and MABL airmasses. For robust lake-breeze circulations, this is not much of an issue given the low threshold values set for the lake-breeze algorithm. However, for cases with similar PBL and MABL temperatures, or onshore synoptic flow that matched the

advection of the front, the HRRR analysis struggled to emulate boundary layer and wind gradients that were detectable by the algorithm.

Both the June and September *Neeskay* missions had lake-breeze events that would be classified as edge cases. The former case had a strong thermodynamic discrepancy, but a minimal kinematic shift along the boundary due to prevalent easterly flow throughout the day. For the latter case, the temperatures over land were only a few degrees Celsius warmer than the water in conjunction with weak, southerly flow. Under these conditions, the lake-breeze front was either sporadically detected or missed entirely for the HRRR 0 h analyses. This was immediately evident for June 1st when the analyses were compared to HRRR forecasts, plotted in Figs. 33 and 34. Between 1800 and 2000 UTC, the algorithm was unable to capture the observed lake-breeze front's inland progression for the 0 h analyses because the HRRR's realization of the kinematic field was insufficient. However, the shift to forecast data was an immediate improvement that led to detection of the lake-breeze front, consistent with its observed evolution. For the 3 h forecast plotted in Fig. 33, the frontal feature was isolated by the algorithm at 1800 UTC and maintained its detection up to 2000 UTC before model-depicted convective cells along the front washed out the lake-breeze by 2100 UTC. The same was true for the 6 and 9 h forecasts (e.g., Figs. 33 and 34) and those forecasts not shown, like the 1 and 2 h short-range forecasts. Granted these forecasts were not perfect with a few discontinuous points along the western segment of the lake-breeze front, particularly for the 12 h forecast plotted in Fig. 34. However, the forecasted lake-breeze depiction was a massive improvement on the lack of lake-breeze detection from the 0 h analyses.

September 14th's shore-parallel flow resulted in similar problems with the HRRR 0 h analyses, in conjunction with a weaker land-water temperature difference. As seen in Fig. 35, the algorithm struggled to consistently identify the lake-breeze front from its initiation at 1700 UTC to its decay after 2300 UTC, only isolating fragments of the front. Contrasted to the forecast data (e.g., Fig. 36), the short- and longer-range forecasts were able to identify a continuous feature that coincided with the lake-breeze front at all timesteps. Even for 1700 UTC (not shown), the algorithm was able to capture the lake-breeze front along the coastline for all forecast times. Generally, these issues with the initialization data were not unique to these to these cases but were a common issue for onshore and shore-parallel flow regimes due to the weaker discrepancies across the boundary, especially kinematically. For offshore flow regimes, the sharper transition from the PBL to MABL, characteristic of this flow regime's lake-breeze, was well resolved by the HRRR and allowed for more consistent lake-breeze detection for the model's analyses and forecasts. Therefore, small differences between the 0 h analyses and forecasts did not affect the detection skill given the innately high gradients across the lake-breeze front. An example of this is plotted in Fig. 37 for a westerly flow regime during the late spring where the HRRR analyses and forecasts (including those not shown) were all able to capture the lake-breeze front's initiation and progression along Lake Michigan's western shoreline. Given the tendency for the algorithm to capture the lake-breeze front with HRRR forecasts across different synoptic flow regimes, the HRRR forecasts were primarily used to assess the algorithm's ability to detect the initiation and advection of the lake-breeze front.

b. Influence of the Synoptic Flow Regime on Lake-Breeze Predictability

For offshore flow regimes, the magnitude or direction of the flow had little impact on the skill of the algorithm to detect the lake-breeze front. For example, May 21st had weak westerlies around 5 kts across Wisconsin, allowing for some inland propagation of the lake-breeze front that the algorithm replicated (e.g., Fig. 37). The day prior had a nearly identical thermodynamic environment, but with winds out of the northwest around 10 kts, confining the lake-breeze circulation closer to the shoreline. Under these conditions, the HRRR kept the front closer to the shoreline as seen from radar data in Fig. 38, and the lake-breeze algorithm's forecasts captured its position. As discussed, detection of the lake-breeze was no issue for offshore flow regimes as the 3 and 6 h forecasts all identified the west-shore lake-breeze circulation from its initiation around 1800 UTC to decay post 0000 UTC. While not shown, the longer-range 9 and 12 h forecasts had the same initiation and advection of the front as the prior two forecasts, except with a further southern extent of the frontal boundary into northern Illinois. All the forecasts matched the minimal progression inland whilst maintaining the continuity of the frontal feature. Even under the stronger flow regime present for this case, the algorithm had minimal biases and faithfully depicted the lake-breeze front's evolution.

Onshore flow regimes were more likely to be missed by the algorithm, but still maintain a high agreement between different forecasts from the HRRR. This was true for the June 1st *Neeskay* mission with its similar frontal initiation, positioning, and advection between forecasts under a weak east-southeasterly flow regime. June 18th had a similar wind direction, but faster wind speeds leading to significantly more inland propagation of the lake-breeze front, visualized from radar output in Figs. 39 and 40.

When comparing the forecast output, generally there were minimal differences in the advection speed or placement of the lake-breeze frontal feature. Particularly at 2000 and 2300 UTC, the positioning of the lake-breeze front was well agreed upon by the forecast data, albeit some minor errors for specific forecasts. For example, the 3 and 12 h algorithm forecasts missed portions of the front further north across southern Wisconsin that the 6 and 9 h forecasts captured well. By 2300 UTC however, errors were minimal, and all forecasts depicted the fast acceleration of the front further north due to faster easterly winds consistent with the observed radar output. The main forecast error was during the early stages of the front's progression at 1700 UTC with the 6 through 12-hour forecasts struggling to capture the initial advection of the boundary in southern Wisconsin. However, as the lake-breeze front progressed further inland, the algorithm forecasts converged on a similar solution that well represented the observed evolution of the lake-breeze front. Therefore, under the stronger onshore flow regime, it did not appear that the algorithm's performance between forecasts was significantly impacted by this discrepancy compared to the June 1st case.

When comparing the forecast skill of the algorithm between the offshore and onshore flow regime, regardless of the flow magnitude, it was clear that the offshore flow regimes presented minimal issues for lake-breeze detection. The larger thermodynamic and kinematic differences exhibited by offshore flow regimes were less sensitive to differences in the forecast fields of the HRRR, leading to high skill in lake-breeze prediction for these cases regardless of forecast time. Additionally, the algorithm forecasts matched onto the observed evolution of the lake-breeze front, effectively capturing the initiation and inland propagation of the lake-breeze front. The onshore flow

regimes were the most difficult to identify given the nature of the diffuse lake-breeze boundary, yet the discrepancies in lake-breeze evolution were minimal between forecasts. The issues innate to onshore flow regimes, such as fragmentation and frontal extent, were occasionally present for these algorithm forecasts as seen with the discussed cases. However, what was not seen were large differences between the algorithm forecasts in the initiation timing and propagation magnitude of the lake-breeze front. Despite the sensitivities of the algorithm to the gradients across the lake-breeze under the onshore flow regime, the presence of a lake-breeze front was well agreed upon by the HRRR forecasts.

c. Influence of the MABL Stability Regime on Lake-Breeze Predictability

The cases discussed in the previous section focused mostly on the early warm season during the late spring/early summer, yielding skillful forecasts of the lake-breeze front. For late warm-season cases, the performance of the algorithm was not hindered by weaker MABL stability and lower thermodynamic differences between the PBL airmass. For a late-season offshore lake-breeze case across Lake Michigan's western shoreline, such as August 28th plotted in Fig. 41, the performance of the algorithm was similar to the early warm season cases. Detection of the lake-breeze front in its early stages was captured by all forecasts at 1900 UTC with an extent that closely matched the observed radar line of the lake-breeze front. Given the winds were out of the southwest around 5 to 10 kts throughout the day, the observed lake-breeze front remained closer to the shoreline, of which the algorithm represented through its 3 and 6 h forecasts at 2100 and 2300 UTC. Furthermore, the agreement between the forecasts in terms of extent and positioning of the lake-breeze front was strong throughout the

front's evolution. Compared to cases analyzed earlier in the warm season, the forecast skill of this case and others like it does not present any new challenges. The lesser stability of the MABL during the late season was not sufficient to warrant a boundary layer height gradient insignificant enough to be missed by the algorithm. While a weakly stable or unstable environment across the MABL may prevent lake-breeze development in the model or observationally, it had little impact on the ability of the algorithm to detect a resolved lake-breeze within the HRRR under offshore flow.

Under onshore flow during the late warm season, the stability of the MABL also did not have a significant impact on lake-breeze prediction with the algorithm. As seen in Fig. 42, the algorithm had no difficulty identifying a late September lake-breeze under a weakly onshore flow regime with winds out of the east-southeast. At all timesteps shown in Fig. 42, the lake breeze was apparent, both in its extent and propagation inland. The forecasts were very similar to each other with a few discrepancies in the northern and southern extent of the boundary, along with some minor fragmentation in the 3 h forecast. For all the onshore flow cases analyzed thus far, this September 18th case was resolved the most effectively whilst having the weakest temperature and boundary layer height discrepancy across the lake-breeze front. The initiation time was captured well at 1900 UTC, and the propagation speed inland was well represented by the forecasts.

From the assessment of the algorithm thus far, the skill of the lake-breeze algorithm was insignificantly affected by differences in the wind speed, time of year, or stability regime under offshore synoptic flow. As long as a lake-breeze was emulated by the HRRR model, it was picked up by the algorithm with predominately westerly flow.

Under onshore flow, this analysis highlighted the dependency of the algorithm on significant kinematic discrepancies for the lake-breeze front to be isolated by the algorithm. The cases where the wind direction behind the lake-breeze front most closely matched the synoptic flow were the most difficult to predict, such as the two June cases, leading to fragmentation and discontinuity along the predicted front. Thus, the September 18th case was able to best resolve the lake-breeze front because of the shift from easterlies to east-southeasterlies behind and ahead of the front, respectively. The cases without wind directions shifts, even as minimal as the September case, led to inconsistent lake-breeze identification. The forecasted boundary layer height gradient across the lake-breeze front was sufficient for most onshore flow cases, regardless of the stability regime. Therefore, the dependence of the lake-breeze algorithm on the stability regime was determined to be insignificant under the assumption a lake-breeze front was present in the domain.

5. Conclusions

The present research provided an observational dataset that documented the spatial and temporal evolution of the Lake Michigan MABL during the 2023 warm season and validated HRRR model forecasts to assess the model's representation of the MABL's evolution. Two field missions were conducted to the east of the Port of Milwaukee in which thirty total vertical radiosonde profiles were collected utilizing the Windsond system. The Windsond thermodynamic and kinematic profiles were compared against each other for each mission to determine the characteristics of the MABL under a strongly stable and unstable regime. Additionally, the ability of the HRRR to resolve lake-breeze circulations along Lake Michigan's western shoreline was

determined through the development of a lake-breeze detection algorithm. The algorithm was applied to HRRR analyses and forecasts to qualitatively assess the algorithm's performance in detecting the lake-breeze front and forecasting its evolution.

For the June 1st and September 14th *Neeskay* excursions, the vertical structure of the MABL remained consistent throughout each measurement period, regardless of the seasonal differences. The MABL on June 1st was incredibly shallow and stable due to the advection of warm PBL temperatures atop the cold Lake Michigan SSTs. The lake SSTs were significantly warmer for the September 14th excursion, resulting in a deeper, well mixed, and unstable MABL. Additionally, the June mission had predominately weak easterly flow throughout the entire day, whereas the September mission had weak southerly flow. Our observations demonstrated the combination of a persistent synoptic regime with the high specific heat capacity of Lake Michigan, resulted in an MABL environment that experienced little to no evolution on diurnal time scales. This was especially true further away from the shoreline where land based PBL influences were minimal. Without large shifts in the synoptic conditions, MABL depth and stability was unchanged for each mission, regardless of location or time. Furthermore, the observed variability in the SSTs spatially had a negligible impact on the observed MABL structures. For June 1st especially, a moderate SST gradient was measured from east to west of the *Neeskay* as seen in Fig. 10, courtesy of Dr. Russel Cuhel. However, the warmer water temperatures to the west did not induce significant warming within the MABL, even near the surface.

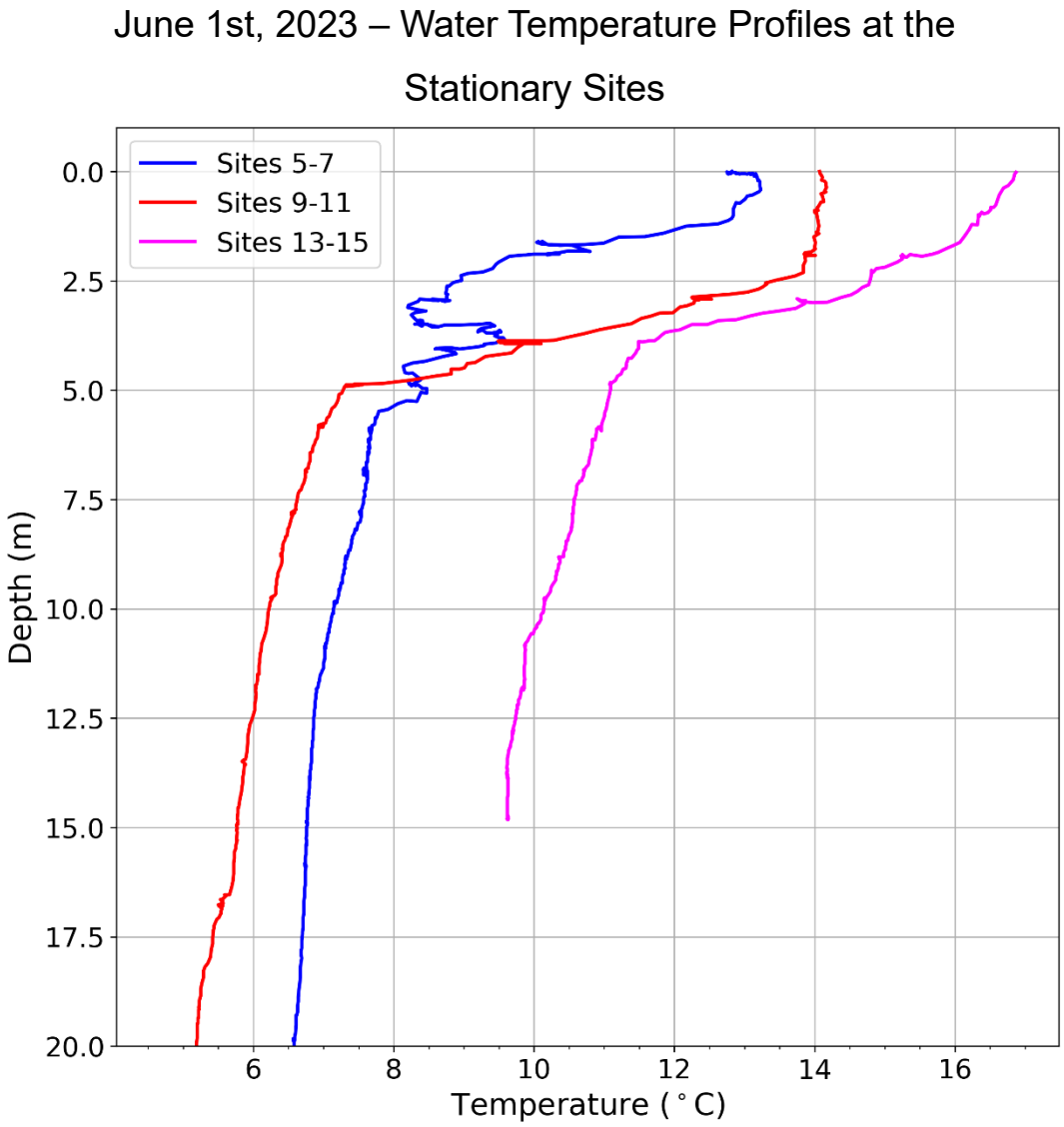

FIG 10. June 1st, 2023, vertical profiles of the water temperature measured off the *Neeskay* at the three sites where the boat was stationary for an hour. Data was measured and collected by Dr. Russell Cuhel of the School of Freshwater Sciences at UWM.

The characteristics of the MABL were primarily dependent upon the airmass being advected over the water and the modifications to that airmass. The advection of a warm airmass over the cold water, which occurs more frequently in the early warm season, established a shallow, stable MABL whose stability and depth was dependent upon the differential between the SSTs and the land-based temperature. Consequently, when a cooler airmass was advected over a warm Lake Michigan, frequently during the

late warm season, a deep and well-mixed MABL environment persisted. Thus, any modifications to the MABL were a result of changes in the advected PBL airmass. For the June 1st case, the magnitude of the inversion increased later in the afternoon due to diurnal heating of the advected airmass over land. The nearshore Windsonds also captured some vertical mixing near the surface. One hypothesis is the warmer SSTs suppressed allowed for near-surface mixing near the shoreline, yet this was unable to be confirmed without measured lake temperatures during the first half of the transect. The only variations the September 14th MABL experienced was a marginal warming of the MABL column to a lesser degree than the June case due to lower diurnal heating over land. Modifications to the dewpoint structure throughout the MABL were also minimal for both cases, apart from the September case with vertical mixing homogenizing the moisture content during the early morning hours. Once moisture distribution was established in the MABL however, it persisted for the remainder of the day for both excursions.

When comparing the HRRR vertical profiles to the Windsond dataset, one pattern defined both cases – the cold bias – regardless of the location, stability, or flow regime. The only exception was a few soundings late in the afternoon near the shoreline for the September case. The magnitude of the cold bias for the June case was not expected, especially when the extent of the bias exceeded the depths of the MABL. With the new stability regime for the September case, the cold bias was hypothesized to be absent, yet it manifested in a nearly identical manner, opening the possibility of a model deficiency in marine environments during the warm season. The persistence of this cold bias suggests the HRRR is underestimating the turbulent vertical mixing in the

MABL as warmer temperatures, whether from the surface or aloft, were not being properly distributed to the MABL. However, this appeared to have a more variable impact on the model's dewpoint profiles as its biases were not consistent with height or between cases. There was strong agreement between the HRRR analyses and forecasts as to the sign of the bias at specific layers within and above the MABL. For example, the HRRR overestimated the moisture near the surface and underestimated the moisture in the upper layers of the MABL and aloft for the June 1st case. A similar pattern was present on September 14th, but with significantly more variation in the moisture bias further aloft due to the model's inability to capture the significant drop in moisture at the top of the MABL. However, these two cases were not sufficient to establish a persistent moisture bias over Lake Michigan, especially considering the high spread of the biases against individual Windsonds.

Analysis of the lake-breeze detection algorithm demonstrated its utility identifying and predicting the evolution of the lake-breeze front. Comparisons of the algorithm's output with HRRR 0 h analyses and forecasts demonstrated the forecast data had a higher skill than the analysis data, particularly for onshore flow regimes as the analyses struggled to resolve significant enough discrepancies across its modeled lake-breeze fronts. For offshore flow regimes, this was less of an issue due to the sharp contrast in the MABL and PBL that occurs when the lake-breeze front's advection opposes the large-scale flow. In the context of the lake-breeze algorithm's purpose, the tendency of HRRR analyses to underestimate thermodynamic and kinematic discrepancies is irrelevant, as long as the defined algorithm thresholds are met. Although the lake-breeze front can already be easily identified via in-situ ASOS data and remotely sensed

radar data across Lake Michigan's coastline, it cannot be predicted with these instruments. The lake-breeze algorithm provides the unique utility of predicting the initiation, spatial extent, and inland progression of the lake-breeze front with high skill throughout the warm season. Based on output of the algorithm alone, one can estimate the initiation timing, spatial extent, propagation magnitude, and decay to inform coastal forecasts across the Great Lakes.

Beyond the 0 h analysis, the detection algorithm is subjectively able to skillfully identify and assist in tracking the evolution of the lake-breeze front across a wide range of stability and flow regimes. Especially for the offshore flow regime, the lake-breeze algorithm consistently identified the lake-breeze front and accurately represented its inland propagation. Because of the innate thermodynamic contrast across the lake-breeze front under offshore flow, the algorithm was not sensitive to variations the resolved boundary layer or wind gradient for this flow regime. Comparison of the algorithm forecasts to the observed advection of the lake-breeze front demonstrated the HRRR's ability to accurately predict the magnitude of inland propagation based on the synoptic wind magnitude. With onshore synoptic flow, the lake-breeze algorithm was able to detect the lake-breeze front and faithfully propagate the boundary inland in agreement with the observations. However, the boundaries were occasionally fragmented, leading to segments of the lake-breeze front being detected rather than continuous frontal features. While the spatial extent of the frontal feature was not always captured by the lake-breeze forecasts, particularly along the northern and southern legs of the lake-breeze front, the segments of the front that were detected by the algorithm

did coincide with the observed position of the front with little variance between forecasts.

Analysis of the lake-breeze algorithm for onshore flow regimes demonstrated the root of the lower skill was not thermodynamic, but kinematically driven. The more similar the wind direction was ahead of and behind the front, the more likely the algorithm was to miss that portion of the lake-breeze front due to insignificant u and v wind gradients across the boundary. While the lake-breeze circulation produces mesoscale pressure-gradient forcing and flow acceleration behind the front, this acceleration alone struggled to meet the kinematic threshold consistently without some shift in wind direction as well. Under these conditions, detection of the lake-breeze front was not impossible, but rather the algorithm was more sensitive to minor shifts in the wind direction along segments of the boundary. Both June cases exhibited this relationship as portions of the lake-breeze front were captured by the algorithm by the HRRR forecasts at numerous, yet discontinuous, locations along the boundary. Whilst the onshore flow regimes were deemed to be the most difficult to isolate with the algorithm, there was skill in predicting the evolution of the onshore flow lake-breeze front with the lake-breeze detection algorithm.

The lake-breeze algorithm provides a new avenue for lake-breeze prediction in the Great Lakes region that expands upon prior methods towards lake-breeze frontal prediction. This research demonstrated that the HRRR model is capable of faithfully resolving the lake-breeze circulation and its frontal boundary can be effectively isolated amongst the noise of the model domain. Furthermore, the algorithm allows for the prediction of the lake-breeze beyond a simple determination of whether a lake-breeze

will occur across the Great Lakes, providing valuable information on the expected propagation, timing, and decay of the frontal boundary. Future research into the efficacy of model-based prediction of the lake-breeze using an algorithm like the one discussed here would benefit greatly from more case analysis that evaluates the model's performance after the lake-breeze front propagates inland. For example, surface observations inland can be utilized to evaluate the model's performance post lake-breeze front passage at a given location. Results from these analyses would provide valuable information as to *why* the model performs well or struggles to resolve the lake-breeze front. Additionally, the lake-breeze algorithm has the potential to be utilized for different coastal environments to predict the lake-breeze for other large lakes, or to detect the sea-breeze along ocean coastlines.

REFERENCES

Allegretti, S., F. Bolelli, M. Cancilla, F. Pollastri, L. Canalini, C. Grana, 2019: How does connected components labeling with decision trees perform on GPUs?. *CAIP 18th Int. Conf.*, Salerno, Italy, https://doi.org/10.1007/978-3-030-29888-3_4.

Arritt, R. W., 1987: The effect of water surface temperature on lake breezes and thermal internal boundary layers. *Bound-Layer Meteor.*, **40**, 101–125, https://doi.org/10.1007/bf00140071.

AWS: NOAA High-Resolution Rapid Refresh (HRRR) Model, https://registry.opendata.aws/noaa-hrrr-pds

Bellaire, F. R., 1965: The modification of warm air moving over cold water. *Proc. 8th Conf. Great Lakes Research*, IAGLR, 249–265

Benjamin, S. G., and Coauthors, 2016: A North American hourly assimilation and model forecast cycle: The Rapid Refresh. *Mon. Wea. Rev.*, **144**, 1669–1694, https://doi.org/10.1175/MWR-D-15-0242.1.

Benjamin, S.G., T.G. Smirnova, E.P. James, E.J. Anderson, A. Fujisaki-Manome, J.G.W. Kelley, G.E. Mann, A.D. Gronewold, P. Chu, and S.G.T. Kelley, 2022: Inland lake temperature initialization via coupled cycling with atmospheric data assimilation. *Geosci. Model Dev.*, **15**, 6659–6676, https://doi.org/10.5194/gmd-15-6659-2022.

Bessardon, G.E.Q., K. Fosu-Amankwah, A. Petersson, and B.J. Brooks, 2019: Evaluation of Windsond S1H2 performance in Kumasi during the 2016 DACCIWA

field campaign. *Atmos. Meas. Tech*, 12, 1311–1324, https://doi.org/10.5194/amt-12-1311-2019.

Biggs, W. G., and M. E. Graves, 1962: A lake breeze index. *J. Appl. Meteor.*, **1**, 474–480, https://doi.org/10.1175/1520-0450(1962)001<0474:ALBI>2.0.CO;2.

Blumberg, W. G., K. T. Halbert, T. A. Supinie, P. T. Marsh, R. L. Thompson, and J. A. Hart, 2017: SHARPpy: An open-source sounding analysis toolkit for the atmospheric sciences. *Bull. Amer. Meteor. Soc.*, **98**, 1625–1636, https://doi.org/10.1175/BAMS-D-15-00309.1.

Bradski, G., and A. Kaehler, 2008: *Learning OpenCV: Computer vision with the OpenCV library.* 1st ed. O'Reilly Media, 555 pp.

Chen, C., R.C. Beardsley, and G. Cowles, 2006: An unstructured grid, finite volume coastal ocean model (FVCOM) system. *Oceanography*, **19**, 78–89, https://doi.org/10.5670/oceanog.2006.92.

Crossman E. T., and J. D. Horel, 2010: Sea and lake breezes: a review of numerical studies. *Bound.-Layer Meteor.*, **137**, 1–29, https://doi.org/10.1007/s10546-010-9517-9.

Dave Ahijevych, 2023: NCAR image archive – meteorological case study selection kit. Accessed 19 March 2024, https://www2.mmm.ucar.edu/imagearchive.

Diedrichsen, M., M.C. Coniglio, E. Rasmussen, S.M. Waugh, 2023: A targeted sounding and LiDAR retrieved wind analysis of the 26 February 2023 Norman, OK tornado. *32nd Conf. on Weather Analysis and Forecasting/28th Conf. on Numerical*

Weather Prediction/20th Conf. on Mesoscale Processes, Madison, WI, https://ams.confex.com/ams/WAFNWPMS/meetingapp.cgi/Paper/425474.

Donlon, C.J., P.J. Minnett, C. Gentemann, T. Nightingale, I.J. Barton, B. Ward, and M.J. Murray, 2002: Towards improved validation of satellite sea surface skin temperature measurements for climate research. *J. Climate*, **15**, 353–369, https://doi.org/10.1175/1520-0442(2002)015<0353:TIVOSS>2.0.CO;2

Dowell, D. C., and Coauthors, 2022: The High-Resolution Rapid Refresh (HRRR): an hourly updating convection-allowing forecast model. Part I: Motivation and system description. *Wea. Forecasting*, **37**, 1371–1395, https://doi.org/10.1175/WAF-D-21-0151.1.

Dye, T. S., P. T. Roberts, and M. E. Korc, 1995: Observations of transport processes for ozone and ozone precursors during the 1991 Lake Michigan ozone study. *J. Appl. Meteor.*, **34**, 1877–1889, https://doi.org/10.1175/1520-0450(1995)034<1877:OOTPFO>2.0.CO;2.

Hawbecker, P., and J. C. Knievel, 2022: An algorithm for detecting the Chesapeake Bay breeze from mesoscale NWP model output. *J. Appl. Meteor. Climatol.*, **61**, 61–75, https://doi.org/10.1175/JAMC-D-21-0097.1.

Hawbecker, P., and J. C. Knievel, 2022: Simulating the Chesapeake Bay breeze: sensitivities to water surface temperature. *J. Appl. Meteor. Climatol.*, **61**, 1595–1611, https://doi.org/10.1175/JAMC-D-22-0002.1.

Iacono J. M., J. S. Delamere, E. J. Mlwaer, M. W. Shepard, S. A. Clough, and W. D. Collins, 2008: Radiative forcing by long-lived greenhouse gases: calculations

with the AER radiative transfer models. *J. Geophys. Res.*, **113**, https://doi.org/10.1029/2008JD009944.

Iversen, S.C., A.K. Sperrevik, and O. Goux, 2023: Improving sea surface tempeartures in a regional ocean model through refined sea surface temperature assimilation. *Ocean Sci.*, **19**, 729 – 744, https://doi.org/10.5194/os-19-729-2023

James, E. P., and Coauthors, 2022: The High-Resolution Rapid Refresh (HRRR): An hourly updating convection-allowing forecast model. Part II: Forecast performance. *Wea. Forecasting*, **37**, 1397–1417, https://doi.org/10.1175/WAF-D-21-0130.1.

Kingsmill, D. E., 1995: Convection initiation associated with a sea-breeze front, a gust front, and their collision. *Mon. Wea. Rev.*, **123**, 2913–2933, https://doi.org/10.1175/1520-0493(1995)123<2913:CIAWAS>2.0.CO;2.

Klemp, J. B., 2011: A terrain-following coordinate with smoothed coordinate surfaces. *Mon. Wea. Rev.*, **139**, 2163–2169, https://doi.org/10.1175/MWR-D-10-05046.1.

Laird, N. F., D. A. R. Kristovich, X. Z. Liang, R. W. Arritt, and K. Labas, 2001: Lake Michigan lake breezes: climatology, forcing, and synoptic environment. *J. Appl. Meteor. Climatol.*, **40**, 409–424, https://doi.org/10.1175/1520-0450(2001)040<0409:LMLBCL>2.0.CO;2.

Lemone, M. A., M. Tewari, F. Chen, and J. Dudhia, 2013: Objectively determined fair-weather CBL depths in the ARW-WRF model and their comparison to CASES-97 observations. *Mon. Wea. Rev.*, **141**, 30–54, https://doi.org/10.1175/MWR-D-12-00106.1.

Lemone, M. A., M. Tewari, F. Chen, and J. Dudhia, 2014: Objectively determined fair-weather NBL features in ARW-WRF and their comparison to CASES-97 observations. *Mon. Wea. Rev.*, **142**, 2709–2732, https://doi.org/10.1175/MWR-D-13-00358.1.

Lennartson, G. J., and M. D. Schwartz, 2002: The lake breeze-ground-level ozone connection in eastern Wisconsin: a climatological perspective. *International Journal of Climatology*, **22**, 1347–1364, https://doi.org/10.1002/joc.802.

Lyons, W. A., 1970: Numerical simulation of Great Lakes summertime conduction inversions. *Proc. 13th Conf. on Great Lakes Research*, Buffalo, NY, International Association for Great Lakes Research, 369–387

Lyons, W. A., 1972: The climatology and prediction of the Chicago lake breeze. *J. Appl. Meteor.*, **11**, 1259–1270, https://doi.org/10.1175/1520-0450(1972)011%3C1259:TCAPOT%3E2.0.CO;2.

Lyons, W. A., and Cole, H. S., 1973: Fumigation and plume trapping on the shores of Lake Michigan during stable onshore flow. *J. Appl. Meteor.*, **12**, 494–510, https://doi.org/10.1175/1520-0450(1973)012<0494:FAPTOT>2.0.CO;2.

Lyons, W. A., and H. S. Cole, 1976: Photochemical oxidant transport: mesoscale lake breeze and synoptic-scale aspects. *J. Appl. Meteor.*, **15**, 733–743, https://doi.org/10.1175/1520-0450(1976)015<0733:POTMLB>2.0.CO;2.

Markowski, P.M., Y.P. Richardson, S.J. Richardson, and A. Petersson, 2018: Aboveground thermodynamic observations in convective storms from

balloonborne probes acting as pseudo-lagrangian drifters. *Bull. Amer. Meteor. Soc*, **99**, 711–724, https://doi.org/10.1175/bams-d-17-0204.1.

Miller, S. T. K., B. D. Keim, R. W. Talbot, and H. Mao, 2003: Sea breeze: structure, forecasting, and impacts. *Rev. Geophys.*, **41**, 1101, https://doi.org/10.1029/2003RG000124.

Nielsen-Gammon, J. W., and Coauthors, 2008: Multisensor estimation of mixing heights over a coastal city. *J. Appl. Meteor. Climatol.*, **47**, 27–43, https://doi.org/10.1175/2007JAMC1503.1.

Olson, J. B., J. S. Kenyon, W. A. Angevine, J. M. Brown, M. Pagowski, and K. Sušelj, 2019: A description of the MYNN-EDMF scheme and the coupling to other components in WRF-ARW. *NOAA Technical Memorandum OAR GSD-61*, https://doi.org/10.25923/n9wm-be49.

Roebber, P. J. and M. G. Gehring, 2000: Real-time prediction of the lake breeze on the western shore of Lake Michigan. *Wea. Forecasting*, **15**, 298–312, https://doi.org/10.1175/1520-0434(2000)015<0298:RTPOTL>2.0.CO;2.

Schluessel, P., W.J. Emery, H. Grassl, and T. Mammen, 1990: On the bulk-skin temperature difference and its impact on satellite remote sensing of sea surface temperature. *J. Geophys. Res.*, **95**, 341–356, https://doi.org/10.1029/JC095iC08p13341.

Scott R. W., and F. A. Huff, 1996: Impacts of the Great Lakes on regional climate conditions. *J. Great Lakes Res.*, **22**, 845–863, https://doi.org/10.1016/S0380-1330(96)71006-7.

Segal, M., and R. A. Pielke, 1985: The effect of water temperature and synoptic winds on the development of surface flows over narrow, elongated water bodies'. *J. Geophys. Res.*, **90**, 4907–4910

Segal, M., M. Leuthold, R. W. Arritt, C. Anderson, and J. Shen, 1997: Small Lake Daytime breezes: some observations and conceptual evaluations. *Bull. Am. Meteor. Soc.*, **78**, 1135–1148, https://doi.org/10.1175/1520-0477(1997)078<1135:SLDBSO>2.0.CO;2.

Sikora, T. D., G. S. Young, and M. J. Bettwy, 2010: Analysis of the western shore Chesapeake Bay bay-breeze. *Nat. Wea. Digest*, **34**, 55–65, http://nwafiles.nwas.org/digest/papers/2010/Vol34No1/Pg55-Sikora-etal.pdf.

Sills, D. M. L., J. R. Brook, I. Levy, P. A. Makar, J. Zhang, and P. A. Taylor, 2011: Lake breezes in the southern Great Lakes region and their influence during BAQS-Met 2007. *Atmos. Chem. Phys.*, **11**, 7955–7973, https://doi.org/10.5194/acp-11-7955-2011.

Simpson, J. E., 1994: Sea breeze and local Winds. Cambridge University Press, UK, 234 pp

Smirnova T. G., J. M. Brown, S. G. Benjamin, and J. S. Kenyon, 2016: Modifications to the RAPID Update Cycle Land Surface Model (RUC LSM) Available in the Weather Research and Forecasting (WRF) Model. *Mon. Wea. Rev.*, **144**, 1851–1865, https://doi.org/10.1175/MWR-D-15-0198.1.

Smith, B. B., 2001: Development of a lake breeze forecast methodology for northern Michigan. *Nat. Wea. Digest*, **25**, 47–52

Smith, T. M., and Coauthors, 2016: Multi-radar multi-sensor (MRMS) severe weather and aviation products: initial operating capabilities. *Bull. Amer. Meteor. Soc.*, **97**, 1617–1630, https://doi.org/10.1175/BAMS-D-14-00173.1.

Sparv Embedded, 2018: Windsond Manual. Accessed 19 March 2024. https://files.sparvembedded.com/windsond_manual_2.1.pdf

Sparv Embedded, 2019: Windsond product catalogue. Accessed 19 March 2024. https://files.sparvembedded.com/windsond_catalog_Feb2019.pdf

Stauffer, R. M., and A. M. Thompson, 2015: Bay breeze climatology at two sites along the Chesapeake Bay from 1968-2010: Impacts on surface ozone. *J. Atmo. Chem.*, **72**, 2534–2548, https://doi.org/10.1016/j.atmosenv.2006.11.027.

Stauffer, R. M., and Coauthors, 2015: Bay breeze influence on surface ozone at Edgewood, MD during July 2011. *J. Atmo. Chem.*, **72**, 335–353, https://doi.org/10.1007/s10874-012-9241-6.

Stull, R. B., 1988: An Introduction to boundary layer meteorology. *Mean Boundary Layer Characteristics*. R.B. Stull, 1–27.

Tallapragada, V., 2022: Correction of the specification of elevation of the Great Lakes in the High Resolution Rapid Refresh (HRRR): effective on or about July 19, 2022. NWS Headquarters Silver Spring MD, accessed on 13 March 2023, https://www.weather.gov/media/notification/pdf2/scn22-68_hrrr_great_lakes.pdf

Thompson, G., R. M. Rasmussen, and K. Manning, 2004: Explicit forecasts of winter precipitation using an improved bulk microphysics scheme. Part I: Description

and Sensitivity Analysis. *Mon. Wea. Rev.*, **132**, 519–542, https://doi.org/10.1175/1520-0493(2004)132<0519:EFOWPU>2.0.CO;2.

Thompson, G., P. R. Field, R. M. Rasmussen, and W. D. Hall, 2008: Explicit forecasts of winter precipitation using an improved bulk microphysics scheme. Part II: Implementation of a new snow parameterizations. *Mon. Wea. Rev.*, **136**, 5095–5115, https://doi.org/10.1175/2008MWR2387.1.

United States Department of Agriculture: Ozone precursors. Accessed 18 March 2024. https://www.nrcs.usda.gov/sites/default/files/2022-12/Ozone_Precursors.pdf

Wagner T. J., A. C. Czarnetzki, M. Christiansen, R. B. Pierce, C. O. Stanier, A. F. Dickens, and E. W. Eloranta, 2021: Observations of the development and vertical structure of the lake-breeze circulation during the 2017 Lake Michigan ozone study. *J. Atmos. Sci.*, **79**, 1005–1020, https://doi.org/10.1175/JAS-D-20-0297.1.

Wang, J., P. Xue, W. Pringle, Z. Yang, and Y. Qian, 2022: Impacts of lake surface temperature on the summer climate over the Great Lakes region. *J. of Geophys. Res.: Atmospheres*, **127**, https://doi.org/10.1029/2021JD036231.

Watts, A. J., 1955: Sea breeze at Thorney Island. *The Meteorological Magazine*, **84**, 42–48

White, L.D., and D. Lu, 2020: Multi-scale transects of three North American Drylines. *Atmosphere*, **11**, 854, https://doi.org/10.3390/atmos11080854

Zhang, J., and Coauthors, 2016: Multi-radar multi-sensor (MRMS) quantitative precipitation estimation: initial operating capabilities. *Bull. Amer. Meteor. Soc.*, **97**, 621–637, https://doi.org/10.1175/BAMS-D-14-00174.1.

Zhang, X., J. Huang, G. Li, Y. Wang, C. Liu, K. Zhao, X. Tao, X.M. Hu, and X. Lee, 2019: Improving lake-breeze simulation with WRF nested les and lake model over a large shallow lake. *J. of Appl. Meteor. Climatol*., **58**, 1689–1708, https://doi.org/10.1175/JAMC-D-18-0282.1.

APPENDIX A:

Field Mission Vertical Profiles and Model Verification

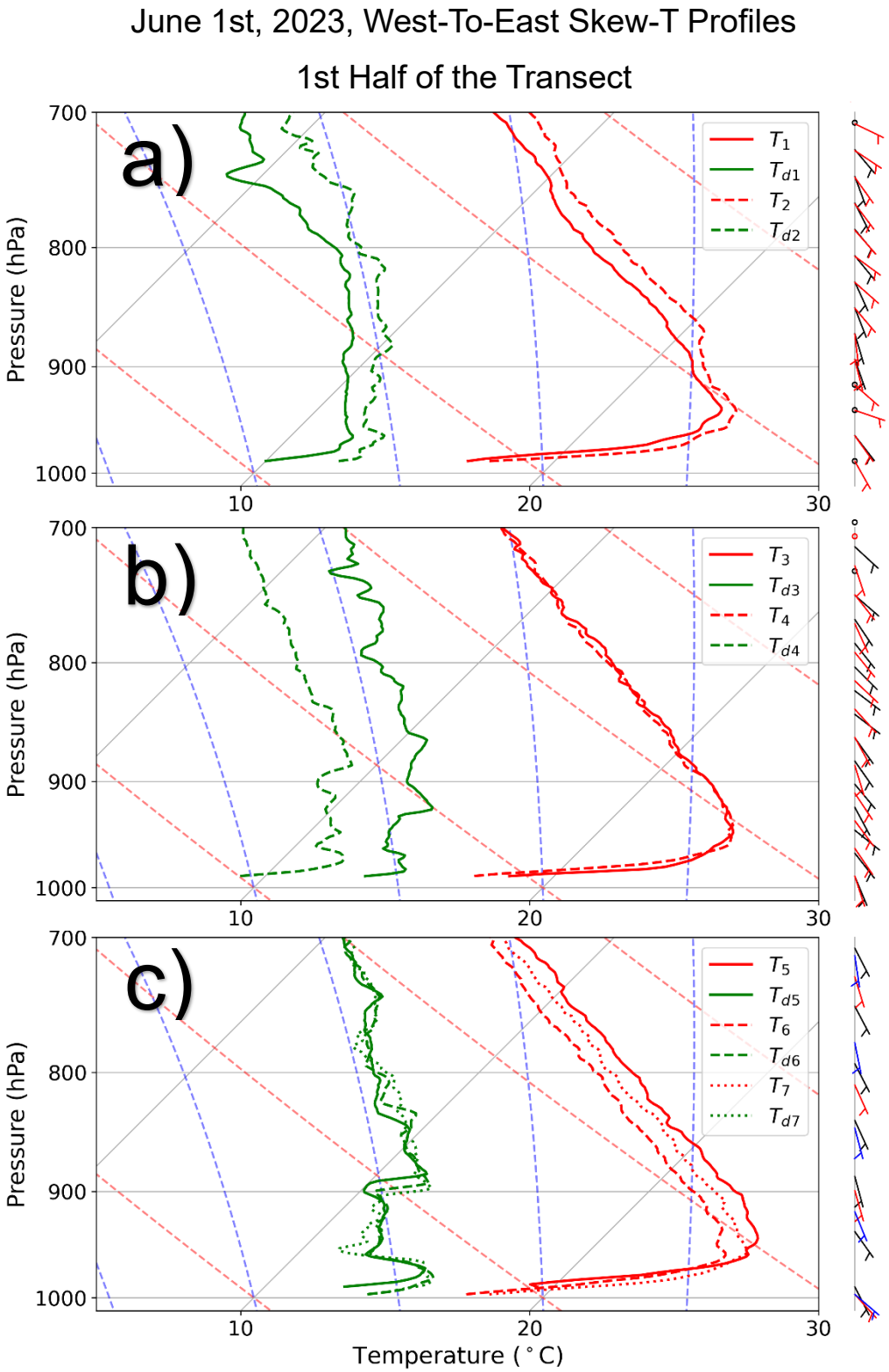

FIG 11. Vertical Skew-T profile comparisons of temperature (red) and dewpoint (green) for Windsonds 1 and 2 (a), 3 and 4 (b), and 5, 6, and 7 (c). Windsond numbers are denoted by the subscripts in the legend. Wind barbs are plotted chronologically according to the Windsond number through a color range of black, red, to blue.

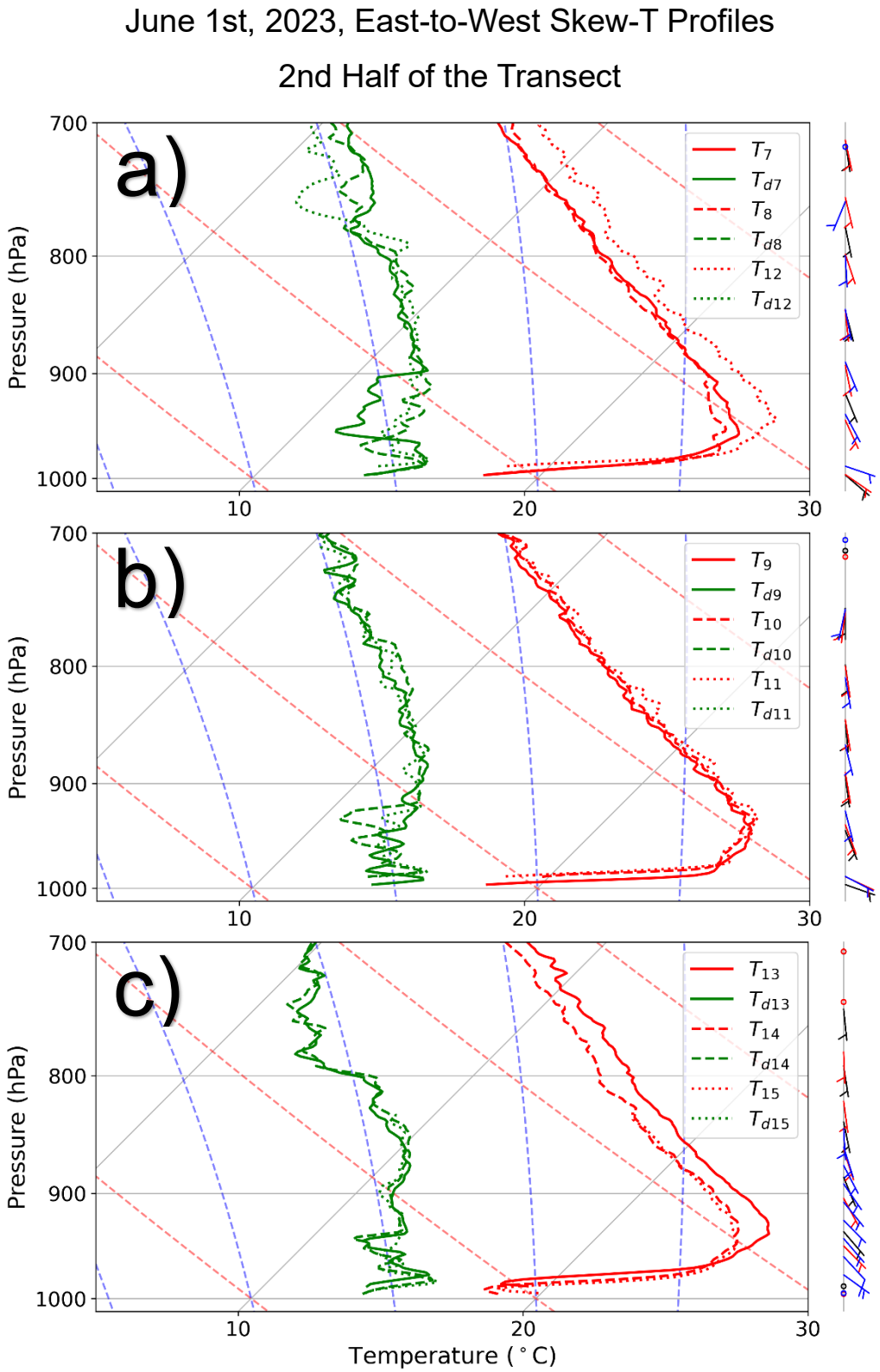

FIG 12. Vertical Skew-T profile comparisons of temperature (red) and dewpoint (green) for Windsonds 7, 8, and 12 (a), Windsonds 9 through 11 (b), and Windsonds 13 through 15 (c). Windsond numbers are denoted by the subscripts in the legend. Wind barbs are plotted chronologically according to the Windsond number through a color range of black, red, to blue.

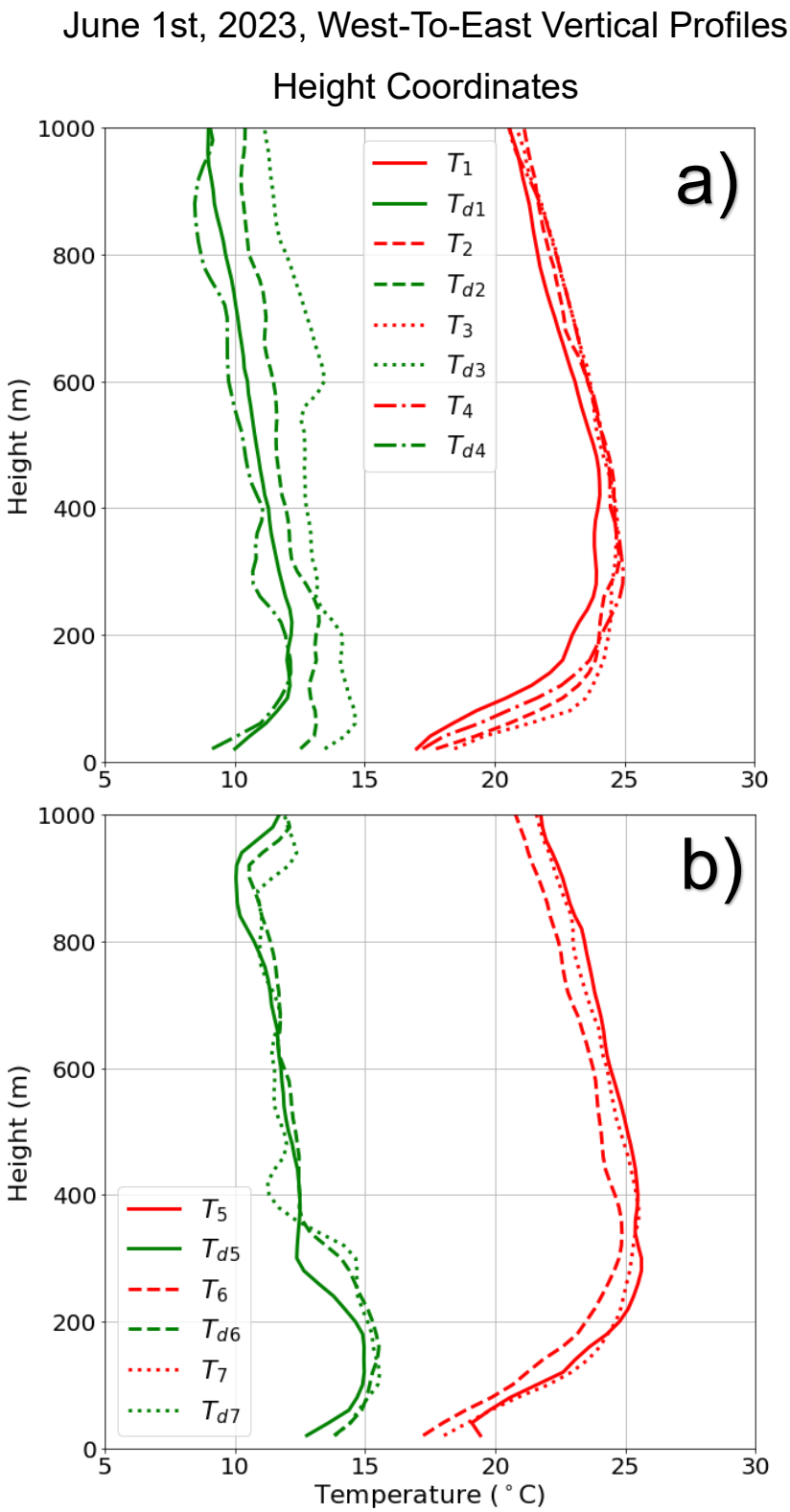

FIG 13. Vertical profile comparisons, using a height-based coordinate system with measurements every 20 m, for temperature (red) and dewpoint (green) for Windsonds 1 – 4 (a) and 5 – 7 (b) for the June 1st, 2023, mission. Windsond numbers are denoted by the subscripts in the legend.

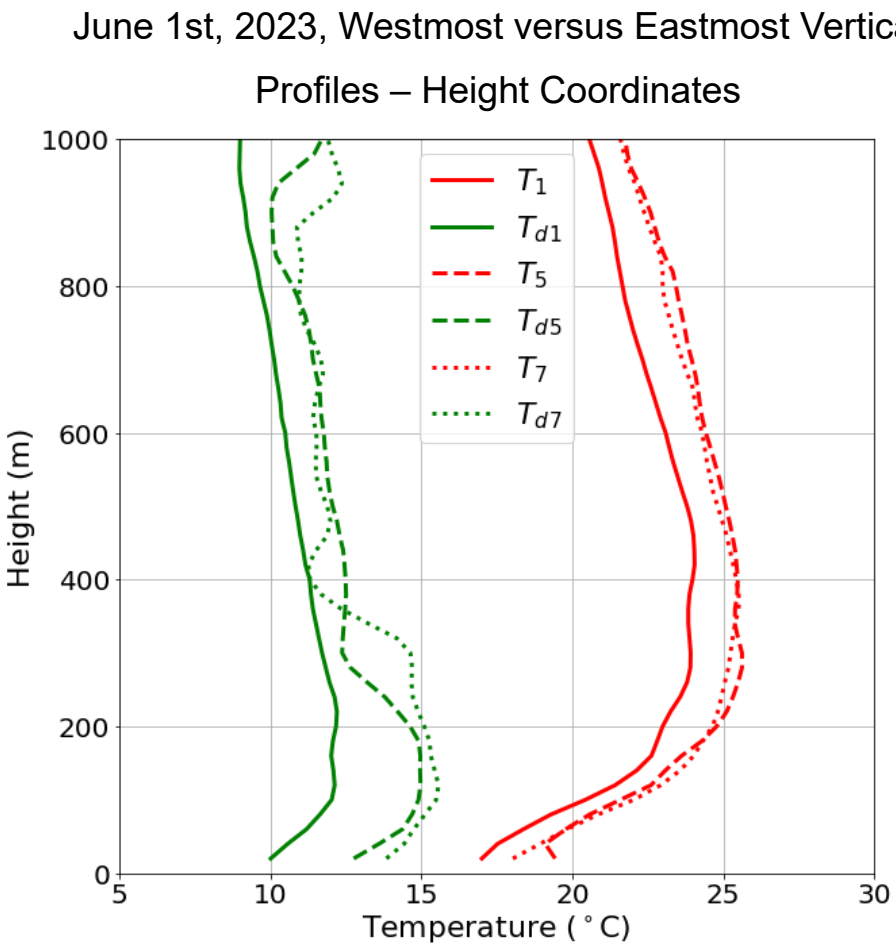

FIG 14. Vertical profile comparisons, using a height-based coordinate system with measurements every 20 m, for temperature (red) and dewpoint (green) for Windsonds 1 (solid), 5 (dashed), and 7 (dash-dot) for the June 1st, 2023, mission.

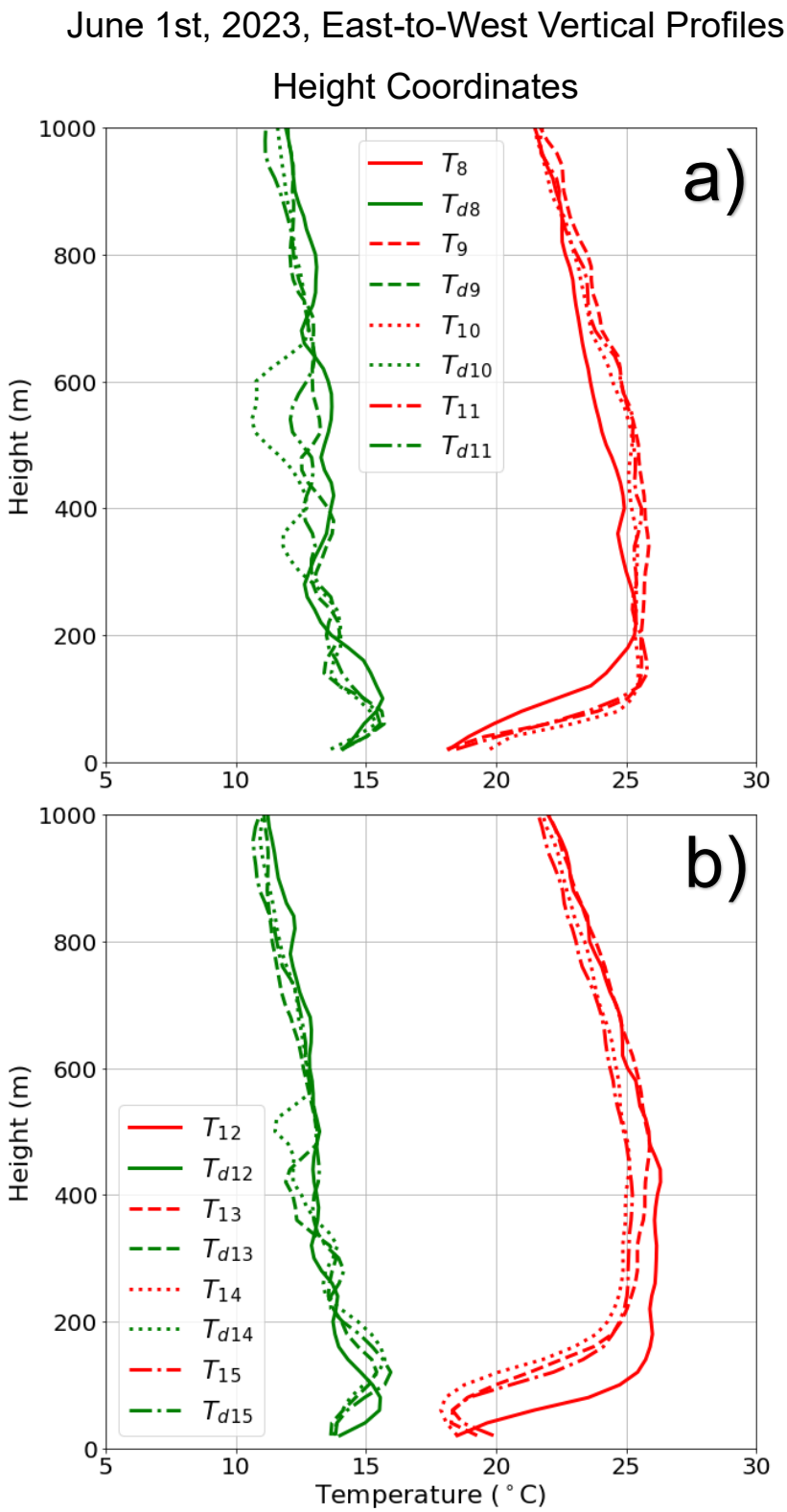

FIG 15. Vertical profile comparisons, using a height-based coordinate system with measurements every 20 m, for temperature (red) and dewpoint (green) for Windsonds 8 – 11 (a) and 12 – 15 (b) for the June 1st, 2023, mission. Windsond numbers are denoted by the subscripts in the legend.

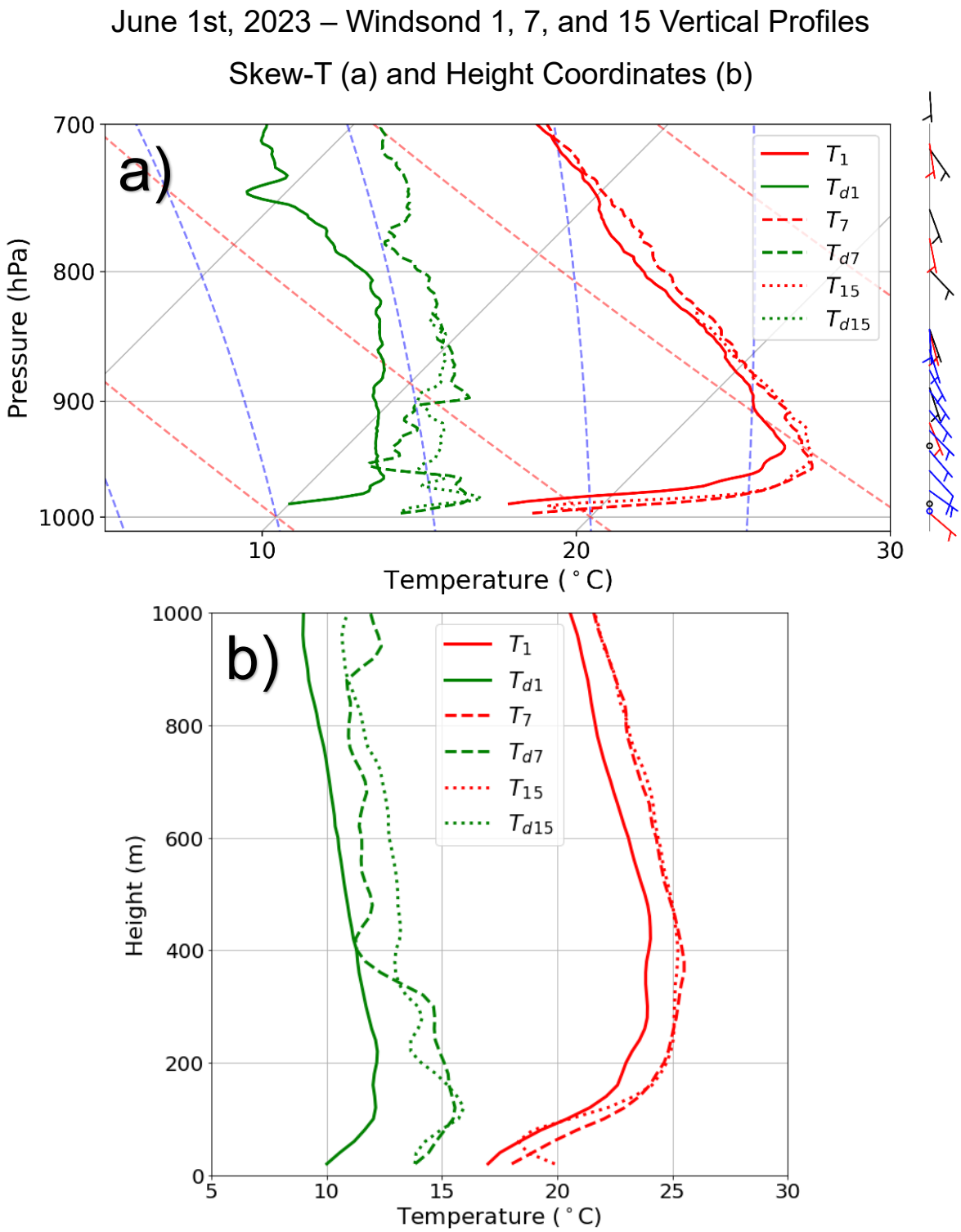

FIG 16. Vertical profile comparisons of Windsonds 1 (solid), 7 (dashed), and 15 (dotted) using a skew-T diagram (a) and a height-based coordinate system diagram (b). Temperature is plotted in red, and dewpoint is plotted in green. Wind barbs are plotted chronologically according to Windsond number through a color range of black, red, and blue.

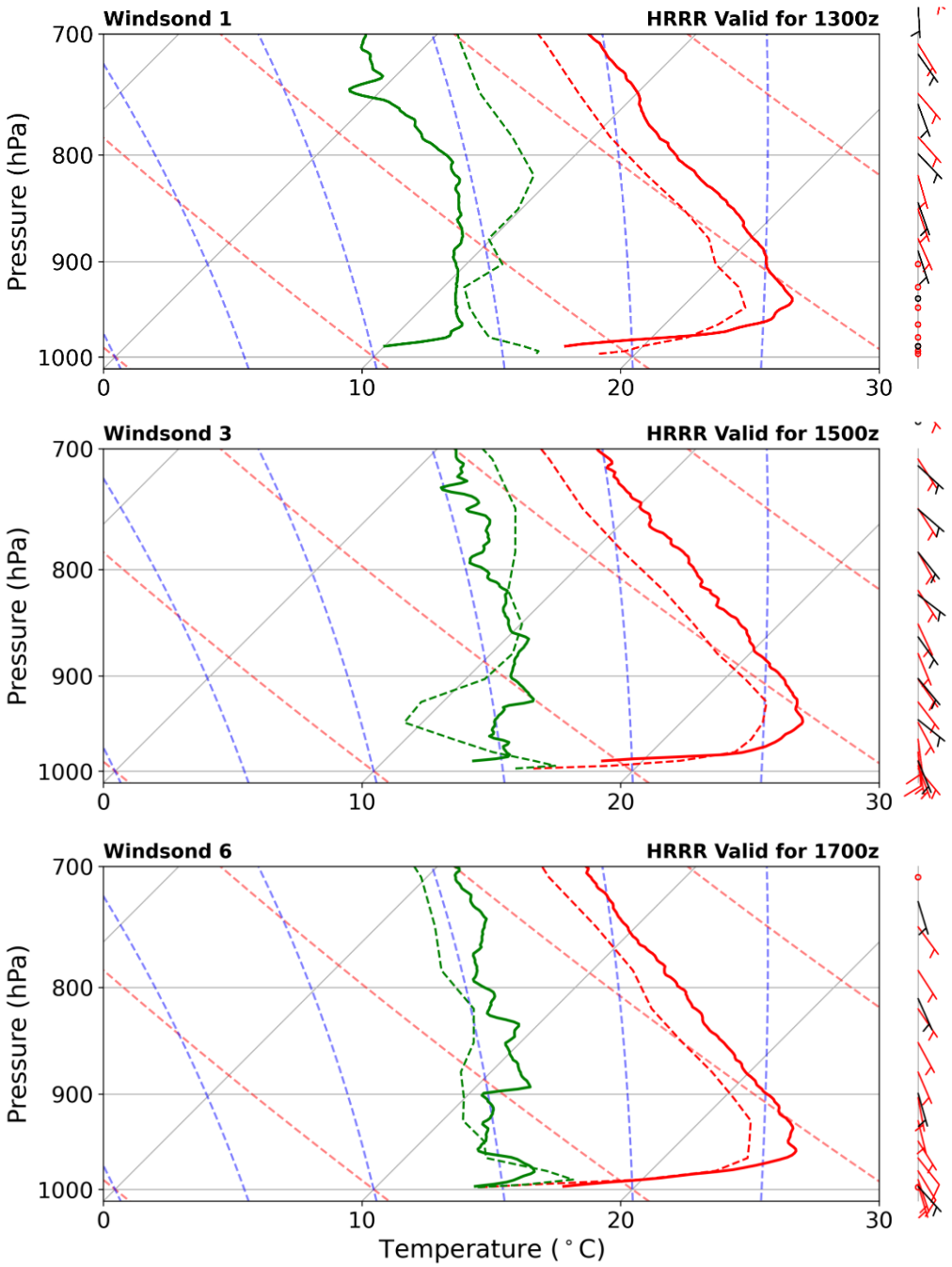

FIG 17. Vertical profile comparisons of Windsonds 1 (top), 3 (middle), and 6 (bottom) versus HRRR 0 h Analyses on June 1st, 2023. Temperature is plotted in red, and dewpoint is plotted in green. Windsond (HRRR) Wind barbs are plotted in black (red).

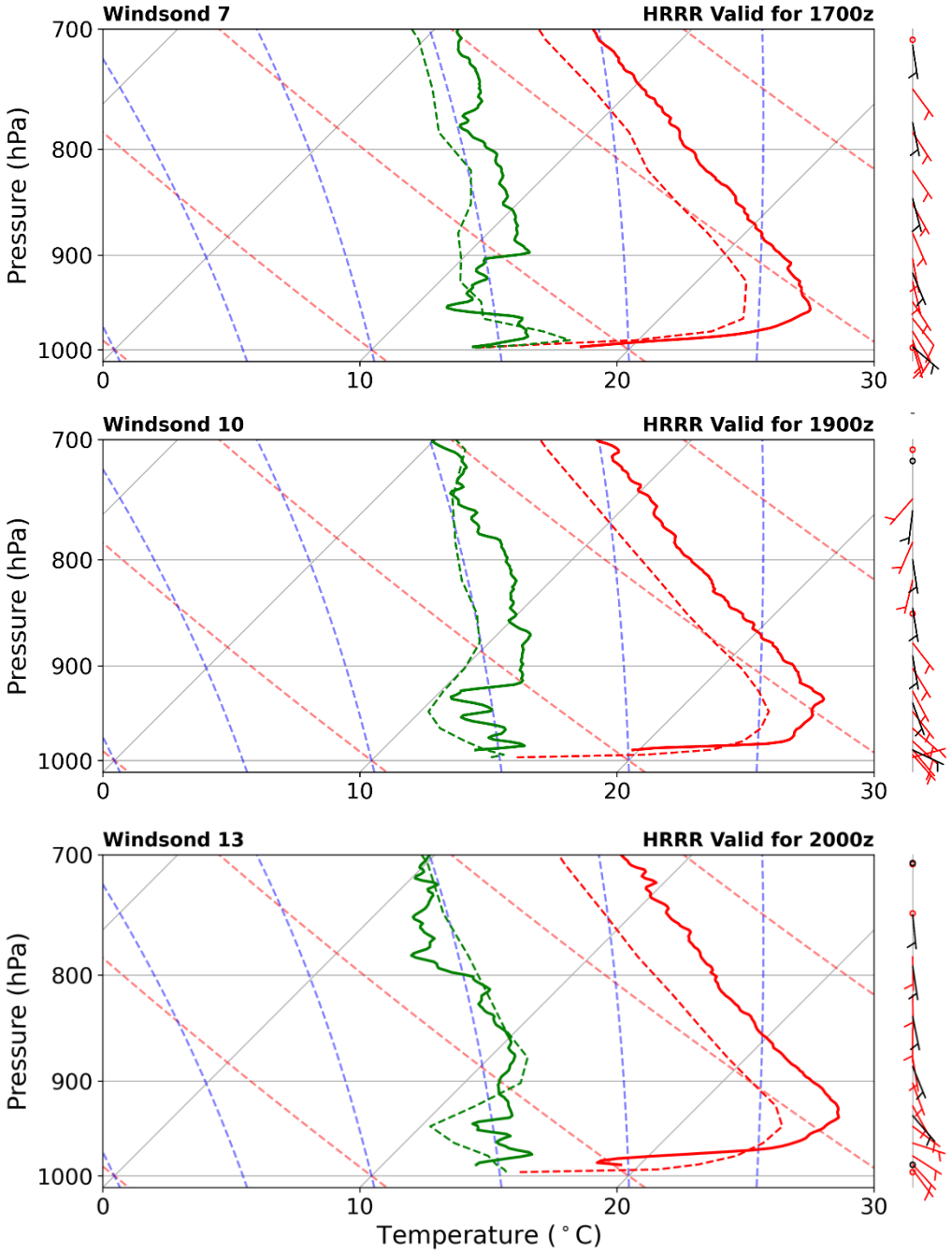

FIG 18. Vertical profile comparisons of Windsonds 7 (top), 10 (middle), and 13 (bottom) versus HRRR 0 h Analyses on June 1st, 2023. Temperature is plotted in red, and dewpoint is plotted in green. Windsond (HRRR) Wind barbs are plotted in black (red).

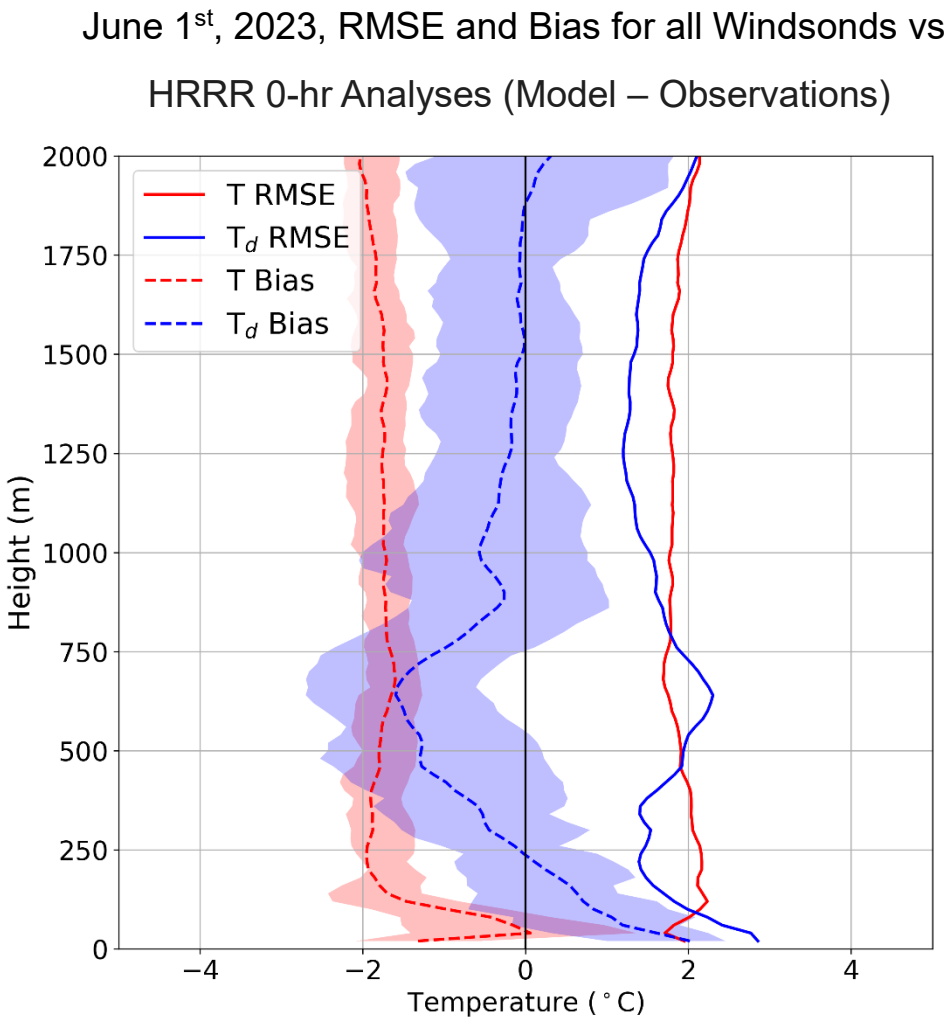

FIG 19. Vertical distribution of RMSE (solid) and bias (dashed) for temperature (red) and dewpoint (blue) on June 1st, 2023. Shaded values compromise the bias between the 25th and 75th percentiles.

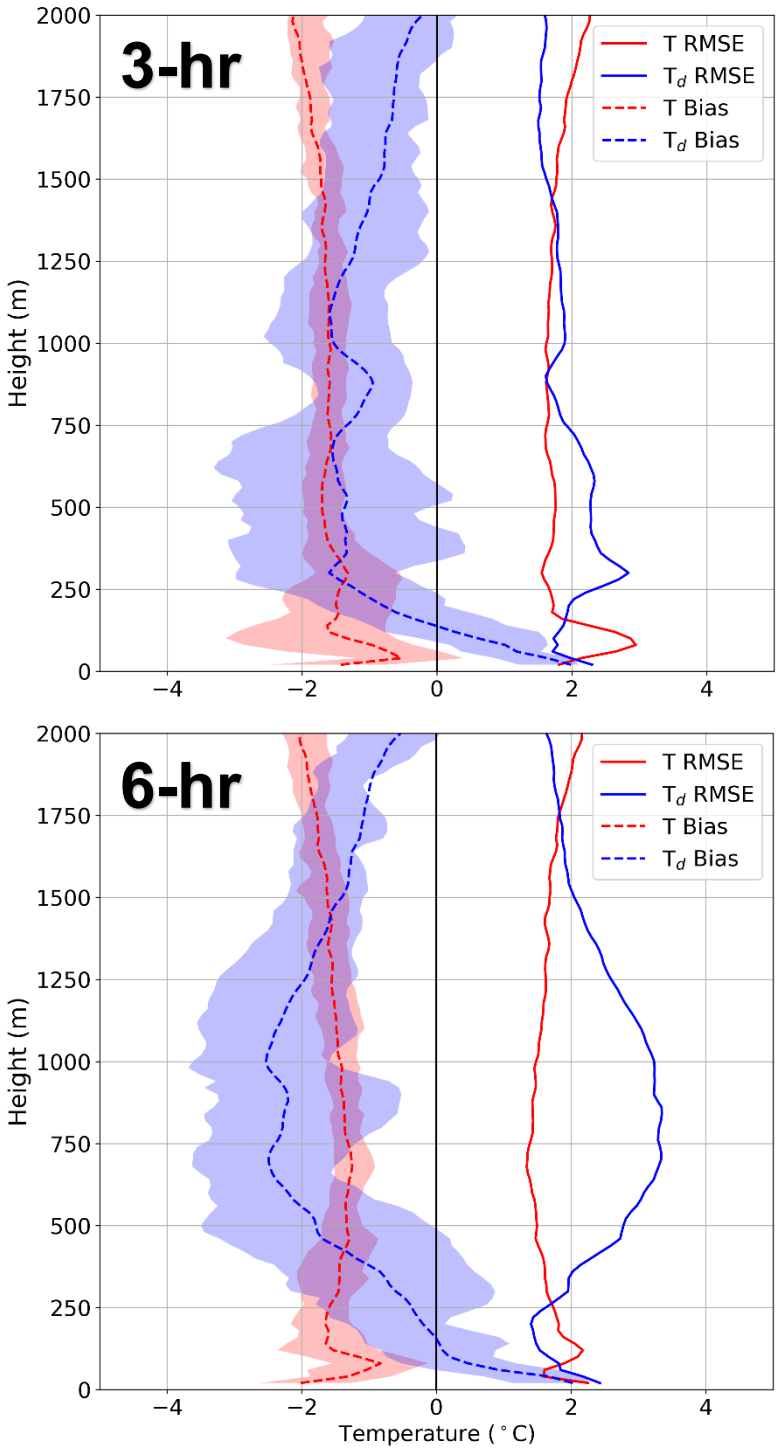

FIG 20. Vertical Distribution of RMSE and Bias for the HRRR 3 h (top) and 6 h (bottom) forecasts on June 1st, 2023. RMSE (solid) and bias (dashed) are plotted for temperature (red) and dewpoint (blue) with the 25th and 75th percentile ranges shaded.

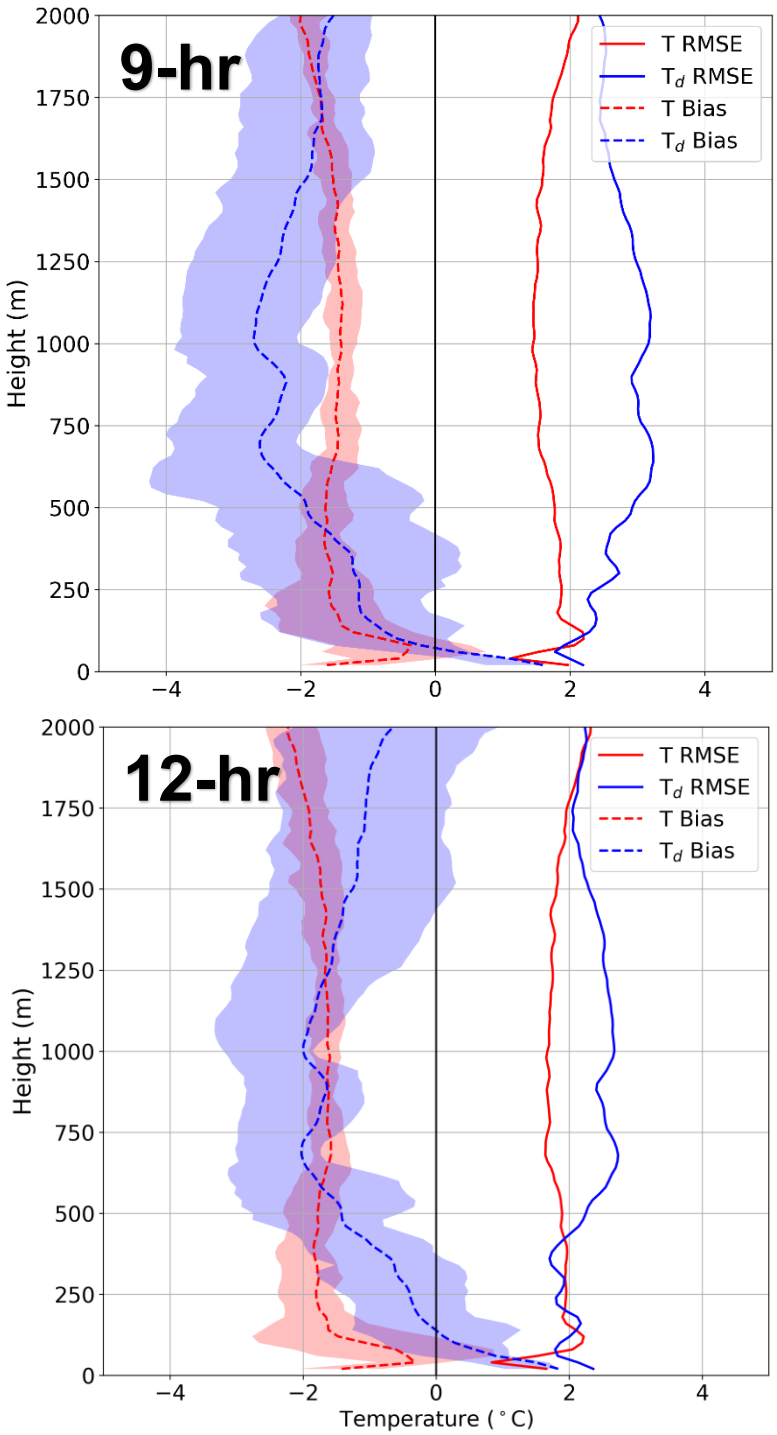

FIG 21. Vertical Distribution of RMSE and Bias for the HRRR 9 h (top) and 12 h (bottom) forecasts on June 1st, 2023. RMSE (solid) and bias (dashed) are plotted for temperature (red) and dewpoint (blue) with the 25th and 75th percentile ranges shaded.

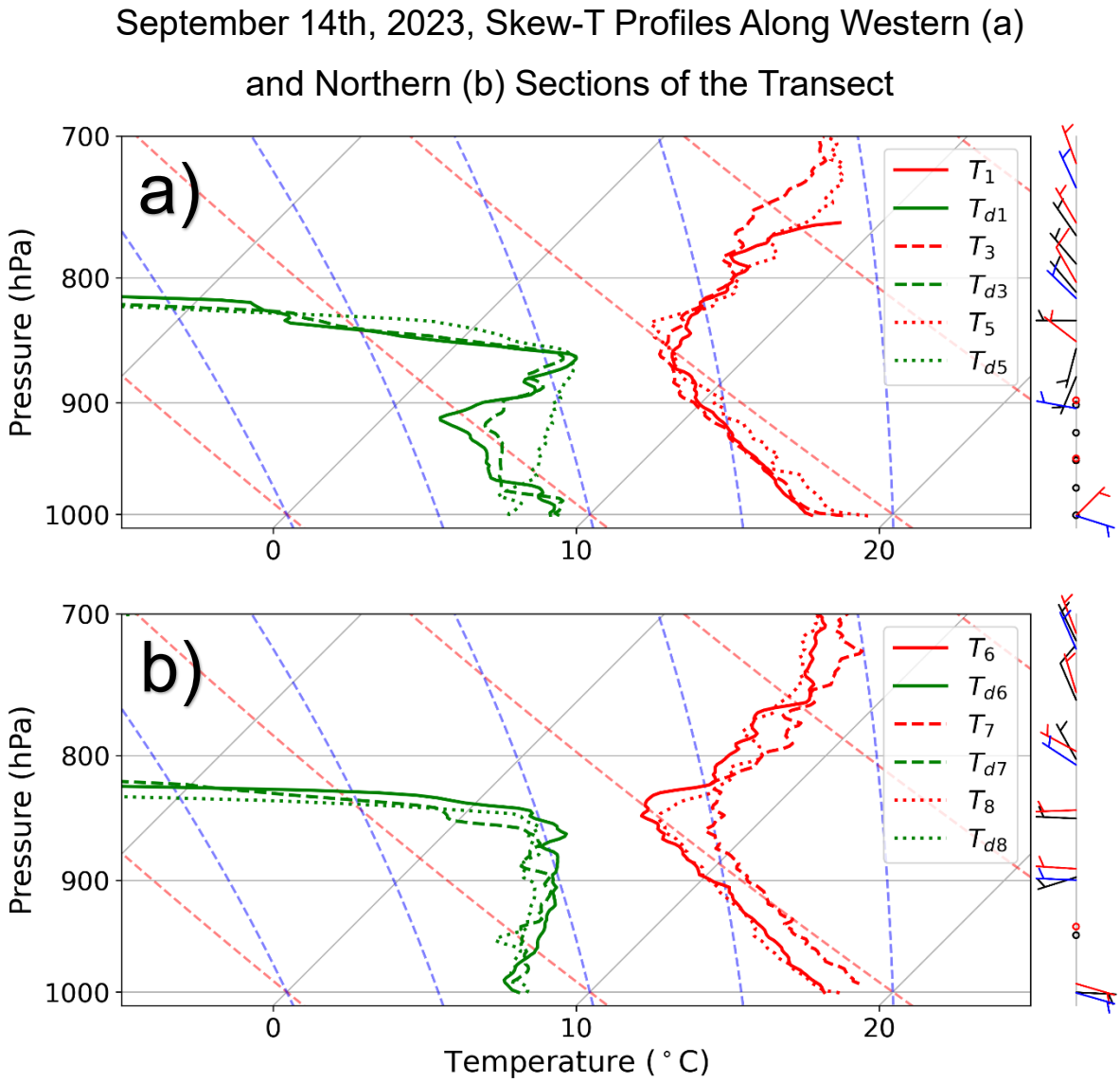

FIG 22. Vertical Skew-T profile comparisons of temperature (red) and dewpoint (green) for Windsonds 1, 3, 5 (a) and 6, 7, 8 (b) for September 14th, 2023. Windsond numbers are denoted by the subscripts in the legend. Wind barbs are plotted chronologically according to the Windsond number through a color range of black, red, to blue.

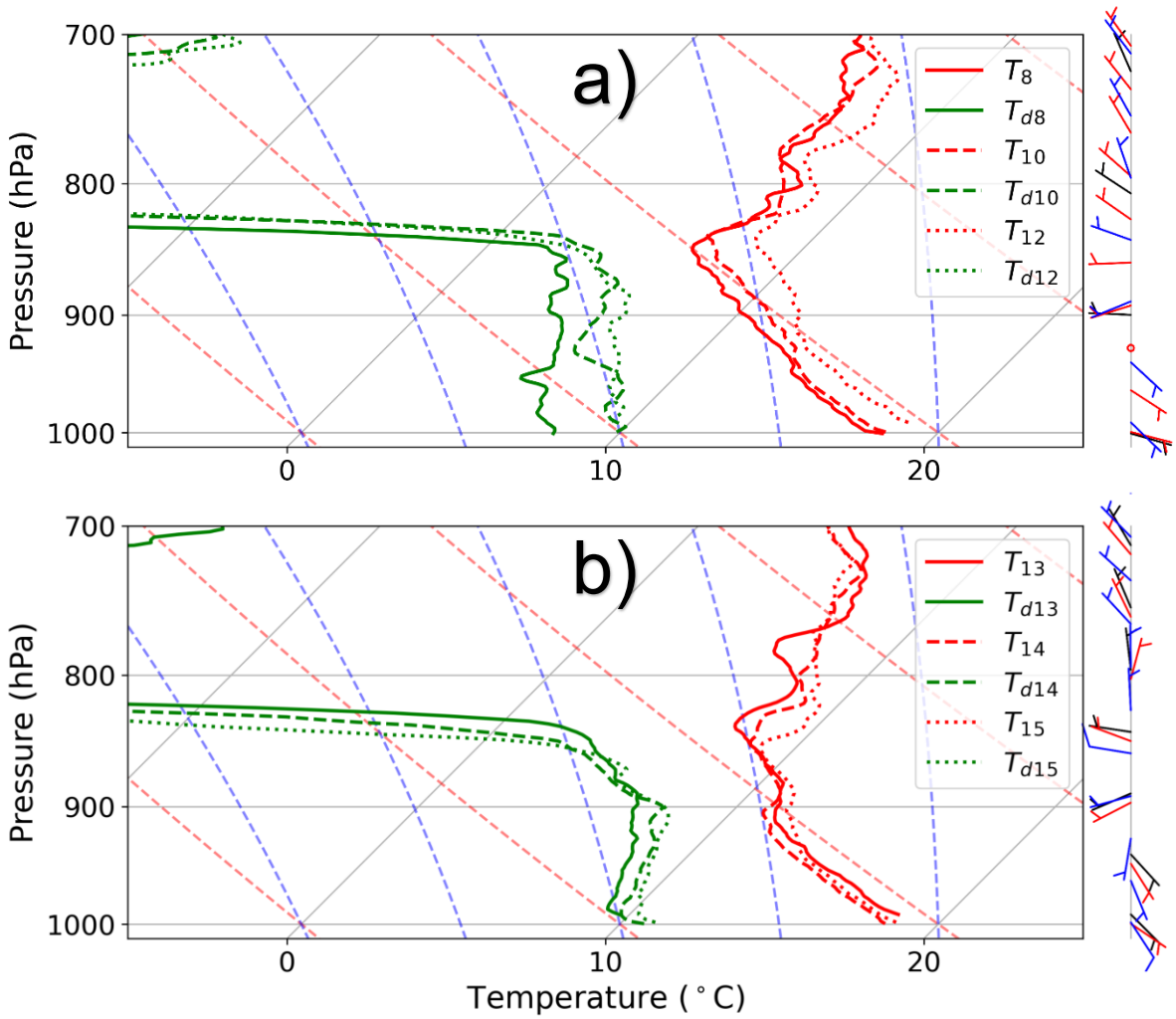

FIG 23. Vertical Skew-T profile comparisons of temperature (red) and dewpoint (green) for Windsonds 8, 10, 12 (a) and 13, 14, 15 (b) for September 14th, 2023. Windsond numbers are denoted by the subscripts in the legend. Wind barbs are plotted chronologically according to the Windsond number through a color range of black, red, to blue.

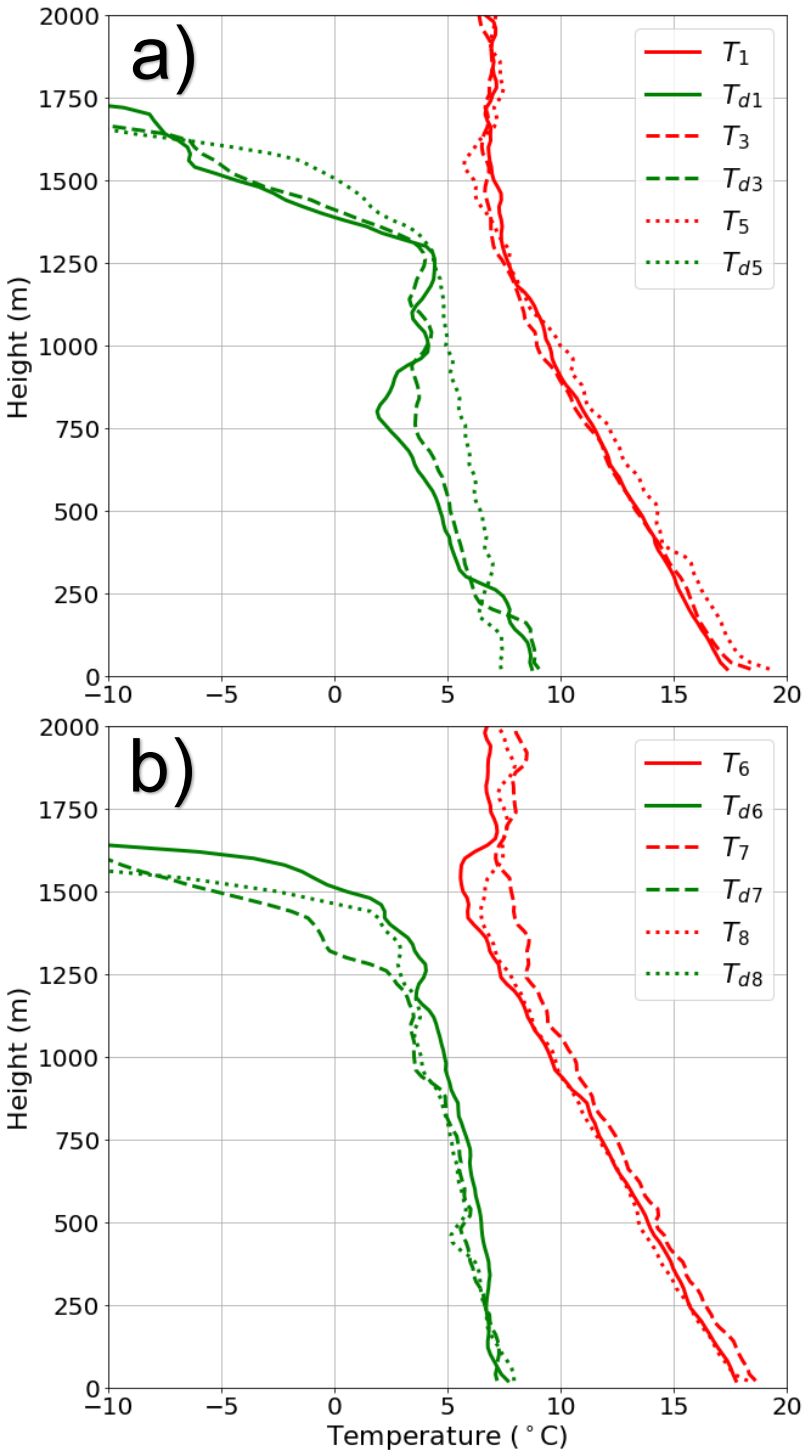

FIG 24. Vertical profile comparisons, using a height-based coordinate system for temperature (red) and dewpoint (green) for Windsonds 1, 3, 5 (a) and 6, 7, 8 (b) for the September 14th, 2023, mission. Windsond numbers are denoted by the subscripts in the legend.

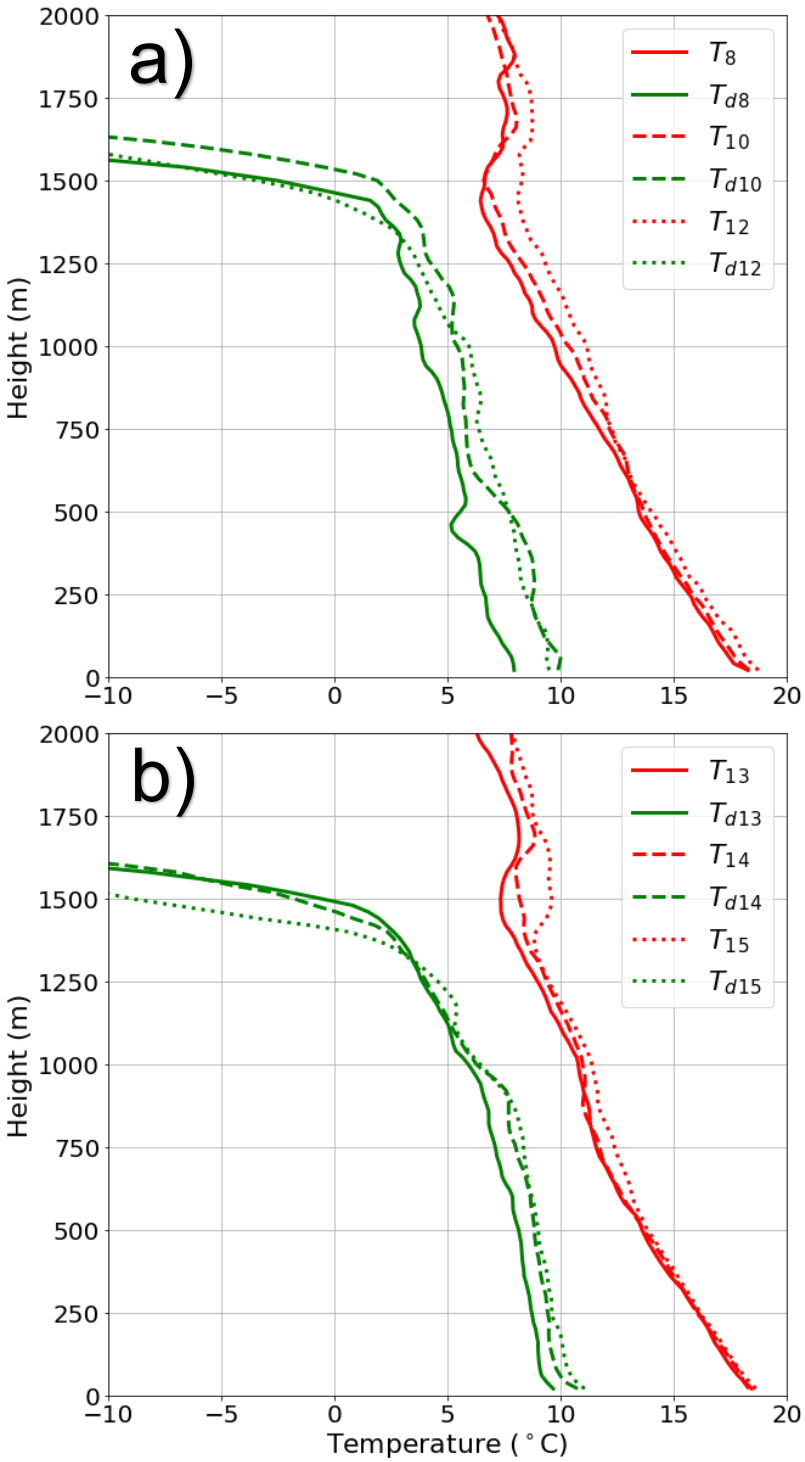

FIG 25. Vertical profile comparisons, using a height-based coordinate system for temperature (red) and dewpoint (green) for Windsonds 8, 10, 12 (a) and 13, 14, 15 (b) for the September 14th, 2023, mission. Windsond numbers are denoted by the subscripts in the legend.

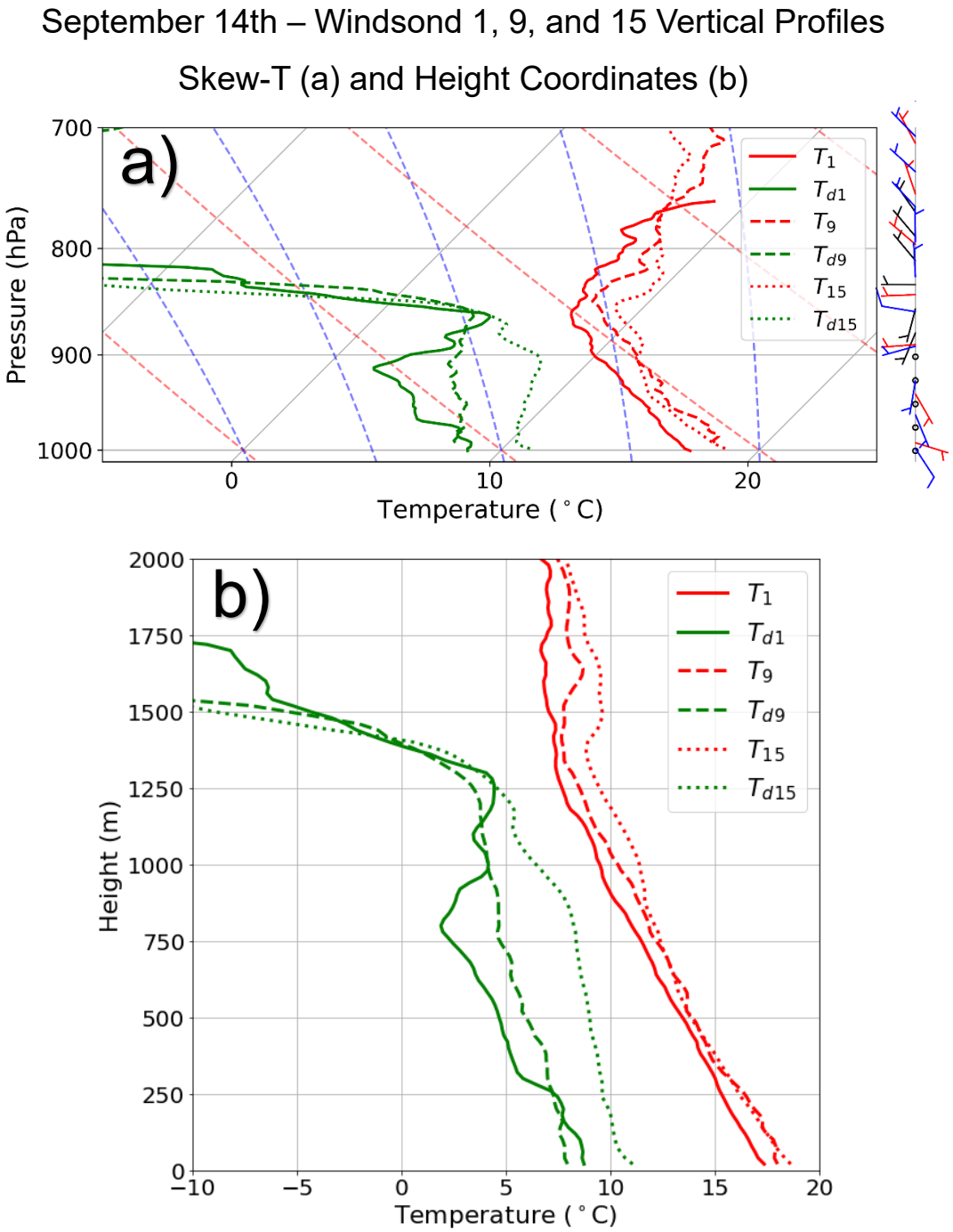

FIG 26. Vertical profile comparisons of Windsonds 1 (solid), 9 (dashed), and 15 (dotted) using a skew-T diagram (a) and a height-based coordinate system diagram (b). Temperature is plotted in red, and dewpoint is plotted in green. Wind barbs are plotted chronologically according to Windsond number through a color range of black, red, and blue.

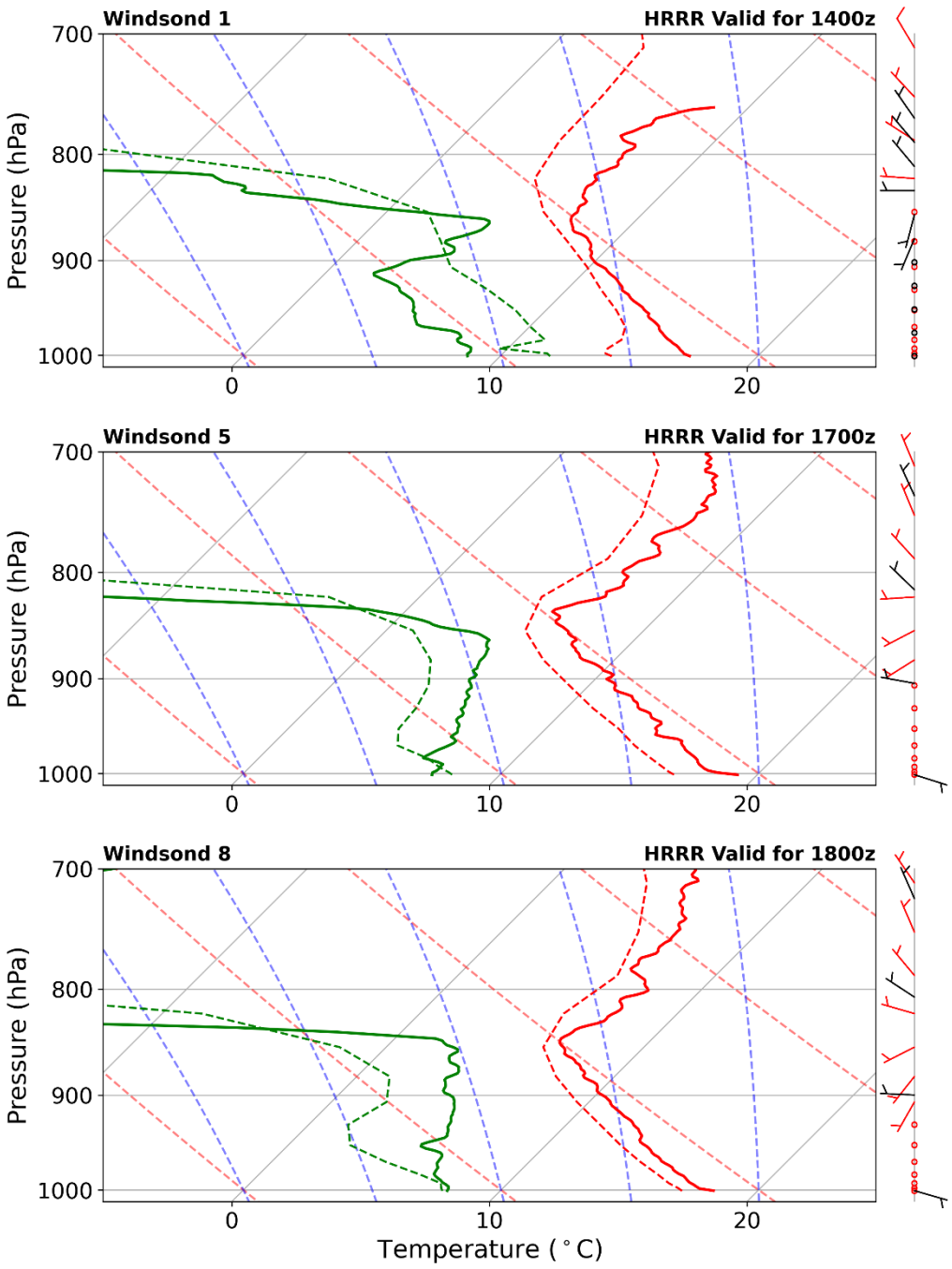

FIG 27. Vertical profile comparisons of Windsonds 1 (top), 5 (middle), and 8 (bottom) versus HRRR 0 h Analyses on September 14th, 2023. Temperature is plotted in red, and dewpoint is plotted in green. Windsond (HRRR) Wind barbs are plotted in black (red).

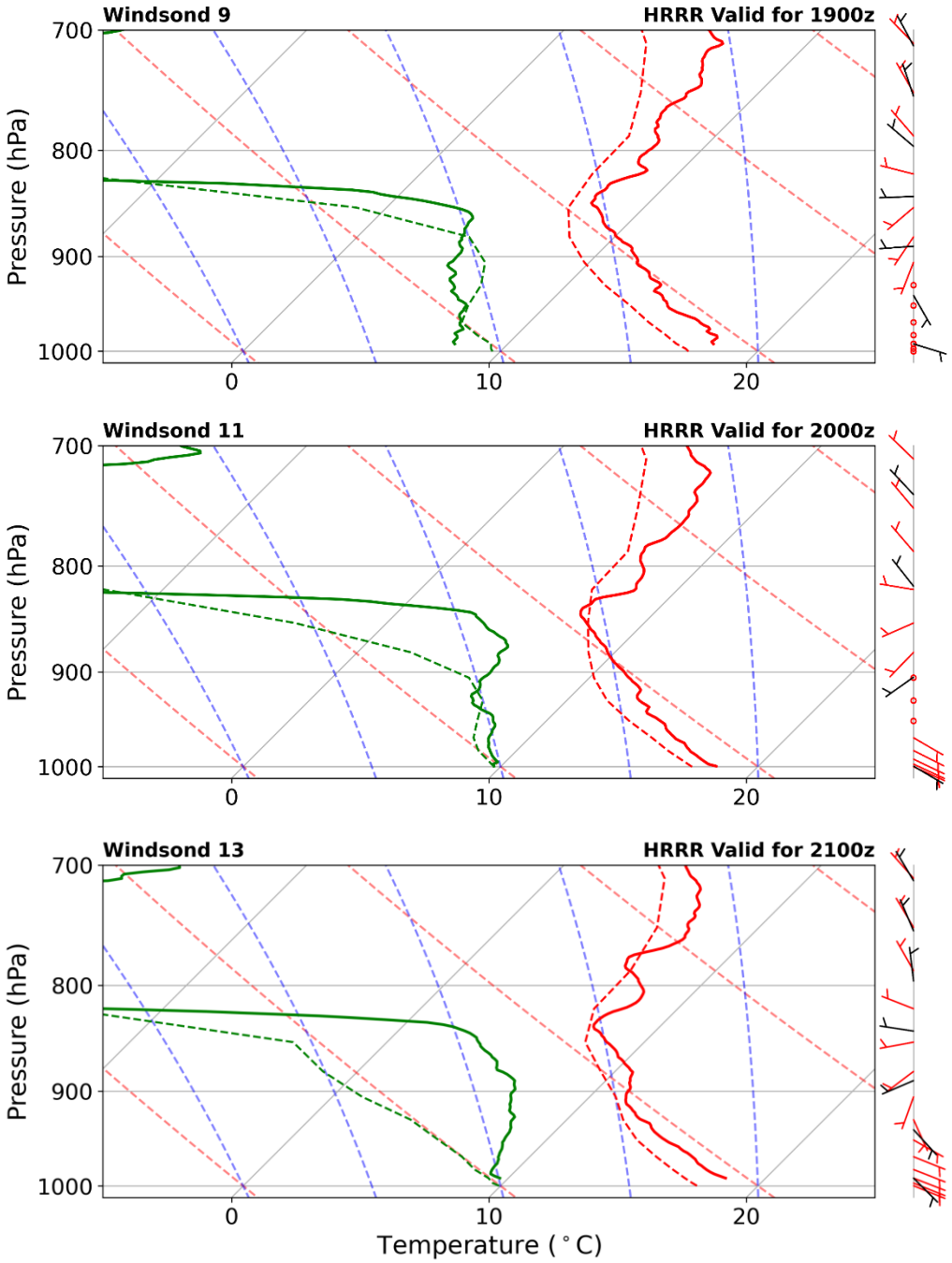

FIG 28. Vertical profile comparisons of Windsonds 9 (top), 11 (middle), and 13 (bottom) versus HRRR 0 h Analyses on September 14th, 2023. Temperature is plotted in red, and dewpoint is plotted in green. Windsond (HRRR) Wind barbs are plotted in black (red).

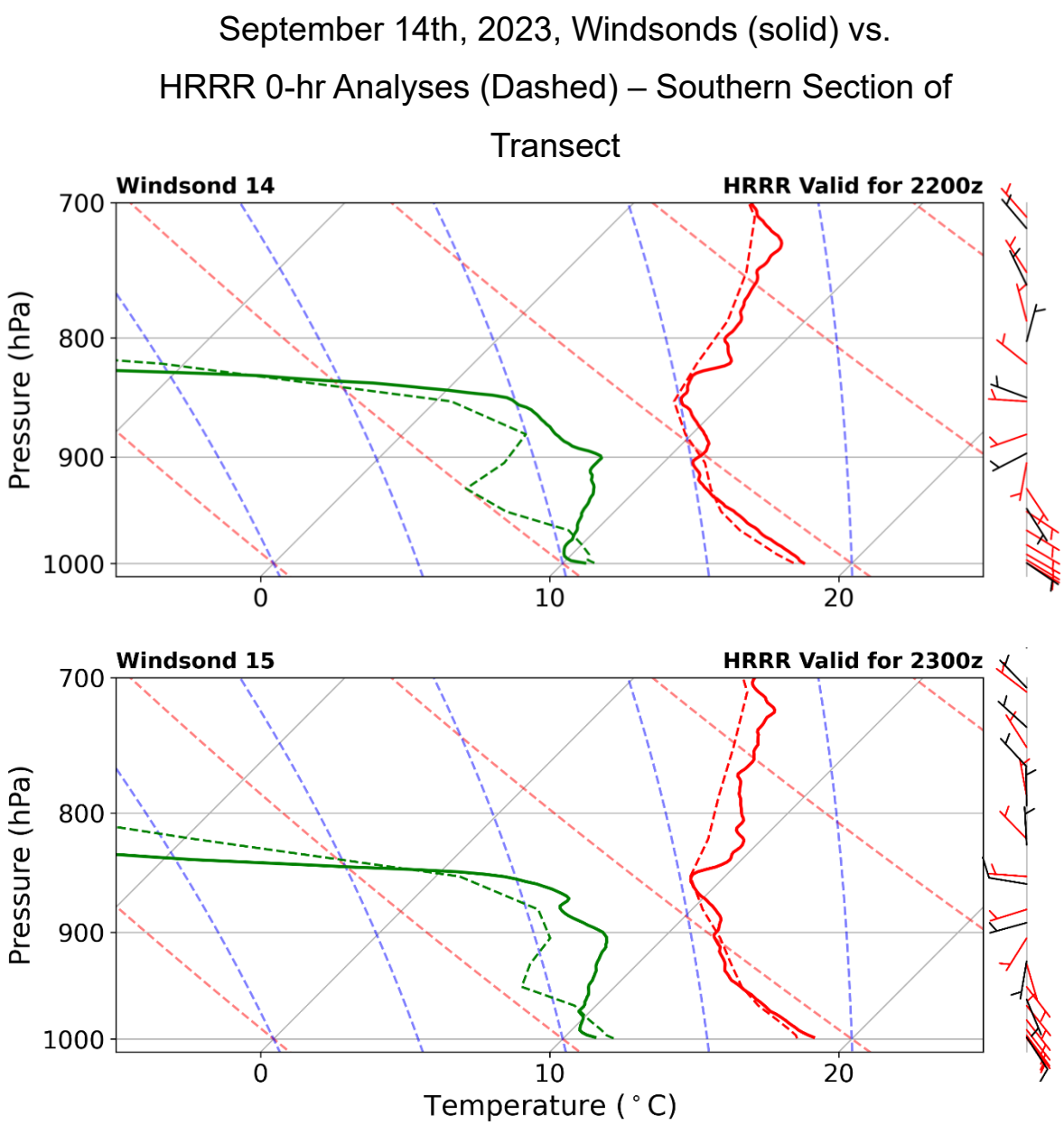

FIG 29. Vertical profile comparisons of Windsonds 14 (top) and 15 (bottom) versus HRRR 0 h Analyses on September 14th, 2023. Temperature is plotted in red, and dewpoint is plotted in green. Windsond (HRRR) Wind barbs are plotted in black (red).

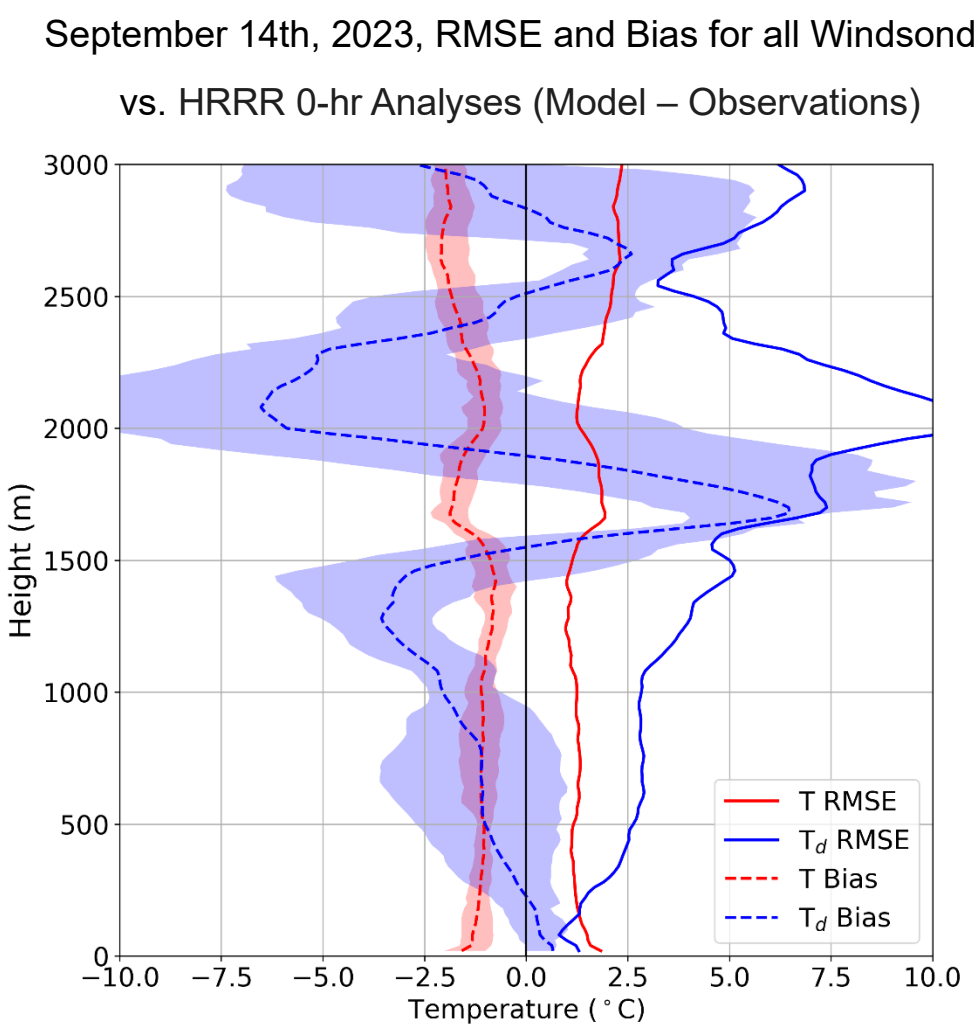

FIG 30. Vertical distribution of RMSE (solid) and bias (dashed) for temperature (red) and dewpoint (blue) on September 14th, 2023. Shaded values compromise the bias between the 25th and 75th percentiles.

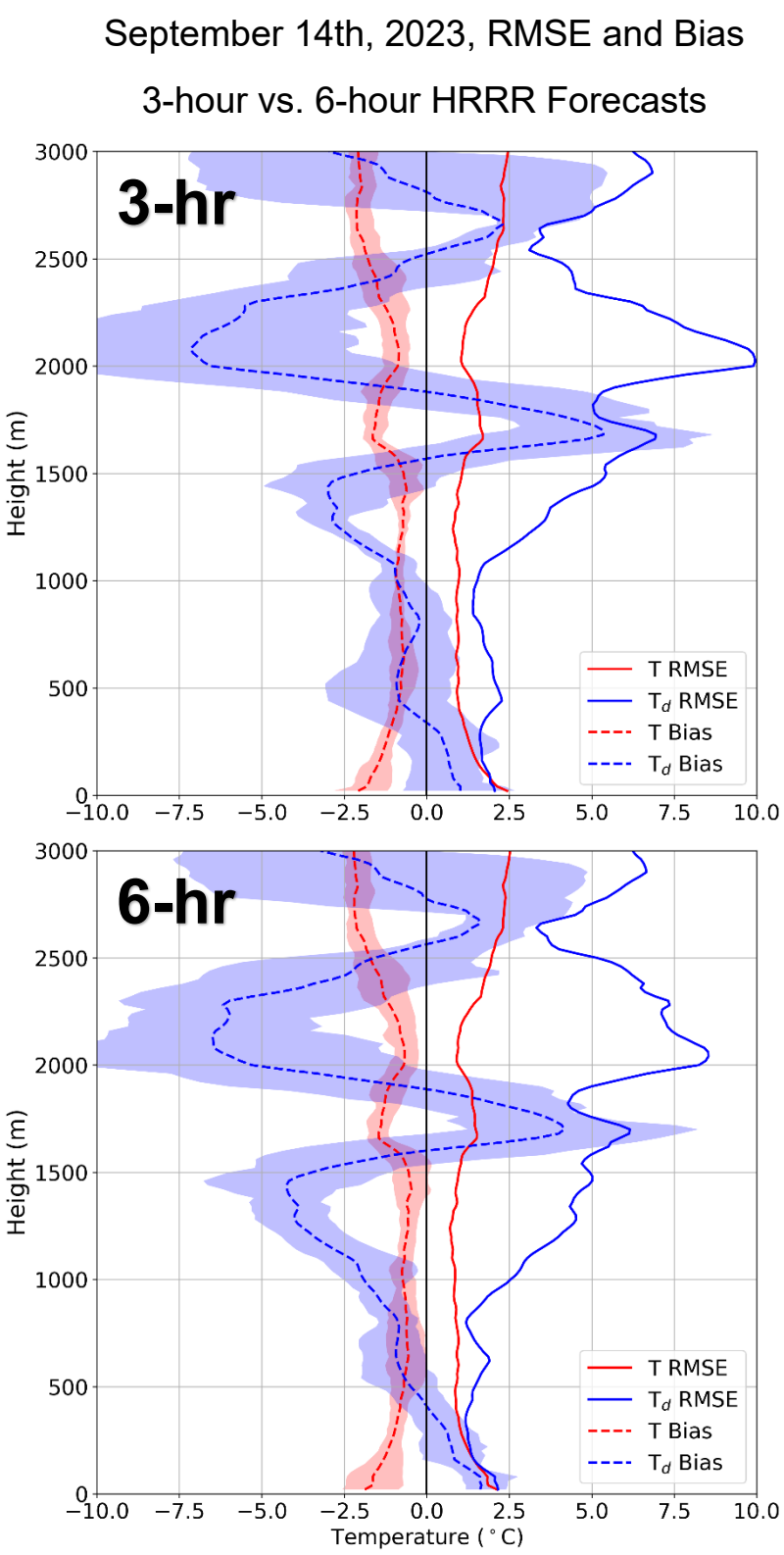

FIG 31. Vertical Distribution of RMSE and Bias for the HRRR 3 h (top) and 6 h (bottom) forecasts on September 14th, 2023. RMSE (solid) and bias (dashed) are plotted for temperature (red) and dewpoint (blue) with the 25th and 75th percentile ranges shaded.

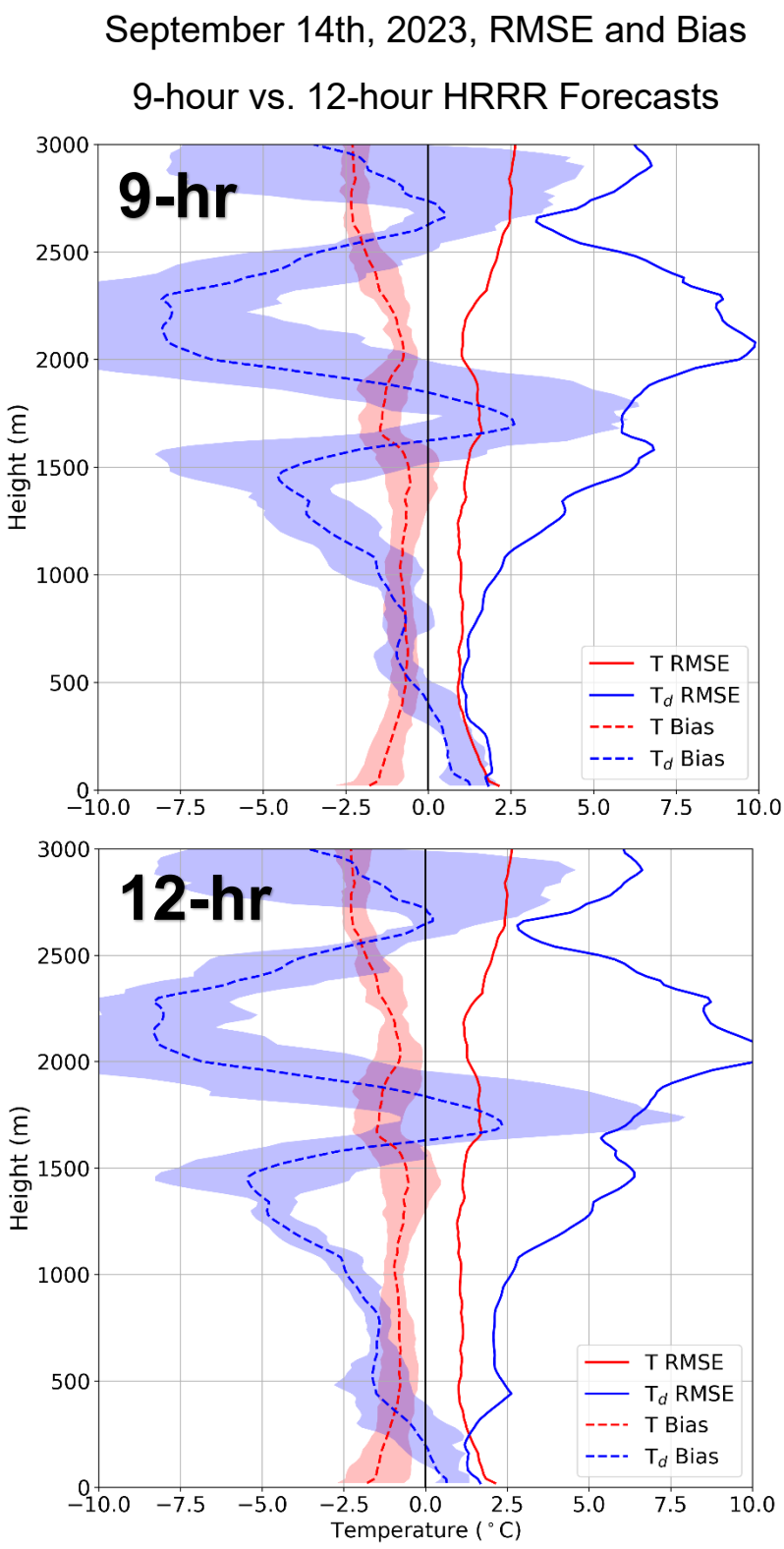

FIG 32. Vertical Distribution of RMSE and Bias for the HRRR 9 h (top) and 12 h (bottom) forecasts on September 14th, 2023. RMSE (solid) and bias (dashed) are plotted for temperature (red) and dewpoint (blue) with the 25th and 75th percentile ranges shaded.

APPENDIX B:

Lake-breeze Algorithm Output

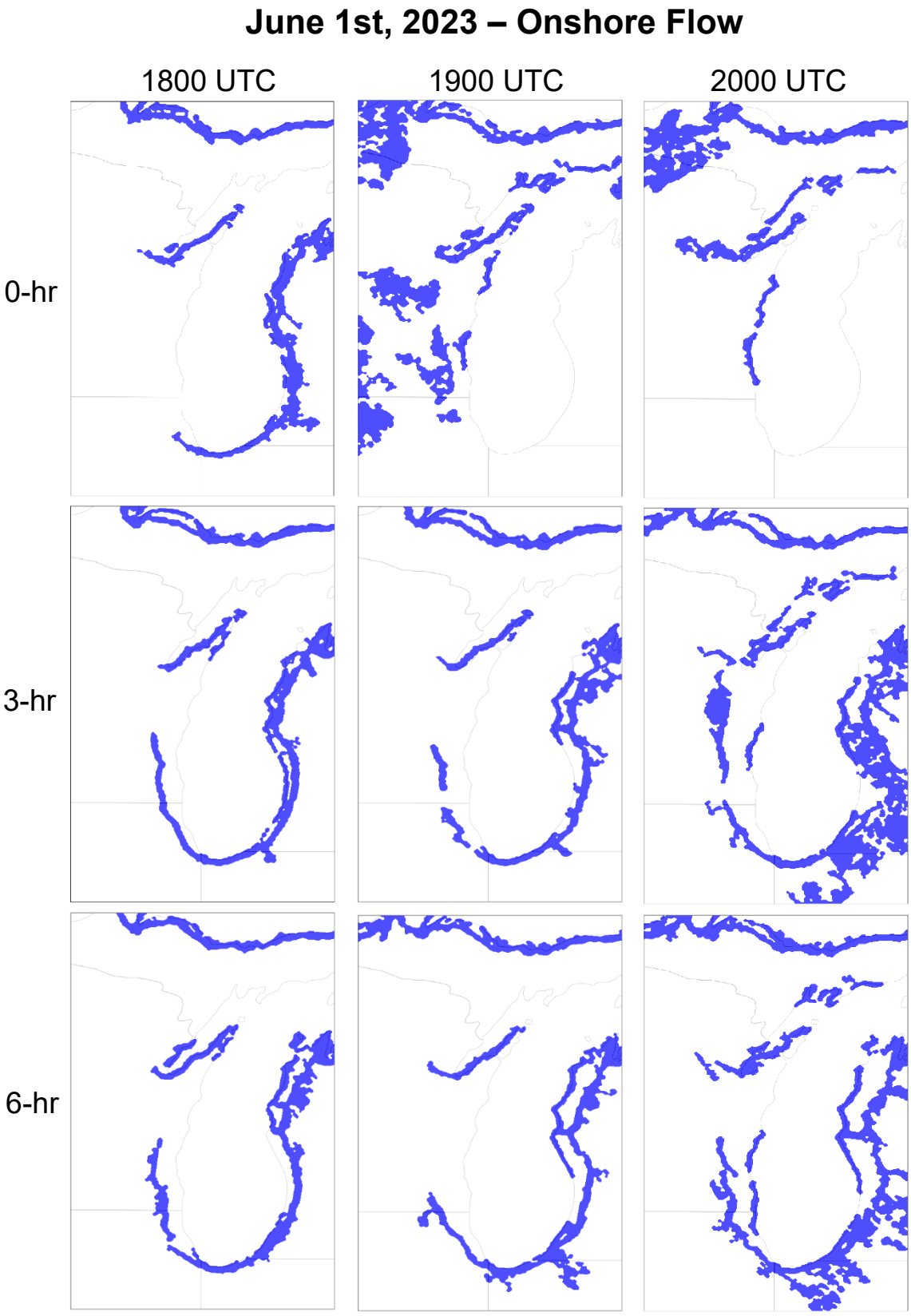

FIG 33. Lake-breeze algorithm output for June 1st, 2023 for 1800 (left), 1900 (middle), and 2000 (right) UTC using the HRRR 0 (top), 3 (middle), and 6 (bottom) hour forecasts.

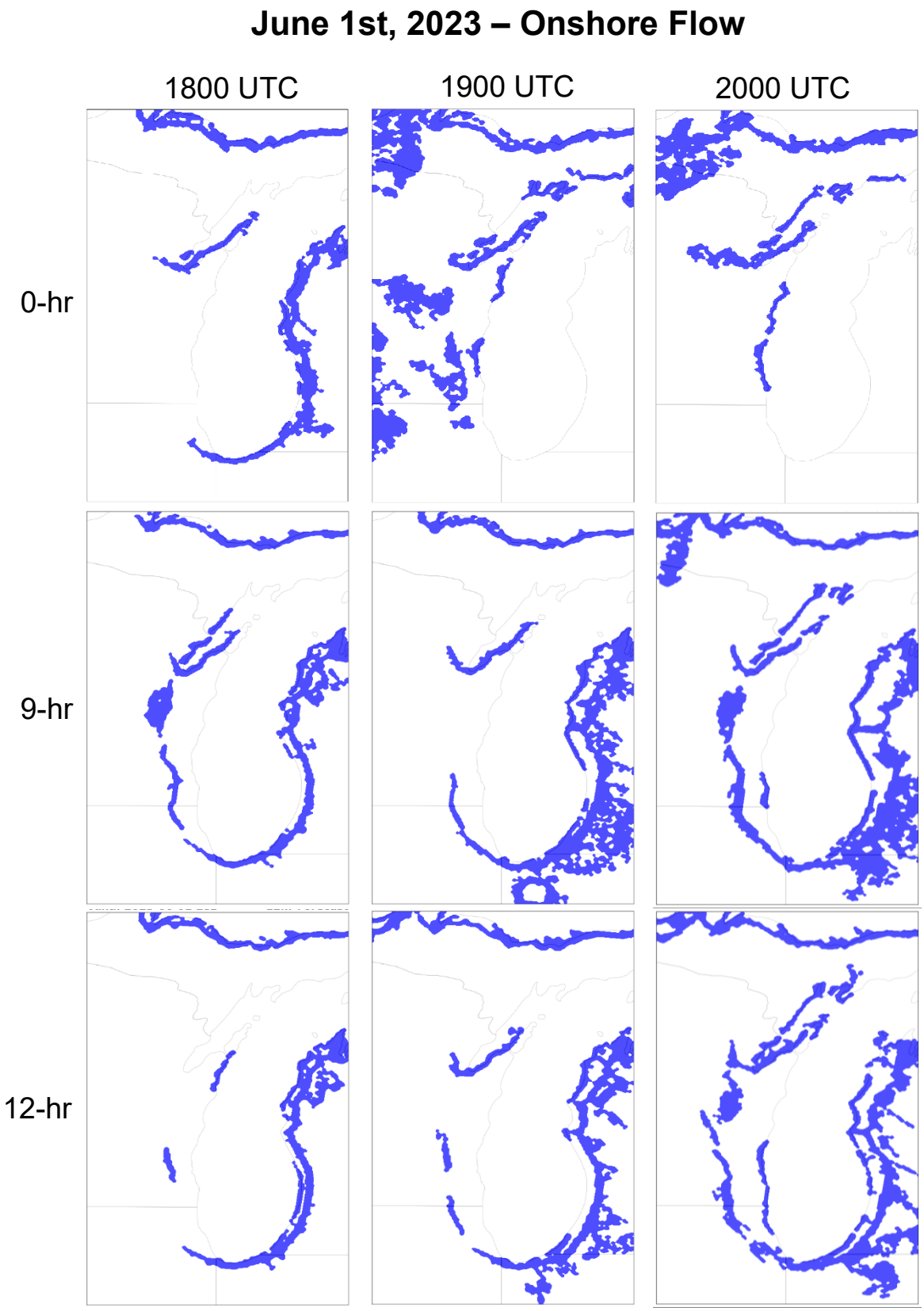

FIG 34. Lake-breeze algorithm output for June 1st, 2023 for 1800 (left), 1900 (middle), and 2000 (right) UTC using the HRRR 0 (top), 9 (middle), and 12 (bottom) hour forecasts.

September 14th, 2023 – 0 Hour HRRR Analyses

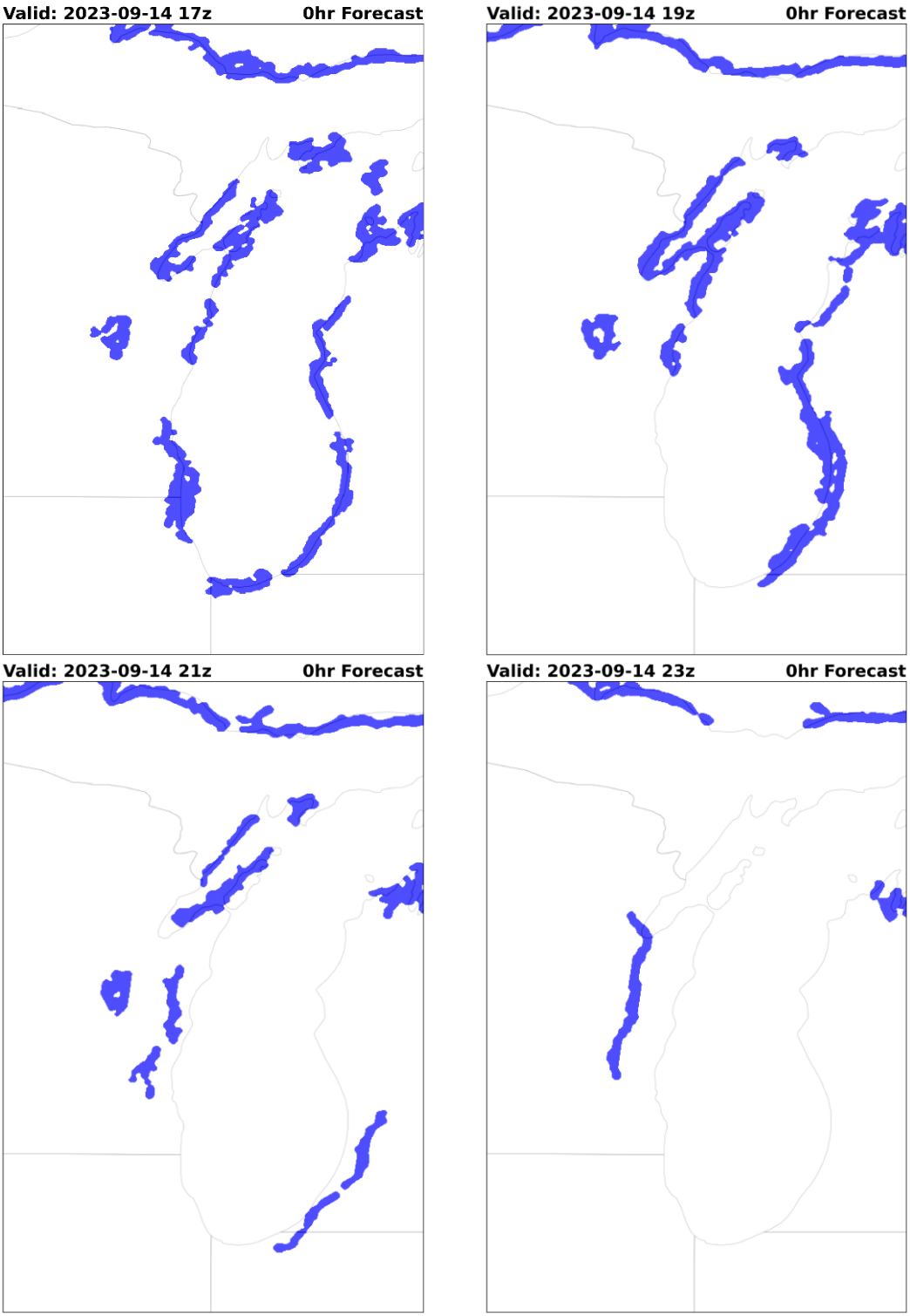

FIG 35. Plot of the lake-breeze algorithm output using HRRR 0 h analyses valid for 1700 (top left), 1900 (top right), 2100 (bottom left), and 2300 (bottom right) on September 14th, 2023.

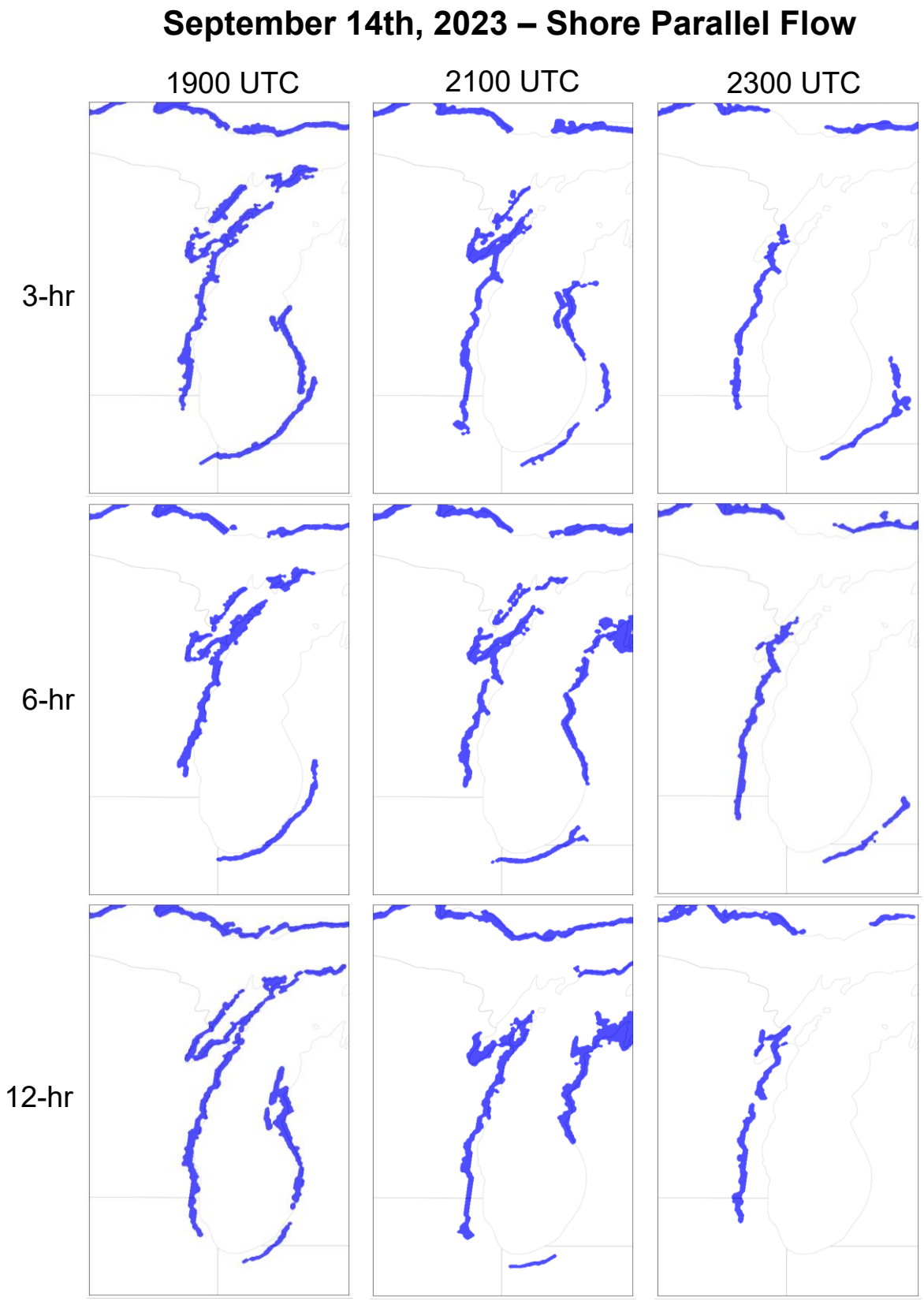

FIG 36. Lake-breeze algorithm output for September 14th, 2023 for 1900 (left), 2100 (middle), and 2300 (right) UTC using the HRRR 3 (top), 6 (middle), and 12 (bottom) hour forecasts.

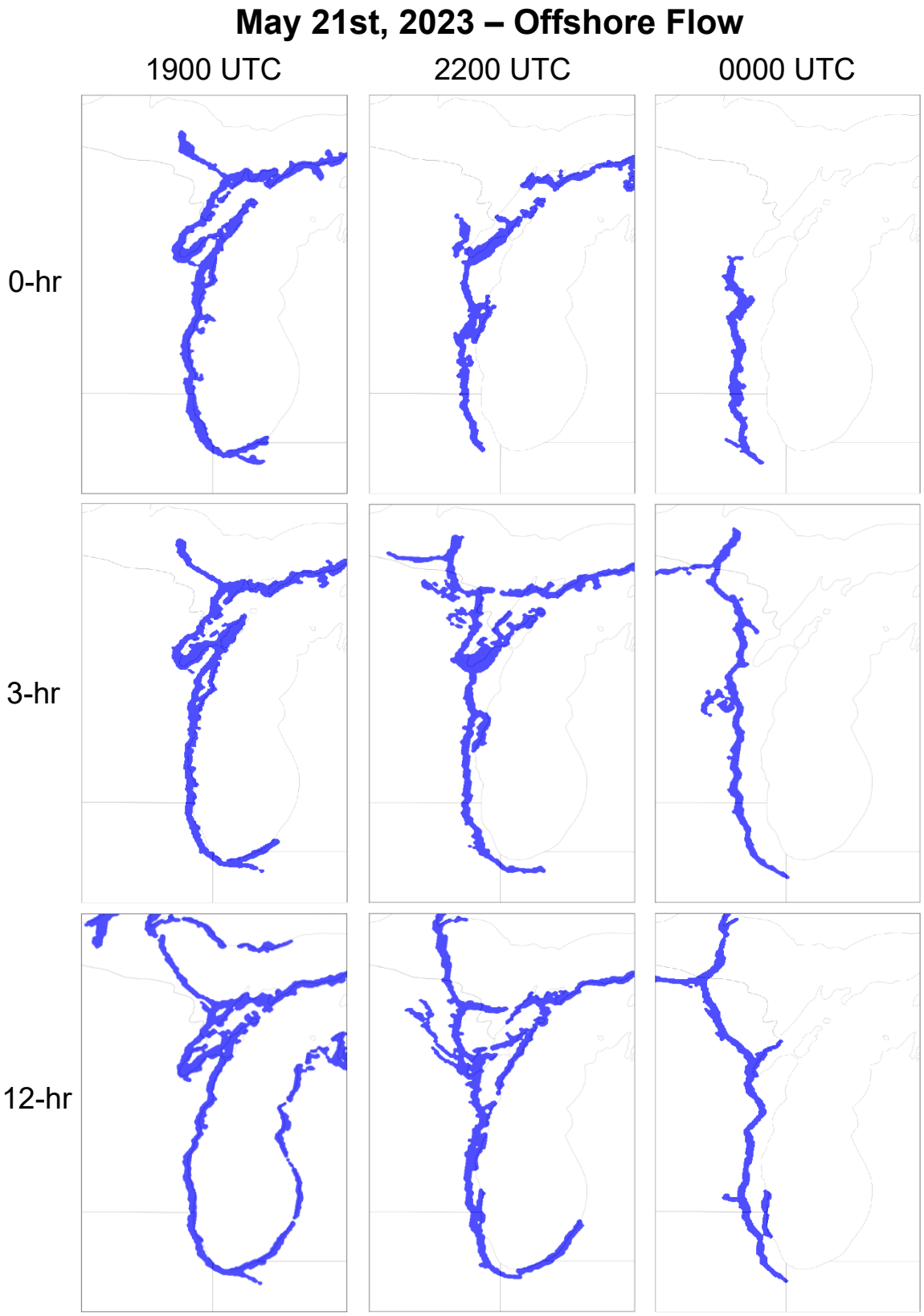

FIG 37. Lake-breeze algorithm output for May 21st, 2023 for 1900 (left), 2200 (middle), and 0000 (right) UTC using the HRRR 0 (top), 3 (middle), and 12 (bottom) hour forecasts.

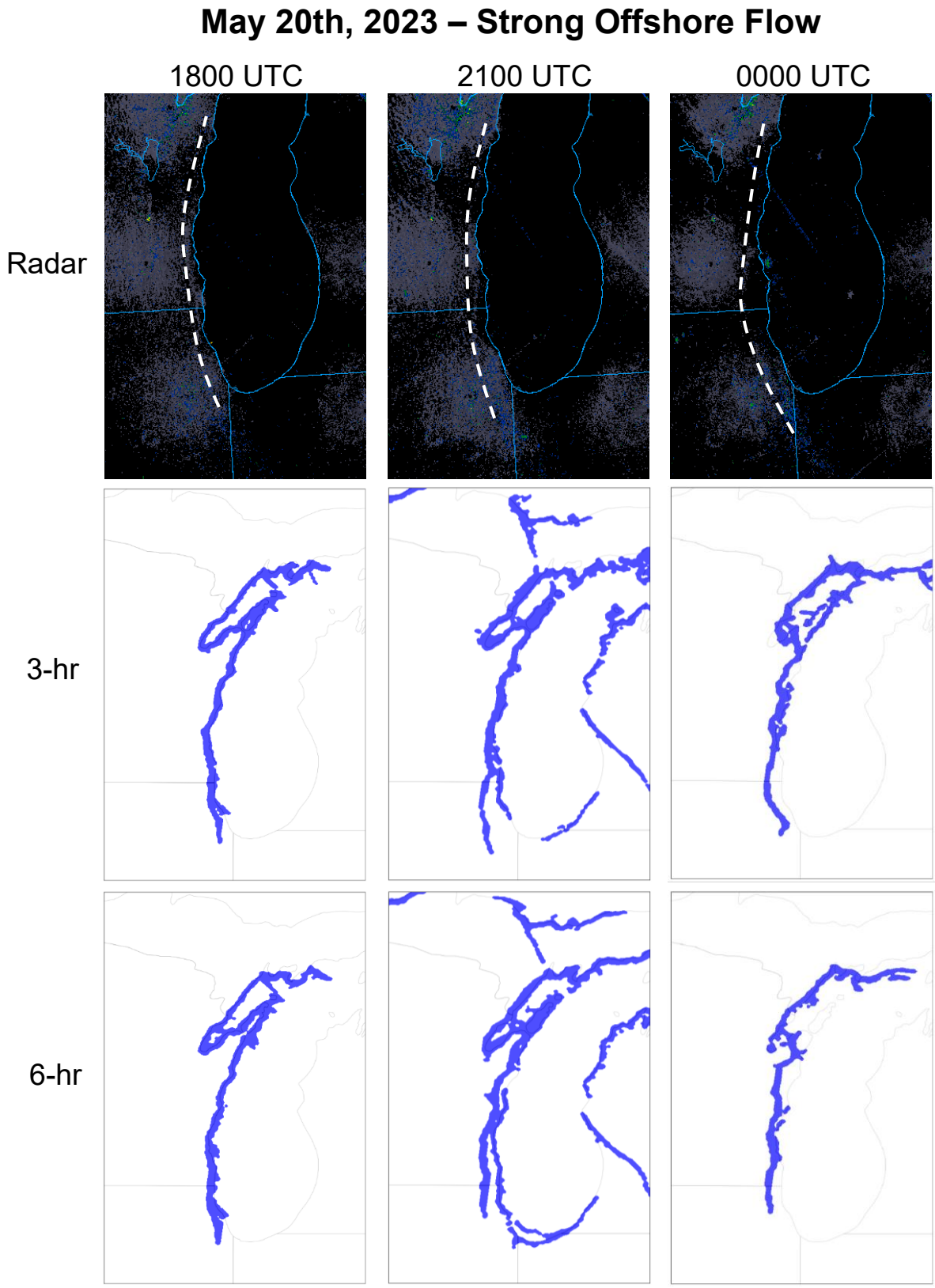

FIG 38. Lake-breeze algorithm output for May 20th, 2023 for 1800 (left), 2100 (middle), and 0000 (right) UTC using the closest radar output (top) and the HRRR 3 (middle) and 6 (bottom) h analyses. White dashed lines denoted the approximate position of the lake-breeze front.

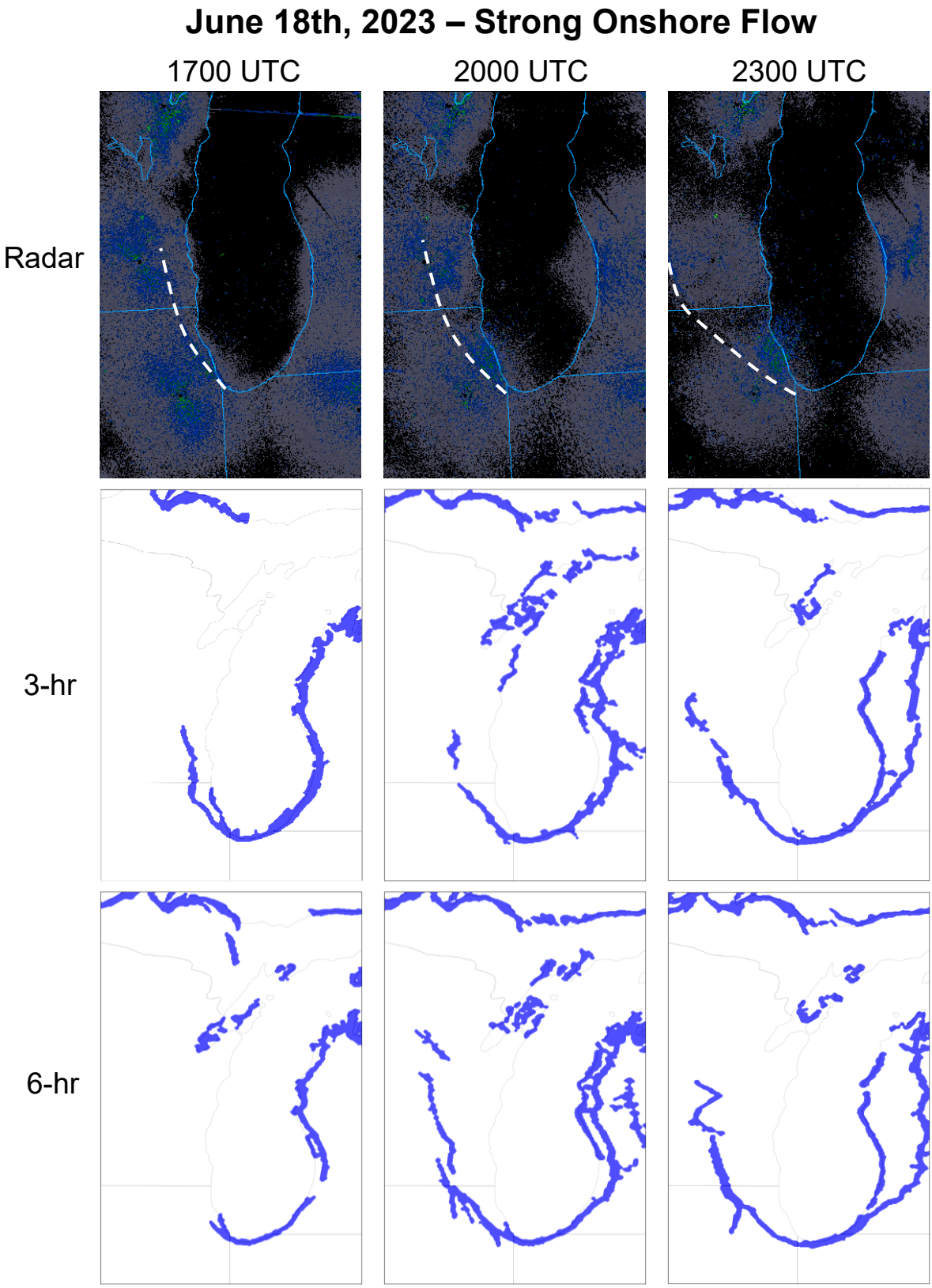

FIG 39. Lake-breeze algorithm output for June 18th, 2023 for 1700 (left), 2000 (middle), and 2300 (right) UTC using the closest radar output (top) and the HRRR 3 (middle) and 6 (bottom) h analyses. White dashed lines denoted the approximate position of the lake-breeze front.

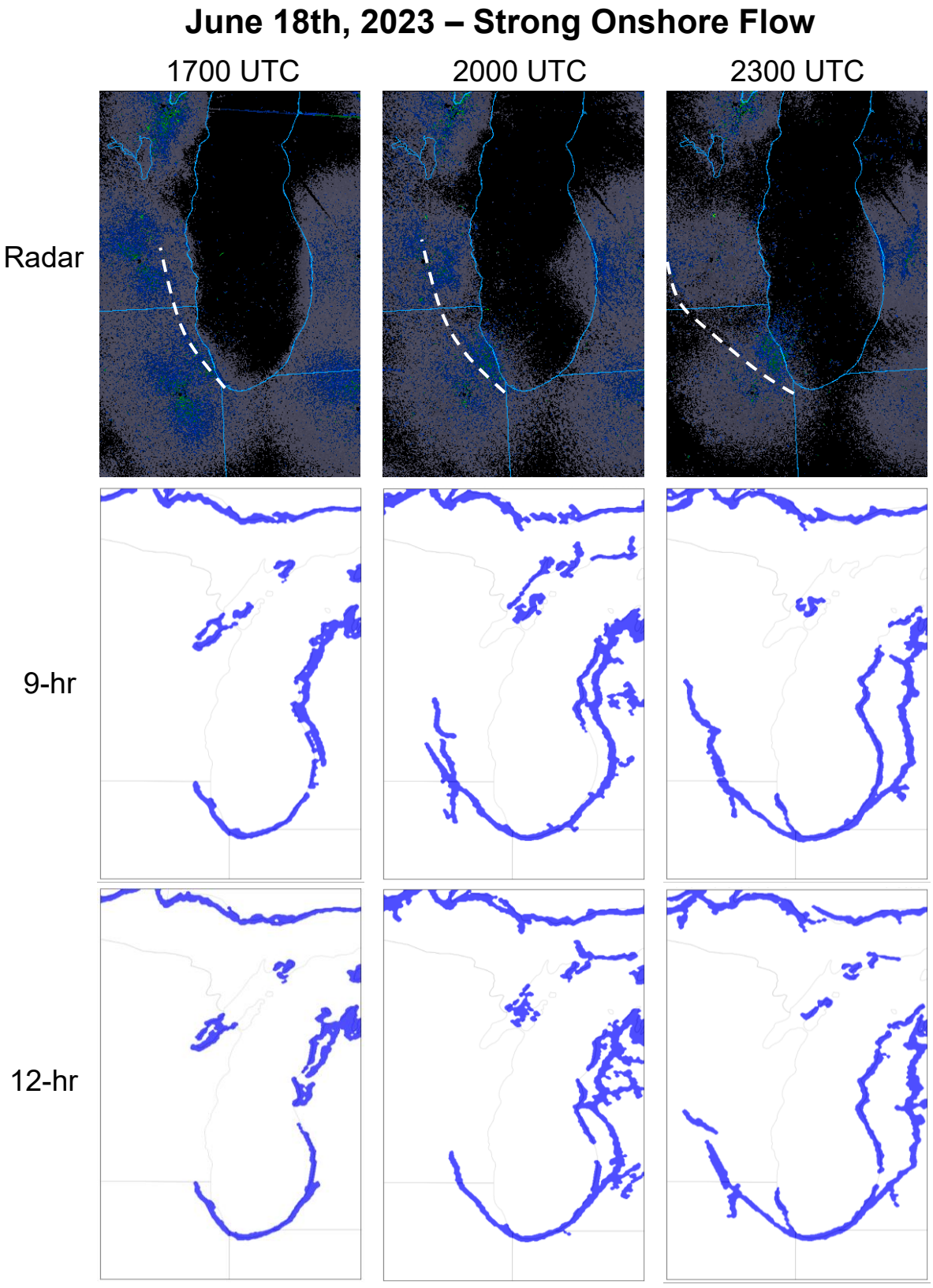

FIG 40. Lake-breeze algorithm output for June 18th, 2023 for 1700 (left), 2000 (middle), and 2300 (right) UTC using the closest radar output (top) and the HRRR 9 (middle) and 12 (bottom) h analyses. White dashed lines denoted the approximate position of the lake-breeze front.

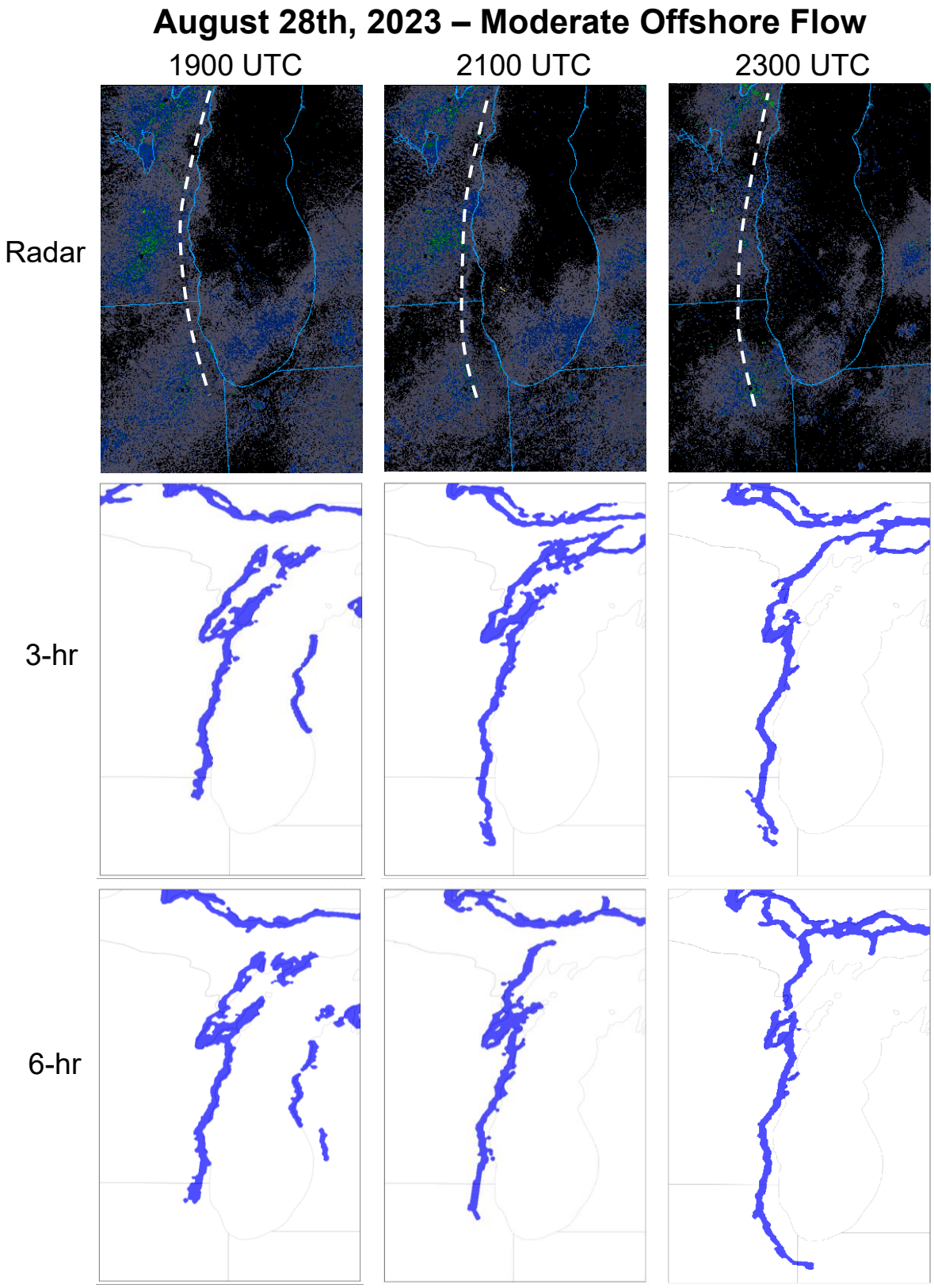

FIG 41. Lake-breeze algorithm output for August 28th, 2023 for 1900 (left), 2100 (middle), and 2300 (right) UTC using the closest radar output (top) and the HRRR 3 (middle) and 6 (bottom) h analyses. White dashed lines denoted the approximate position of the lake-breeze front.

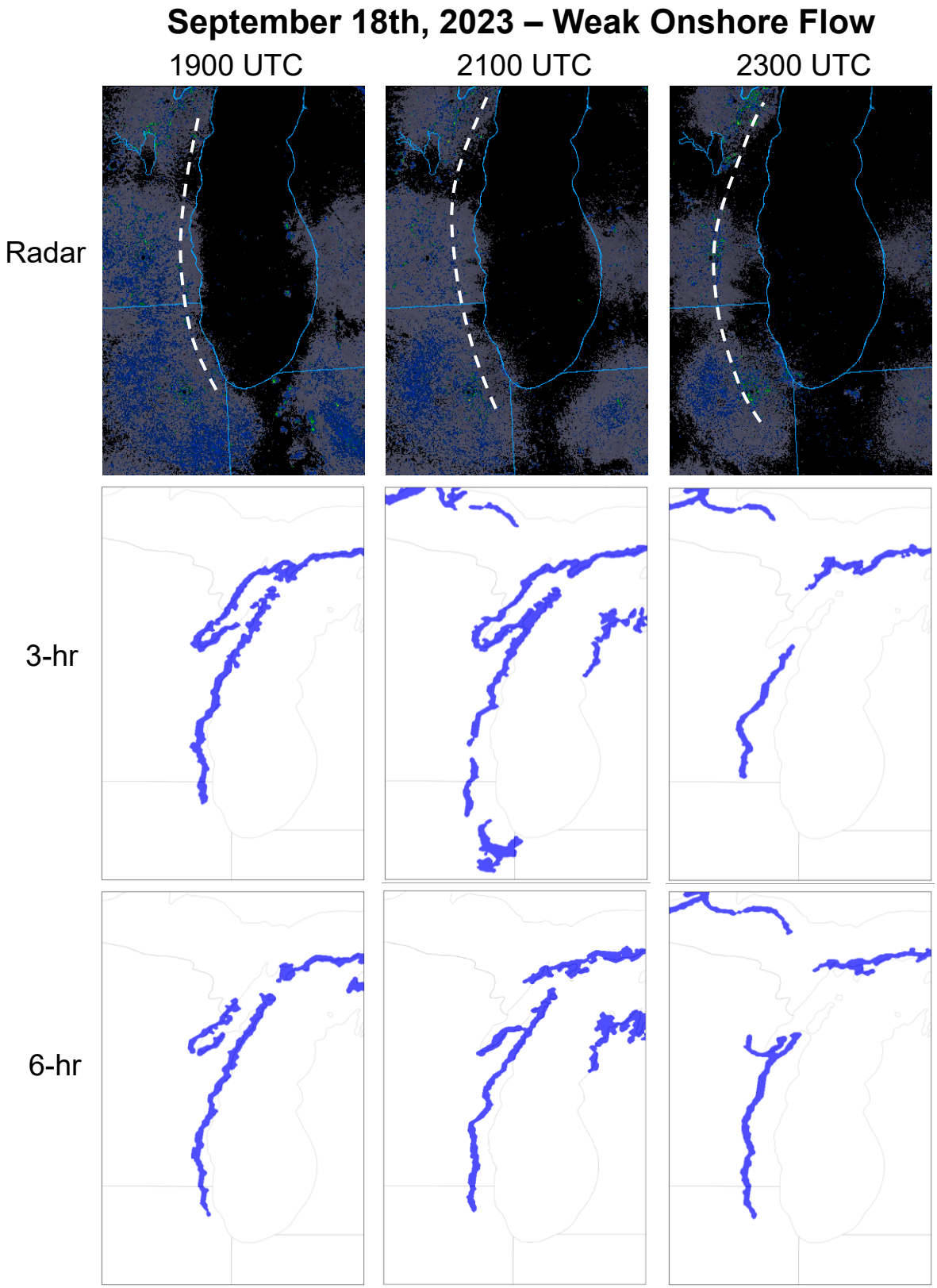

FIG 42. Lake-breeze algorithm output for September 18th, 2023 for 1900 (left), 2100 (middle), and 2300 (right) UTC using the closest radar output (top) and the HRRR 3 (middle) and 6 (bottom) h analyses. White dashed lines denoted the approximate position of the lake-breeze front.